



**BOUNDARY LAYER MEASUREMENTS IN THE TRISONIC GAS-DYNAMICS
FACILITY USING PARTICLE IMAGE VELOCIMETERY WITH CO₂ SEEDING**

THESIS

Daniel B. Wolfe, Major, USAF

AFIT/GAE/ENY/12-M43

**DEPARTMENT OF THE AIR FORCE
AIR UNIVERSITY**

AIR FORCE INSTITUTE OF TECHNOLOGY

Wright-Patterson Air Force Base, Ohio

APPROVED FOR PUBLIC RELEASE; DISTRIBUTION UNLIMITED

The views expressed in this thesis are those of the author and do not reflect the official policy or position of the United States Air Force, Department of Defense, or the United States Government. This material is declared a work of the U.S. Government and is not subject to copyright protection in the United States.

AFIT/GAE/ENY/12-M43

**BOUNDARY LAYER MEASUREMENTS IN THE TRISONIC GAS-DYNAMICS
FACILITY USING PARTICLE IMAGE VELOCIMETERY WITH CO₂ SEEDING**

THESIS

Presented to the Faculty

Department of Aeronautics and Astronautics

Graduate School of Engineering and Management

Air Force Institute of Technology

Air University

Air Education and Training Command

In Partial Fulfillment of the Requirements for the
Degree of Master of Science in Aeronautical Engineering

Daniel B. Wolfe, BS

Major, USAF

March 2012

APPROVED FOR PUBLIC RELEASE; DISTRIBUTION UNLIMITED

**BOUNDARY LAYER MEASUREMENTS IN THE TRISONIC GAS-DYNAMICS
FACILITY USING PARTICLE IMAGE VELOCIMETERY WITH CO₂ SEEDING**

Daniel B. Wolfe, BS

Major, USAF

Approved:


Dr. Mark F. Reeder (Chairman)

8 March 2012
Date


Dr. Marc D. Polanka (Member)

8 MAR 12
Date


Capt James L. Rutledge, USAF (Member)

8 Mar 2012
Date

Abstract

Particle image velocimetry (PIV) is utilized with solid carbon dioxide (CO_2) seeding material to conduct boundary layer measurements in the test section of the Air Force Research Laboratory's Trisonic Gas-dynamics Facility (TGF), which has a 24 inch by 24 inch cross-section. Freestream velocity was set at Mach 0.3, Mach 0.5, or Mach 0.8 while stagnation pressure ranged from 500 to 2400 pounds per square foot (psf). High pressure liquid CO_2 was directed through expansion nozzles into shroud tubes which led to solidified particles in the wind tunnel stagnation chamber. Two different sets of shroud tubes were used to modify the size of dry ice particles produced and the particle number density. Shroud tubes with an inside diameter (ID) of 0.824 inches provided good particle count and coverage for stagnation pressures between 500 and 1500 psf, while 0.364 inch ID shroud tubes demonstrated good particle count and coverage for stagnation pressures over 1000 psf. Overall, the PIV results produced freestream velocity measurements and boundary layer profiles which compared well with expected values. After initial processing, turbulence data closely followed trends expected within boundary layer, but levels were somewhat higher than anticipated. When the PIV data was processed using elliptical interrogation regions, elongated in the streamwise direction, resulting turbulence levels were much closer to expectations.

Acknowledgments

First, I would like to express my sincere appreciation to my faculty advisor, Dr. Mark Reeder, for his guidance and support throughout the course of my thesis work. His insight and direction were very much appreciated. I'd also like to thank Mr. John Hixenbaugh for his superb logistics support and expert plumbing skills. The test equipment you helped build was truly vital to the success of this research.

I'd also like to thank my sponsors at AFRL. Thank you to Mr. Tom Presdorf for your support and enthusiasm throughout this project. Mr. Shawn Raisch, Mr. Paul Olekas, and Mr. Keith Koon thank you for your support and expertise configuring the test equipment and running the TGF.

Finally, I would like to thank Mr. Ben Hagen, for his outstanding support throughout this entire process. Your expert knowledge on PIV techniques and willingness to share that information has helped immensely. Thank you for the countless hours you have spent working with me on this project.

Daniel B. Wolfe
Major, USAF

Table of Contents

	Page
Abstract	iv
Table of Contents	vi
List of Figures	viii
List of Tables	xi
 I. Introduction	 1
1.1 Motivation	2
1.2 Research Focus	4
 II. Background	 6
2.1 PIV Overview	6
2.1.1 Light Source	6
2.1.2 Flow Seeding	8
2.1.3 Image Acquisition and Correlation	11
2.2 CO ₂ Particle Formation and Characterization	16
2.3 Boundary Layer Properties	19
 III. Methodology	 23
3.1 Trisonic Gas-dynamics Facility	23
3.2 CO ₂ Particle Generation	26
3.2.1 Distribution Manifold Installation	31
3.3 PIV System	32
3.3.1 PIV Data Processing	38
 IV. Results and Discussion	 40
4.1 Record of Experiments Performed	40
4.2 Particle Size and Particle Number Density	42
4.3 Boundary Layer Calculations	50
4.3.1 Mach 0.3	50
4.3.2 Mach 0.5	57
4.3.3 Mach 0.8	60
4.3.4 Expected Boundary Layers	64
4.4 Planar Velocity Maps and Turbulence Data	67
4.4.1 Refined PIV Processing for Turbulence Measurements	74
4.5 Sources of Error	75

V. Conclusions and Recommendations	77
5.1 Overview of Research Effort.....	77
5.2 Conclusions	78
5.3 Impact of Research.....	80
5.4 Future Work	80
Appendix A. Wind Tunnel Instrumentation Data.....	82
Appendix B. Clauser Plots.....	85
Appendix C. Boundary Layer Profiles Compared to $1/7^{\text{th}}$ Power Law	92
Bibliography	94

List of Figures

Figure	Page
2.1	Essential PIV components.....7
2.2	The cross correlation process.....14
2.3	Correlation peak resulting when all particles have the same displacement.....15
2.4	Correlation peaks resulting when particles have different displacements.....15
2.5	Schematic of CO ₂ particle generation system.....16
2.6	Distribution of mean velocity from study by Klebanoff.....21
2.7	Distribution of turbulence intensities from study by Klebanoff.....22
2.8	Distribution of turbulent shearing stress from study by Klebanoff.....22
3.1	Side view of the TGF.....25
3.2	TGF performance chart for subsonic test section.....26
3.3	CO ₂ storage dewars.....28
3.4	CO ₂ distribution manifold installed in the TGF.....28
3.5	3/4 NPT pipe shroud tube drawing.....29
3.6	1/4 NPT pipe shroud tube drawing.....29
3.7	Shroud tube and particle size comparison.....30
3.8	Stereoscopic PIV setup for boundary layer measurements with laser sheet (green) and optical axis of cameras (blue).....34
3.9	Type 11 calibration plate.....35
3.10	Pre-calibration image from camera 1.....35
3.11	Pre-calibration image from camera 2.....36
3.12	Post-calibration, corrected image from camera 1.....36
3.13	Post-calibration, corrected image from camera 2.....37
3.14	Example of median filter operation.....39
4.1	Seeding from 0.824 inch ID shroud tubes at $M = 0.3$, $P = 500$ psf.....43
4.2	Seeding from 0.824 inch ID shroud tubes at $M = 0.3$, $P = 1042$ psf.....43
4.3	Seeding from 0.824 inch ID shroud tubes at $M = 0.3$, $P = 1531$ psf.....44
4.4	Seeding from 0.824 inch ID shroud tubes at $M = 0.3$, $P = 2018$ psf.....44
4.5	Seeding from 0.824 inch ID shroud tubes at $M = 0.3$, $P = 2395$ psf.....45

4.6	Seeding from 0.824 inch ID shroud tubes at $M = 0.5$, $P = 1044$ psf.....	46
4.7	Seeding from 0.364 inch ID shroud tubes at $M = 0.5$, $P = 1042$ psf.....	46
4.8	Seeding from 0.364 inch ID shroud tubes at $M = 0.3$, $P = 750$ psf.....	47
4.9	Vector map of image pair with low particle number density.....	48
4.10	Seeding from 0.824 inch ID shroud tubes at $M = 0.8$, $P = 1044$ psf.....	49
4.11	Vector map of a single image pair captured at $M = 0.8$, $P = 1044$ psf.....	49
4.12	Flow field vector map for 0.824 inch ID shroud tubes at $M = 0.3$, $P = 550$ psf with red box indicating area affected by laser light reflections.....	51
4.13	Velocity profile for 0.824 inch ID shroud tubes at $M = 0.3$, $P = 550$ psf.....	52
4.14	Velocity profile for 0.824 inch ID shroud tubes at $M = 0.3$, $P = 1042$ psf.....	53
4.15	Velocity profile for 0.824 inch ID shroud tubes at $M = 0.3$, $P = 1531$ psf.....	53
4.16	Velocity profile for 0.824 inch ID shroud tubes at $M = 0.3$, $P = 2018$ psf.....	54
4.17	Velocity profile for 0.824 inch ID shroud tubes at $M = 0.3$, $P = 2395$ psf.....	55
4.18	Velocity profile for 0.364 inch ID shroud tubes at $M = 0.3$, $P = 1530$ psf.....	56
4.19	Boundary layer comparison using 0.824 inch ID and 0.364 inch ID shroud tubes at $M = 0.3$, $P = 1530$ psf.....	56
4.20	Velocity profile for 0.824 inch ID shroud tubes at $M = 0.5$, $P = 1044$ psf.....	58
4.21	Velocity profile for 0.364 inch ID shroud tubes at $M = 0.5$, $P = 1042$ psf.....	58
4.22	Boundary layer comparison using 0.824 inch ID and 0.364 inch ID shroud tubes at $M = 0.5$, $P = 1044$ psf.....	59
4.23	Velocity profile for 0.364 inch ID shroud tubes at $M = 0.5$, $P = 1530$ psf.....	60
4.24	Velocity profile for 0.824 inch ID shroud tubes at $M = 0.8$, $P = 798$ psf.....	61
4.25	Velocity profile for 0.824 inch ID shroud tubes at $M = 0.82$, $P = 1044$ psf.....	62
4.26	Velocity profile for 0.824 inch ID shroud tubes at $M = 0.82$, $P = 1239$ psf.....	62
4.27	Velocity profile for 0.364 inch ID shroud tubes at $M = 0.84$, $P = 1045$ psf.....	63
4.28	Velocity profile for 0.364 inch ID shroud tubes at $M = 0.79$, $P = 1525$ psf.....	64
4.29	Calculated versus measured 90% boundary layer thickness.....	66
4.30	Flow field vector map for Experiment 33, $M = 0.5$, $P = 1044$ psf.....	67
4.31	Valid vector count for Experiment 33, $M = 0.5$, $P = 1044$ psf.....	68
4.32	Streamwise velocity (V_x) for Experiment 33, $M = 0.5$, $P = 1044$ psf.....	69
4.33	Streamwise velocity (V_x) for Experiment 33, $M = 0.5$, $P = 1044$ psf.....	69

4.34	RMS streamwise velocity (V_x'), Experiment 33, $M = 0.5$, $P = 1044$ psf.....	70
4.35	RMS perpendicular velocity (V_y'), Experiment 33, $M = 0.5$, $P = 1044$ psf.....	70
4.36	Absolute value of Reynolds stress ($V_x'V_y'$), Experiment 33, $M = 0.5$, $P = 1044$ psf.....	71
4.37	Turbulence data for Experiment 33, $M = 0.5$, $P = 1044$ psf.....	72
4.38	Turbulence data for Experiment 25, $M = 0.3$, $P = 1042$ psf.....	73
4.39	Turbulence data for Experiment 31, $M = 0.8$, $P = 1044$ psf.....	73
4.40	Improved turbulence data for Experiment 33, $M = 0.5$, $P = 1044$ psf.....	75

List of Tables

Table		Page
2.1	Common seeding materials for gas flows.....	8
4.1	Record of experiments performed.....	41
4.2	Comparison of calculated and measured boundary layer thickness.....	66

BOUNDARY LAYER MEASUREMENTS IN THE TRISONIC GAS-DYNAMICS FACILITY USING PARTICLE IMAGE VELOCIMETERY WITH CO₂ SEEDING

I. Introduction

The history of aviation has extended over more than two thousand years starting with the earliest attempts to fly kites in China around 200 BC, to the first powered heavier-than-air flight by the Wright brothers in 1903, and leading to the modern supersonic and hypersonic aircraft of today [1]. Developments in aeronautical science and engineering have made world travel easy and efficient, has revolutionized the way warfare is conducted, and was a vital stepping stone into space exploration. In modern history, the field of Aeronautical Engineering has been highly dependent on theory, observation, and experimentation to improve our understanding of fluid mechanics and aircraft design.

The fundamental theories, concepts and equations developed by men like Newton, Bernoulli, Euler, Navier, Stokes, Reynolds, and Prandtl, are the foundation from which human flight in heavier-than-air machines was made possible. In the early 1900s, after several setbacks, the Wright brothers designed and built a wind tunnel to develop their own calculations for airfoil lift and drag. These calculations ultimately provided the data needed to design and build the first successful powered aircraft [1]. Wind tunnels continue to play an important role in the study of fluid mechanics and Aeronautical Engineering. Computer modeling has proven to be a powerful tool in recent years. However, there are numerous instances where actual experimental data of fluid motion is required.

1.1 Motivation

Numerous methods exist to collect experimental data in wind tunnels in order to understand the complex science of fluid mechanics. Each method has distinct advantages and disadvantages which must be taken into consideration prior to the execution of each experiment. For instance, single-point methods like hot-wire anemometry and laser-Doppler anemometry provide a quantitative and accurate sample of the flow at a given point. These methods however, are not able to capture instantaneous flow field data over an entire test region. With the recent development of digital camera technology and the software to efficiently process digital images it is now possible to develop new measurement techniques that are able to simultaneously provide instantaneous spatial flow field visualization and quantitative results. One of the most successful measurement methods to materialize in the past three decades is particle image velocimetry (PIV) [2].

PIV is based on the simple principle that velocity equals the distance traveled per unit of time. If tracer particles can be introduced in a fluid under the right conditions, the particles will move at the same speed as the fluid. Two digital images of the particles are captured over a known time increment and the distance traveled by the particles can be determined by comparing the first and second image. The velocity of the particles can then be determined by dividing this distance by the known time increment between the two images. In order for PIV to provide valuable data the particles must accurately follow the fluid motion and must not alter the fluid properties or flow characteristics [2].

This concept, while easy to understand, is much more complex in the application of experimental aerodynamic data collection as discussed in Chapter 2. Once these complexities are understood, a great deal of information can be collected about the fluid

flow in question. Using the resulting instantaneous flow field data from PIV, boundary layer effects, turbulence characteristics, vortex formation, and momentum thickness, for example, can be determined. As the applications of PIV in aerodynamics and water flows continue to grow, so does the interest in refining this technique to improve its accuracy as well as its practicality [3].

Unfortunately, in some cases the use of PIV is prohibitively inconvenient and costly. Typical seed materials for PIV, such as titanium dioxide, atomized oils, or theater smoke work well for blowdown facilities. However, these materials can lead to significant, and expensive, downtime for large closed-circuit wind tunnel facilities because of residue on the internal surfaces. The Air Force Research Laboratory's (AFRL) Trisonic Gas-dynamics Facility (TGF), is a closed-circuit wind tunnel capable of creating low subsonic, transonic, and supersonic conditions. In a previous test, an oil-based smoke was used in the TGF to seed the air flow. This caused a residue to build up on the tunnel walls and test section glass, requiring a substantial cleanup effort after the test. These seed materials can also adversely affect measurements executed using pressure- and temperature-sensitive paint. Also, many large-scale tunnel operators are deterred from PIV due to the potential fire hazard of seed materials like polystyrene, ethylene glycol, propylene glycol, ethyl alcohol and acetone. These materials have flash points and auto-ignition temperatures that are near or below the compressor operating temperatures in many closed-circuit tunnels [4]. Water particles have been used in the past also, but increase the probability of tunnel component corrosion and damage to electronic systems. Numerous examples of oil- and water-based seeding are available, including experiments at the Arnold Engineering Development Center's 16T wind tunnel.

Results show if these seed materials can be replaced with clean seeding methods, many facilities could benefit [5]. The search for a clean seeding material has resulted in the recent study of solid carbon dioxide (CO_2), or dry ice. CO_2 can exist as a solid and then sublime, leaving no trace or residue other than the naturally occurring inert gas which mixes into the surrounding air. If dry ice particles can be created, introduced into the air flow, and if they persist long enough to pass through the test section prior to sublimating, they would negate any need for additional maintenance on the wind tunnel due to PIV testing.

1.2 Research Focus

It is important to select a proper seeding material that will allow collection of accurate PIV data and not negatively impact the operation of wind tunnel facilities. The research presented here focuses on developing a method to properly size CO_2 particles and produce the amount of particles needed to collect accurate PIV data in a production scale tunnel. The particles must be small enough to accurately track the fluid flow and also be large enough to scatter a sufficient amount of light to be captured by the sensor of a digital camera. Also, the particle density must be close enough to the fluid density to minimize the effects of gravity and velocity discrepancies between the particle and the surrounding fluid. Finally, the density of particles in the test section must be adequate in order to maximize the resolution of the velocity vector field.

The overarching goal of this research is to take the next step toward developing a fully operational PIV capability at the TGF for AFRL and its customers. Previous work by Brian Love, under the direction of Dr. Mark Reeder, demonstrated the feasibility of

collecting PIV data in the TGF [6, 7]. This research refines their methods with the following goals:

- Produce seed particles of consistent size which are suitable for PIV
- Produce a consistent distribution of seed particles throughout the TGF test section
- Analyze the TGF test section boundary layer normal to the window at various

Mach numbers and various pressures

Previously, three different injectors of various sizes were used to seed the TGF. Several injection methods and injection locations were tested to find a suitable solution to the seeding problem. During these experiments, only one injector at a time was used which resulted in insufficient particle coverage and limited PIV data collection to basic freestream velocity measurements [6, 7]. The research presented in the following chapters discusses the work done to improve upon this work with the goals listed above.

II. Background

In this chapter, background information is provided on PIV techniques used for this research. First, the basic principles of PIV are discussed, including the component pieces required to collect PIV data. Flow seeding is covered in more detail because of its importance in this research. Recent research pertaining to clean-seeding is discussed. Finally, the theory of boundary layer development and the relevant mathematical relations thereof are discussed.

2.1 *PIV Overview*

In recent years PIV instrumentation and data processing techniques have undergone rapid development. While early applications used photographic recording, current techniques rely almost exclusively on digital charge coupled device (CCD) cameras and advanced software algorithms to correlate particle motion between different digital images. A basic PIV configuration is shown in Figure 2.1. Essential components of this technique are flow seeding particles, a light source, imaging optics and imaging sensor. These components are briefly described in the following sections. For an in depth review of PIV please refer to the text by Adrian and Westerweel [3].

2.1.1 *Light Source*

Light is required to illuminate the seed particles adequately to be detected by the digital camera sensor. Typically lasers are used because they emit collimated, monochromatic light with a high energy density and can be easily directed through optics

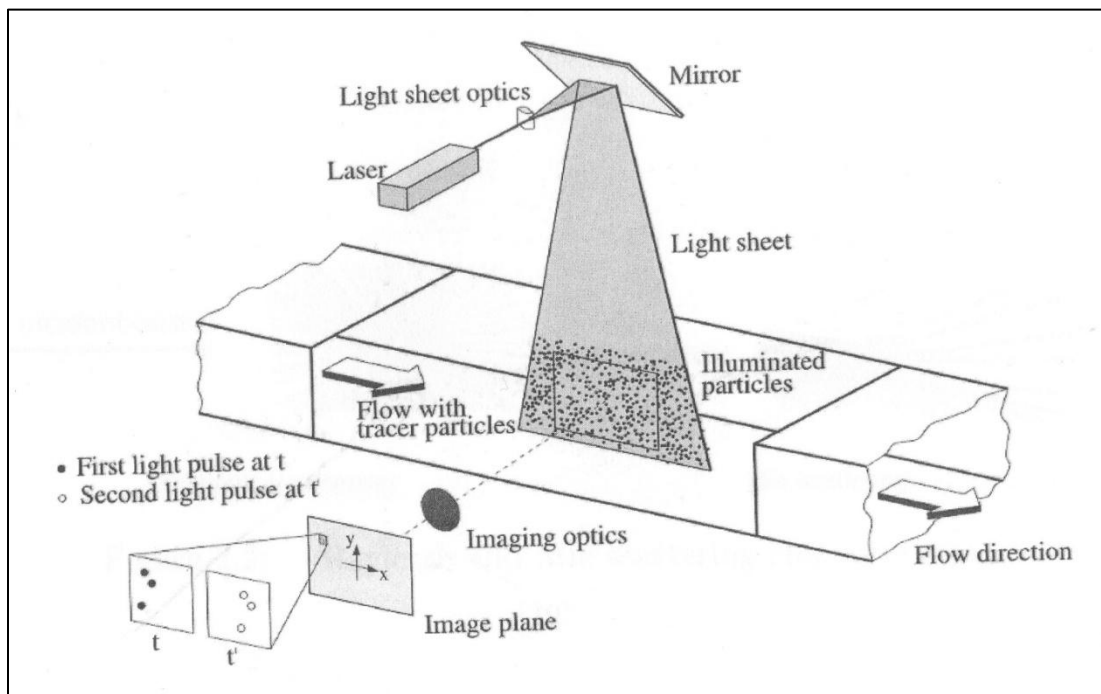


Figure 2.1: Essential PIV components.

[8]

to produce a light sheet. The most common type of laser used for PIV experiments is the neodymium-doped yttrium-aluminum-garnet (Nd:YAG) laser. Nd:YAG lasers produce light with a wavelength of 1064 nm that is then frequency doubled to achieve a wavelength of 532 nm in the visible green spectrum [2]. They produce pulse energies between 10mJ and 1J and very short pulse durations ranging from 5-15ns making them ideal for PIV.

Determining the proper light source is also dependent on the seed particles' light scattering properties. Table 2.1 lists typical air flow seed materials and their diameters. These particles have a diameter larger than the wavelength of the light source and scatter light according to the Mie theory [2]. According to this theory a majority of the light is scattered in the forward direction, the same direction as the incident light energy, and less is scattered backwards and to the sides. For single-camera PIV the optical axis is usually arranged normal to the light-sheet plane, to minimize image distortion. Nd:YAG pulsed

lasers are often used in PIV because they provide a large amount of light energy over a short time duration, usually less than 10 nanoseconds, which can be collected by the sensor in a CCD camera.

Table 2.1: Common seeding materials for gas flows [8].

Type	Material	Mean diameter in μm
Solid	Polystyrene	0.5 – 10
	Alumina Al_2O_3	0.2 – 5
	Titania TiO_2	0.1 – 5
	Glass micro-spheres	0.2 – 3
	Granules for synthetic coatings	10 – 50
	Dioctylphthalate	1 – 10
	Smoke	< 1
Liquid	Various oils	0.5 – 10
	Di-ethyl-hexyl-sebacate (DEHS)	0.5 – 1.5
	Helium-filled soap bubbles	1000 – 3000

2.1.2 Flow Seeding

PIV methods rely on the presence of particles in the flow that not only follow changes in the flow velocity but are also sufficient in number to provide the desired resolution of the measured flow velocity. Selecting a seeding material requires balancing two parameters. First, the seed particles must be large enough to scatter sufficient light as discussed in the previous section. Second, the seed particles must be small enough to also respond quickly to the dynamic changes that occur in the flow being studied. The size criterion for flow-following is characterized by the Stokes' number. The seeding materials shown in Table 2.1 are commonly used for PIV because they often satisfy both criteria.

The background of the development of Stokes' number criteria is as follows. The equation of motion of a small spherical particle immersed in a viscous fluid flow, originally developed by Basset and independently derived by Boussinesq and Oseen (BBO Equation) [2], is given as:

$$\begin{aligned} \frac{4}{3}\pi a^3 \rho_p \frac{dv}{dt} = & \frac{4}{3}\pi a^3 \rho_f \frac{dV}{dt} + \frac{4}{3}\pi a^3 (\rho_p - \rho_f)g - 6\pi\mu a \left[(v_p - U) - \frac{1}{6}a^2 \nabla^2 U \right] \\ & - 6\pi\mu a^2 \int_0^t \frac{d}{d\tau} \left[(v_p - U) - \frac{1}{6}a^2 \nabla^2 U \right] \frac{d\tau}{\sqrt{v(t-\tau)}} - \frac{2}{3}\pi a^3 \frac{d}{dt} \left[(v_p - U) - \frac{1}{10}a^2 \nabla^2 U \right] + L \end{aligned} \quad (2.1)$$

where

$$a = \frac{d_p}{2} = \text{tracer particle radius}$$

$$\rho_p = \text{particle density}$$

$$\rho_f = \text{fluid density}$$

$$g = \text{gravity}$$

$$\mu = \text{fluid viscosity}$$

$$v_p = \text{particle velocity}$$

$$U = \text{fluid flow velocity}$$

$$L = \text{lift force}$$

Particle mass multiplied by acceleration is the left-hand side of Equation (2.1). The terms on the right-hand side of the equation are, in order, the non-inertial force, net body force, quasi-steady viscous force, time history force, added mass force, and the lift force. Various forms of the BBO Equation appear in texts by Melling [9] and Tropea, et al. [2].

For very small particles as used in PIV the quasi-steady viscous term (Stokes drag) dominates the right-hand side of Equation (2.1). The approximation that dU/dt equals dv_p/dt allows the difference between the particle velocity, v_p , and that of the surrounding fluid, U , to be estimated as:

$$v_p - U = \frac{2}{9} \frac{a^2(\rho_p - \rho_f)}{\mu} \frac{dv_p}{dt} \quad (2.2)$$

The difference in velocity, $v_p - U$, is called the slip velocity. It is apparent from Equation (2.2) the selection of neutrally buoyant particles, $\rho_p - \rho_f = 0$, results in tracers that accurately follow the fluid flow. This condition is easily satisfied for liquid flows, but is much more difficult to achieve in gas flows where particle density is on the order of 10^3 greater than the fluid [2]. In the case where $\rho_p/\rho_f \gg 1$, a single exponential decay law is used to model the particle response to a stepwise variation in the flow velocity. The characteristic response time of the particle is defined as

$$\tau = \frac{2}{9} a^2 \frac{\rho_p - \rho_f}{\mu} \quad (2.3)$$

The particle response time should be kept smaller than the smallest time scale of the flow (τ_f). The accuracy of the flow tracers in turbulent flows is quantified by the particle Stokes' number, S_k , defined as the ratio between τ and τ_f . According to the literature when $S_k < 0.1$, particle tracing of the flow will achieve acceptable accuracy with errors

below 1% [2]. Instead of using a characteristic response time, Melling calculated a characteristic frequency, C , from the BBO Equation resulting in Equation (2.4).

$$C = \frac{18\mu}{\rho_p d_p^2} \quad (2.4)$$

Frequency is equal to $1/\tau$, and it can easily be shown with simple algebra that Equation (2.3) is equivalent to Equation (2.4).

$$\frac{1}{\tau} = \frac{9\mu}{2a^2\rho_p} = \frac{9\mu}{2\left(\frac{1}{2}d_p\right)^2\rho_p} = \frac{18\mu}{d_p^2\rho_p} = C \quad (2.5)$$

2.1.3 Image Acquisition and Correlation

In the past, PIV images were captured on film with 35mm cameras. Today, digital cameras are used to capture a large quantity of images quickly. CCD and complementary metal-oxide semiconductor (CMOS) sensors convert light energy into electrical energy which is used to produce a digital image. Both sensor types are extremely sensitive to light so low ambient light conditions are needed to properly capture images of the seed particles and minimize background noise and reflections.

Using a light sheet, formed by passing a double pulsed laser beam through an optical arrangement, the particles in the flow are illuminated twice with a small time separation between. A digital camera is typically positioned perpendicular to the plane of

the light sheet and its shutter timed to capture the light scattered by the particles. The displacement of particles in the time between the laser pulses is recorded as a pair of two single exposure images. The recorded particle displacement field is measured locally across the whole field of view of the images, scaled by the image magnification and then divided by the known pulse separation time increment to obtain flow velocity at each point. Depending on the flow velocity and the camera lens magnification factor the delay of the two pulses must be determined so adequate displacements of the particle images on the CCD or CMOS are obtained [10].

The large number of digital images combined with the number of particles per image, requires the use of sophisticated software to process the vector fields. A variety of PIV analysis techniques exist, but all methods are based on a statistical cross-correlation algorithm [3]. This method breaks the image pairs down into a grid of interrogation regions (IR) as seen in Figure 2.2. Typically, each IR is a non-overlapping square made up of 128×128 , 64×64 , or 32×32 pixels, and the physical size of each IR can range from micrometers to centimeters, depending on the field of view of the camera. According to the LaVision, PIV software manual, best results from this method are obtained when a minimum of ten particles are present in each IR [10]. The first step in acquiring a flow field vector map is the analysis of the IRs in the frequency domain using fast Fourier transforms (FFT). An IR from the first image is compared pixel by pixel to the same IR in the second image. A peak occurs when the particle reflections in image one match the particle reflections in image two. This correlation peak will be much higher when all particles in the IR have approximately the same displacement as seen in Figure 2.3. If the particles do not all move with the same velocity, the displacement

found by correlation is approximately an average over the particles and will result in several peaks of lower amplitude as seen in Figure 2.4. The correlation, performed in the frequency domain, is converted back into the time domain through an inverse Fourier transform. The result is a vector map of each particle's pixel displacement between the two images. Initial calibration images are taken in order to determine the number of pixels per unit length known as the scale factor. With the known pixel displacement and known time step between images the velocity vector map of each IR can easily be calculated. This process is executed for all IRs and results in an instantaneous velocity vector map over the entire flow field. Post-processing of the vectors may be accomplished using filters and analysis methods including peak filters, IR shifting, overlapping, and local averaging. Proper post-processing will result in increased accuracy and spatial resolution of the vector field. Figure 2.2 below shows the entire PIV correlation process with a near-ideal result of the peak detection.

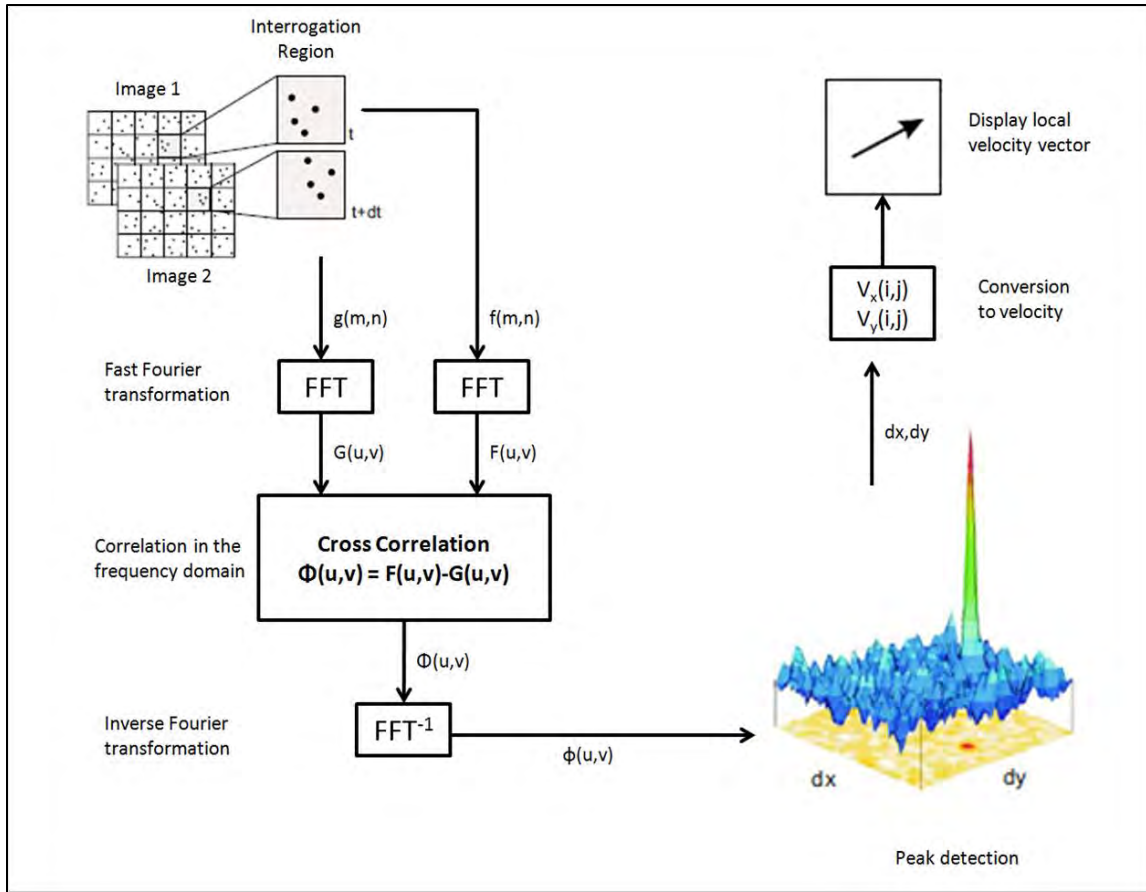


Figure 2.2: The cross correlation process.

[10]

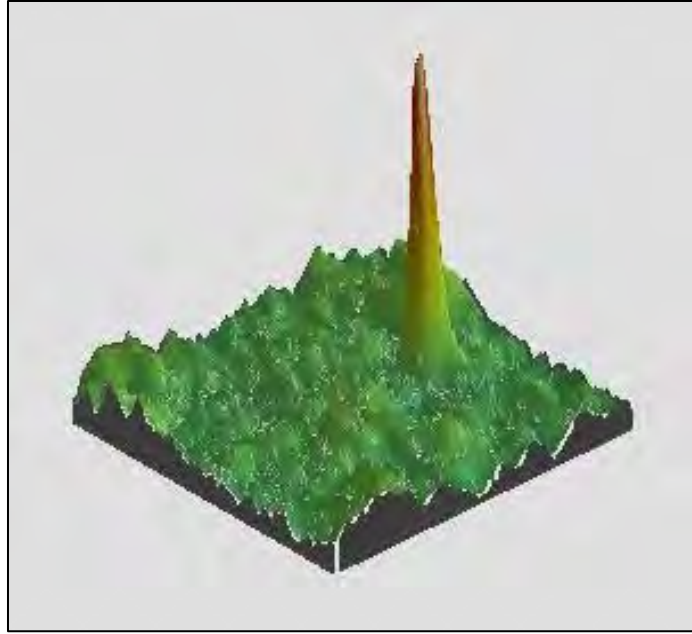


Figure 2.3: Correlation peak resulting when all particles have the same displacement.

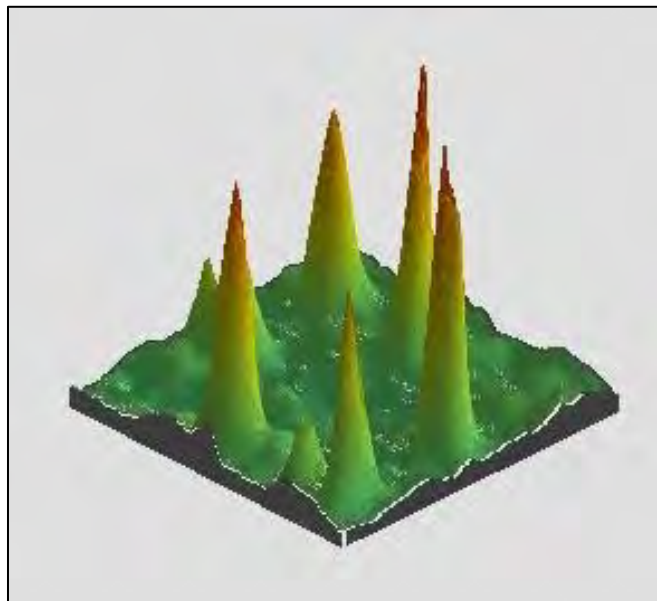


Figure 2.4: Correlation peaks resulting when particles have different displacements.

2.2 *CO₂ Particle Formation and Characterization*

Creating discrete particles for PIV using CO₂ has been the focus of several researchers within the last decade and is well documented [4, 6, 7, 11, 12]. Particle production requires a high-pressure dewar of CO₂ which is equipped with a siphon tube to access the liquid in the bottom of the container. The liquid CO₂ is drawn up the siphon tube and directed through a small diameter expansion nozzle. Attached to the nozzle is a larger diameter shroud tube as seen in Figure 2.5. When the CO₂ expands through the nozzle some of the liquid evaporates and lowers the temperature of the remaining liquid spray to form solid particles. The small particles then combine with each other, or agglomerate, to form larger particles of various sizes inside the shroud tube.

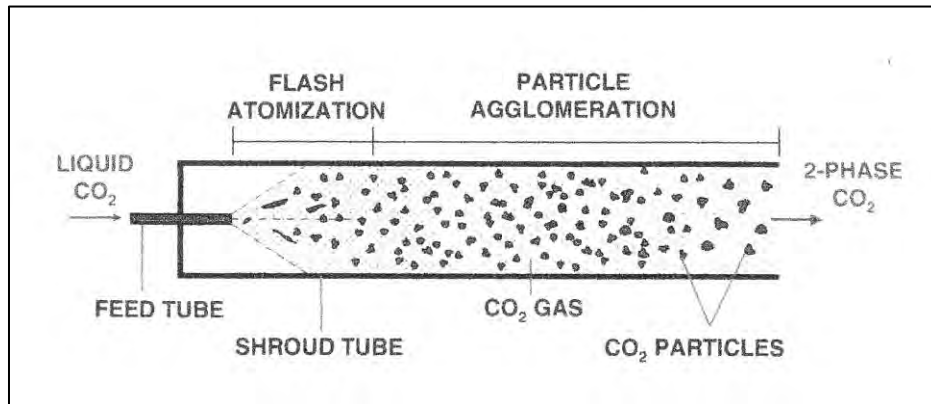


Figure 2.5: Schematic of CO₂ particle generation system.

[4]

The use of CO₂ to form clean seeding particles for PIV measurements has been studied at AFIT and AFRL in cooperation with Innovative Scientific Solutions, Inc. for several years. Initial work was described by DeLapp, et al. in 2006 [12], where a commercially available system called the Sno-Gun II was used to generate dry ice particles. Several nozzles of varying diameter were used to create particles of different size which were then measured using a Malvern particle size analyzer. The results of this research showed that CO₂ particles measuring between 5 to 15 μm could be created using this technique.

Further work by McNiel et al. built on the work of DeLapp to determine if discrete particles could be created and injected into the air flow of a wind tunnel for PIV [13]. This research focused on two methods for particle injection including a capped, multi-port shroud tube and a simple, uncapped shroud tube. The multi-port system, absent shroud tubes, proved unable to produce CO₂ particles and only created gaseous clouds through the test section. Successful results were obtained using the simple shroud tube. Discrete particles were created, injected in the flow, and did not sublime prior to reaching the test section of the wind tunnel [13].

McNiel et al. also explored using various combinations of small and large tubes to control the expansion of CO₂ in order to produce seed particles [13]. Greene then researched the effects of varying the size of the feed tube and shroud tube diameters on particle size. He also studied how insulating the shroud tubes would affect the size of the particles [11]. Greene documented that increasing the length of the shroud tube, increasing the inner diameter of the shroud tube, decreasing the inner diameter of the feed tube, and insulating the shroud tube each increased the size of particles generated.

Reversing any of these parameters would result in particles of smaller size [11]. Greene was able to successfully inject particles and collect PIV data in the AFIT 2.5 x 2.5 inch supersonic wind tunnel. Attempts to scale this technique up to the larger 6 x 6.5 inch supersonic blow-down tunnel resulted in decreased particle number density. An increase in the air mass flow rate for the larger tunnel and the greater distance between the injection site and the test section caused more of the CO₂ particles to sublime prior to reaching the test section [11].

Research by Love in 2008 focused on improving the method of particle generation and quantifying particle response time for flow across a shock in the 6 x 6.5 inch tunnel at AFIT [7]. Again, feed tubes and shroud tubes of different sizes were tested in addition to the use of a static mixing shroud tube. The particles generated using the static mixing shroud tube were approximately three times smaller than particles made by open flow shroud tubes of the same diameter. Love also led the first attempt at CO₂ clean seeding for PIV measurement in the TGF at AFRL Air Vehicles Directorate. Tests were successfully performed at three subsonic speeds and four stagnation pressures. PIV data were successfully collected in the tunnel freestream in each case and streamwise velocities matched expected values [7]. However, due to the limited optical access of the TGF, the light-sheet plane used to collect data was rotated at an angle. This angle was not orthogonal to the tunnel surfaces making it impractical to accurately study boundary layer conditions in the test section. A main goal of the research in this thesis is to accurately capture the boundary layer conditions in the TGF at several Mach numbers and stagnation pressures.

2.3 *Boundary Layer Properties*

The boundary layer is a thin region of flow adjacent to the surface, where the flow is slowed by the friction forces acting between the flow and the solid surface. Directly at the surface, the flow velocity is zero. This is known as the no-slip condition. Above the surface the velocity increases until it equals the freestream velocity. The thickness of this boundary layer, $\delta(x)$, is the height above the surface where the flow velocity equals 99% of the freestream velocity. Due to differences in laminar and turbulent flow, two mathematical models are used to calculate boundary layer thickness over a flat plate [14]. For the laminar case

$$\delta(x) = \frac{5.0x}{\sqrt{Re_x}} \quad (2.6)$$

where

x = horizontal distance over plate

Re_x = Reynolds number at x

The data collected in this research concentrates on turbulent flow fields. The equation for turbulent boundary layer thickness is as follows.

$$\delta(x) = \frac{0.37x}{Re_x^{(1/5)}} \quad (2.7)$$

Additionally, the text by Schlichting [15] developed two empirical models for a compressible turbulent boundary layer which relate the normalized velocity distribution, $\frac{U}{U_\infty}$, to the height above the plate, y , divided by the momentum thickness, δ_2 , and displacement thickness, δ_1 , as seen in Equations (2.8) and (2.9).

$$\frac{U}{U_\infty} = 0.683 \left(\frac{y}{\delta_2} \right)^{\frac{1}{7}} \quad (2.8)$$

$$\frac{U}{U_\infty} = 0.737 \left(\frac{y}{\delta_1} \right)^{0.1315} \quad (2.9)$$

In a turbulent compressible boundary layer, the ratio of boundary layer thickness to momentum thickness is $72/7$ and the ratio of boundary layer thickness to displacement thickness is 8.

$$\delta = \frac{72}{7} \delta_2 \quad (2.10)$$

$$\delta = 8 \delta_1 \quad (2.11)$$

In addition to determining mean velocity profiles, it is an understatement to say that many studies have focused on turbulence measurements in boundary layers. Klebanoff conducted similar wind tunnel studies in a large closed circuit tunnel of turbulent boundary layers over a 12 foot long plate using hot-wire anemometry [16], and the representation of his data offers a straightforward comparison to data collected as part

of this research. The mean velocity data from Klebanoff is given in Figure 2.6, where U_1 here represents the freestream velocity. Schlichting characterized the same results in terms of boundary layer thickness and showed that the 90 percent velocity location was located at approximately 0.50δ for this data set.

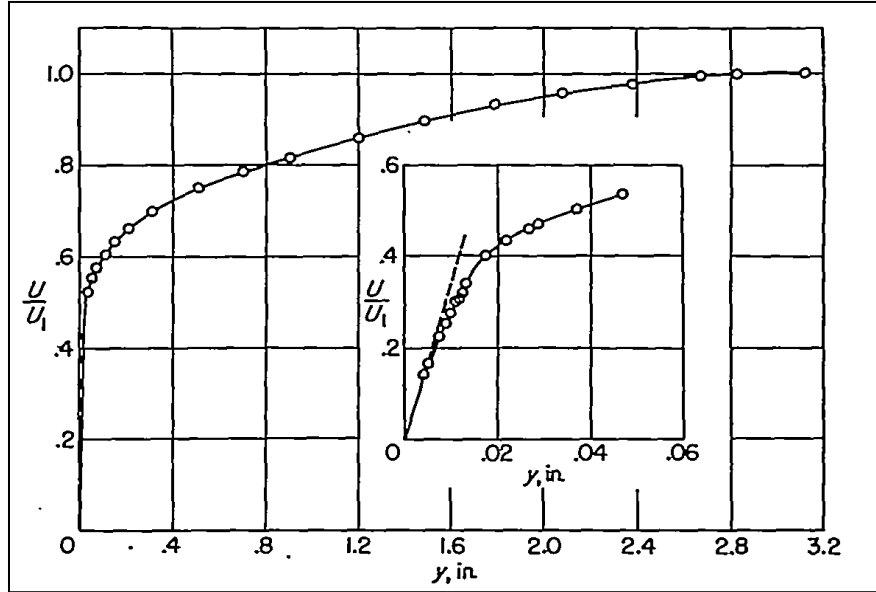


Figure 2.6: Distribution of mean velocity from study by Klebanoff.

[16]

Klebanoff used hot wire anemometry to determine the profiles. As shown in Figure 2.7, he found that the maximum streamwise turbulence was approximately 11% very close to the wall, while maximum turbulence normal to the flow was much lower, around 4%. In Figure 2.8, Reynolds shear stress normalized by one-half times the square of the freestream velocity obtained by Klebanoff is given, and it remains below 0.003. While many other, more modern, measurements of boundary layers have been performed,

this straightforward presentation by Klebanoff provides a highly useful benchmark for comparison of the PIV results obtained in this study.

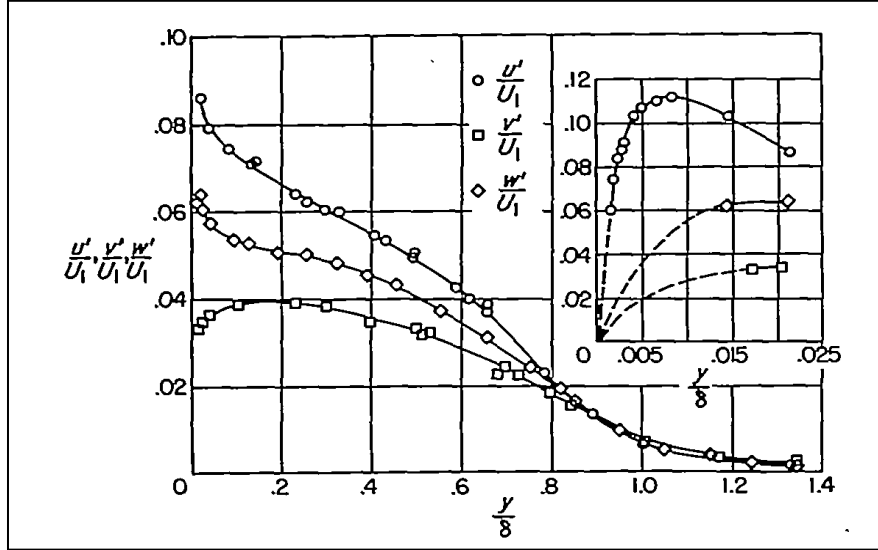


Figure 2.7: Distribution of turbulence intensities from study by Klebanoff.

[16]

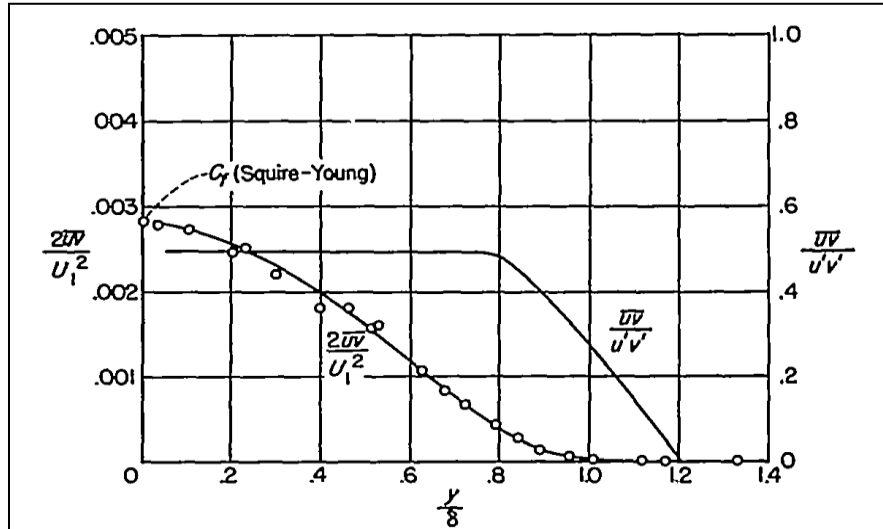


Figure 2.8: Distribution of turbulent shearing stress from study by Klebanoff.

[16]

III. Methodology

This chapter describes the test equipment and procedures used throughout this research project. First, the pertinent operational details of the TGF are covered. Next, the process for generating CO₂ particles is discussed. Finally, the PIV system and its setup are described.

3.1 *Trisonic Gas-dynamics Facility*

The TGF is an asset of AFRL Air Vehicles Directorate and is located at Wright-Patterson Air Force Base, OH. The TGF is a closed circuit, variable density, continuous flow wind tunnel capable of operating at subsonic, transonic, and supersonic speeds through a range of Mach numbers from 0.23 to 3.0 (Figure 3.1). Separate interchangeable nozzle blocks are used to operate in the supersonic flow regime. Tests for this research were performed at subsonic velocities only and utilized the subsonic nozzle blocks. The 2 x 2 foot subsonic test section can provide Mach numbers from approximately 0.23 to 0.85. At subsonic conditions the maximum achievable Reynolds number per foot is 2.5 million and the maximum attainable dynamic pressure is 350 pounds per square-foot (PSF). The TGF's subsonic operation envelope is shown in Figure 3.2.

The stagnation chamber inlet measures 8 x 8 feet and is 26 feet upstream of the test section windows. Two 28-inch diameter hinged windows are mounted on the test section sidewalls. These windows can be opened quickly to allow easy access to the models for configuration changes. In addition, the two optical quality glass windows allow the collection of Schlieren images, high-speed digital images, and PIV data.

PIV data, for this research, was collected on seven different days throughout the

month of September 2011. All experiments were conducted nominally at Mach 0.3, Mach 0.5, or Mach 0.8. Precise measurements of the tunnel conditions during each test run are presented in Chapter 4.

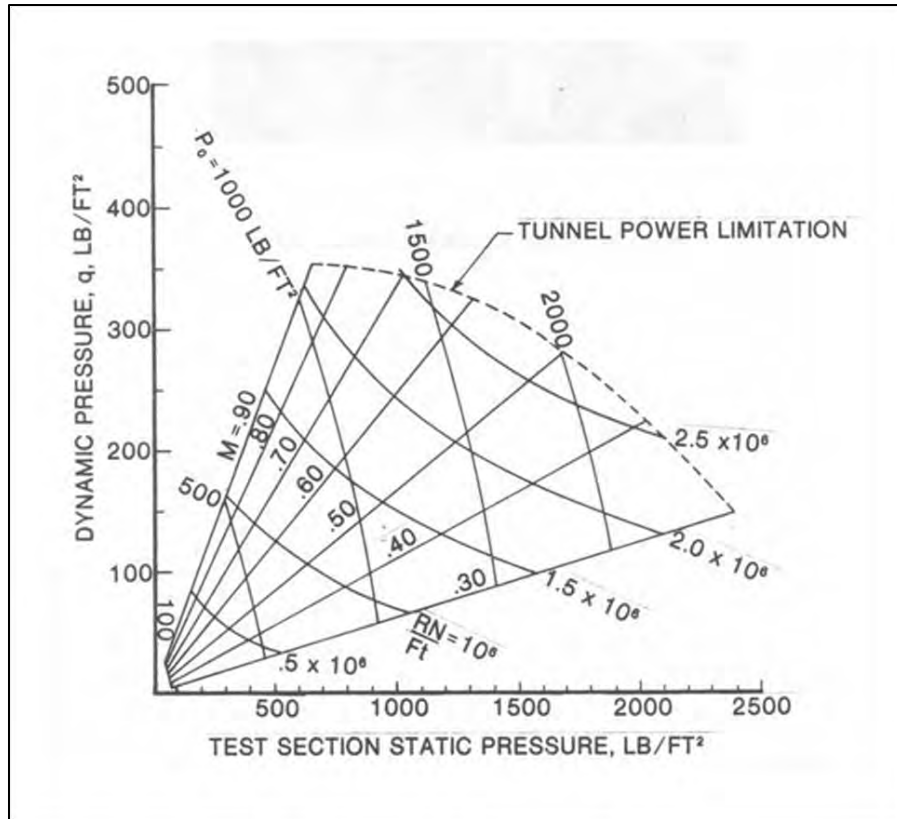


Figure 3.2: TGF performance chart for subsonic test section.

[17]

3.2 *CO₂ Particle Generation*

The liquid CO₂ (LCO₂) used throughout this project was stored in commercially available dewars as shown in Figure 3.3. The dewars have an internal volume of 180 liters and are pressurized to approximately 350 psi. The dewars are equipped with a siphon tube which draws the LCO₂ out from the bottom of the tanks. Two dewars are used simultaneously to feed the distribution manifold pictured in Figure 3.4. Pressurized LCO₂ flows from the dewars through high pressure, flexible, stainless steel Swagelok®

hoses and compression fittings to the top and bottom connection on the manifold. The LCO_2 then flows through nozzles where it expands, rapidly decreasing in pressure and temperature, and forms solid CO_2 particles. While the particles remain in the shroud tubes, they agglomerate and increase in size until exiting the tube.

The distribution manifold is constructed of 0.5 inch outer diameter, stainless steel tube with eight equally spaced connection points for the injector assemblies. Total overall length of the manifold is 22 inches and the injectors are spaced 2.3 inches apart on center. The eight connection points are threaded to accept standard 1/8 inch National Pipe Thread (NPT) fittings. One injector assembly consists of an expansion nozzle, a reducing coupling, and a shroud tube. Washjet®, 1/8-MEG-0002 expansion nozzles, with a 0.034 inch diameter orifice, were used for all experiments. Two different sizes of shroud tubes were used in order to create CO_2 particles of different size. Prior research by Greene [11] and Love [7] demonstrated that using larger diameter shroud tubes will increase the size of the particles while smaller diameter tubes will decrease the particles size. The first set of shroud tubes were 6 inch lengths of 3/4 inch NPT pipe which have an inside diameter of 0.824 inches as seen in Figure 3.5. The second set of shroud tubes consisted of 6 inch lengths of 1/4 inch NPT pipe which have an inside diameter of 0.364 inches as seen in Figure 3.6. A visual comparison of the particles generated by the different size shroud tubes can be seen in Figure 3.7.



Figure 3.3: CO₂ storage dewars.

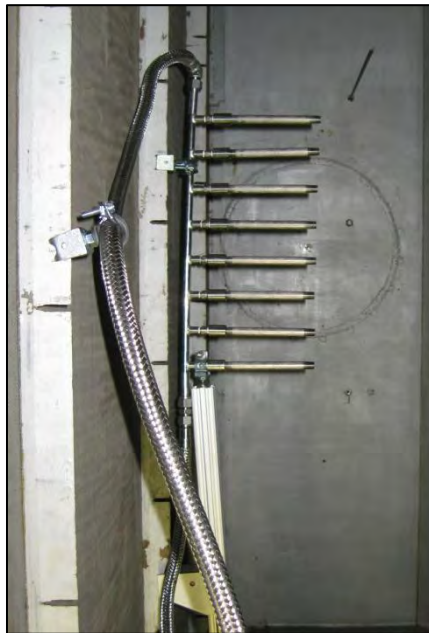


Figure 3.4: CO₂ distribution manifold installed in the TGF.

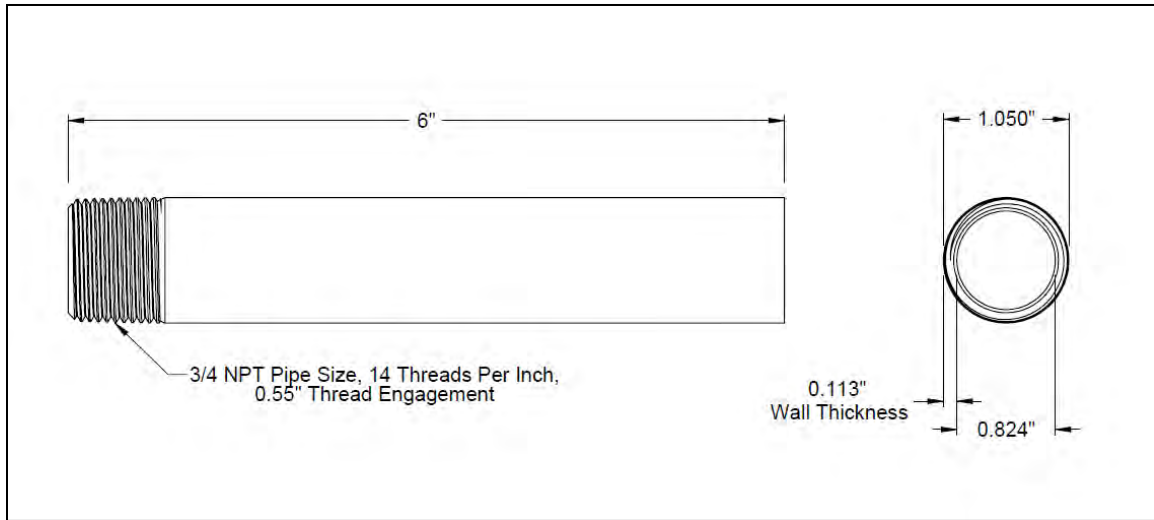


Figure 3.5: 3/4 NPT pipe shroud tube drawing.

[18]

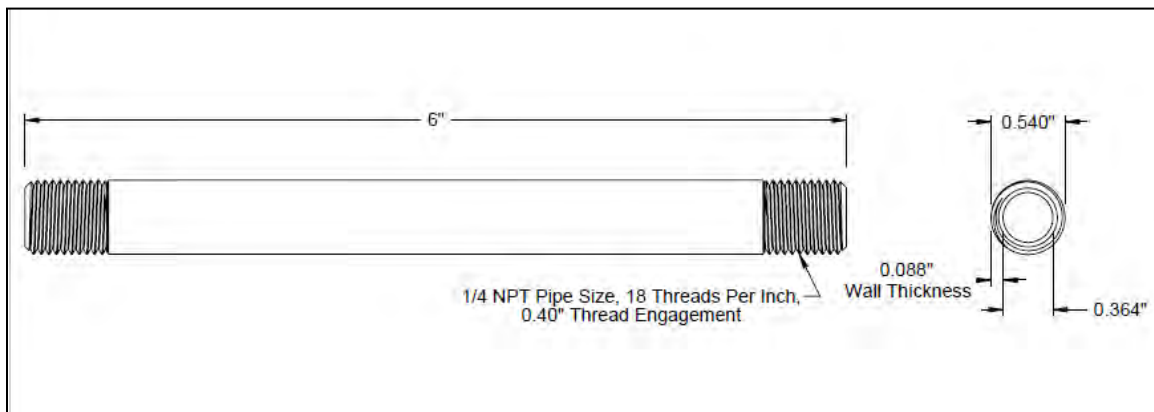


Figure 3.6: 1/4 NPT pipe shroud tube drawing.

[18]



1/4 NPT shroud tubes



3/4 NPT shroud tubes

Figure 3.7: Shroud tube and particle size comparison.

3.2.1 Distribution Manifold Installation

Prior to installation in the TGF, a drag force analysis of the CO₂ distribution manifold was done to ensure no damage would occur due to the manifold breaking free from its mounts. The drag force was calculated to be less than one pound at the tunnel's maximum operating limit. The safety review board, held by AFRL/RBAX, rated the CO₂ particle distribution system as low risk and approved it for installation in the TGF.

The manifold was mounted in three different configurations within the stagnation chamber of the TGF. This was done to optimize particle distribution in the test section for PIV measurements of the boundary layer perpendicular to the tunnel window. In all configurations the height of the manifold remained constant. The manifold center was aligned with the centerline of the test section when measured from the floor. In the first configuration, the manifold was mounted in the center of the stagnation chamber with the shroud tubes parallel to the flow direction. For the second configuration, the manifold remained mounted in the same location and the shroud tubes were rotated on the vertical axis approximately 40 degrees toward the wall. This forced the CO₂ particles closer to the wall of the tunnel where boundary layer measurements were taken. In the third configuration, the manifold was mounted close to the side wall of the stagnation chamber with the shroud tubes parallel to the flow direction. This was also done in an attempt to increase particle coverage near the wall of the test section to optimize PIV measurements of the boundary layer.

3.3 *PIV System*

A commercial, off-the-shelf, PIV system assembled and sold as a package by LaVision was used for this research project. This system consists of a LaVision computer with DaVis 7.2 software package, cameras, and a laser light source. Digital images were captured with two Imager Pro X 2M CCD cameras which have a 1600 x 1200 pixel array. Nikkor 55 mm f3.5 lenses were mounted on both cameras. The laser light sheet was produced by a New Wave Research Solo 200XT, Nd:YAG, frequency doubled laser operating at 532 nm and a maximum power of 200mJ. Precision timing of the laser pulses and camera shutters was controlled by the DaVis software in combination with the integrated Programmable Timing Unit Version 9 (PTU 9). The PTU 9 is a PCI board installed in the LaVision computer and is capable of highly accurate timing synchronization of up to 16 independent channels.

In conventional PIV experiments the camera optical axis is set up perpendicular to the plane of the laser light sheet. This arrangement provides the most direct method to capture two dimensional flow data on the plane of the light sheet. The limited optical access of the TGF prevents simple positioning of cameras perpendicular to the horizontal plane in the test section to study the boundary layer along the side wall or window. To accomplish the boundary layer study a backward-scatter, stereoscopic PIV technique was used. An overview of this approach has been described by Adrian and Westerweel [3] and in the LaVision FlowMaster manual [10]. Two cameras are set at an equal angle on opposite sides of the light sheet plane and the laser light is scattered backward to the cameras as seen in Figure 3.8. This technique not only enabled optical access perpendicular to the tunnel wall, it also enabled the capture of all three components of the

flow velocity, increasing the accuracy of the boundary layer measurements. Single camera PIV can still be accomplished in this configuration but the data may contain bias errors.

After the cameras and laser are mounted, the system must be calibrated to correctly scale the field of view. First, a Type 11, LaVision calibration plate was aligned horizontally with the light sheet plane. This calibration plate, seen in Figure 3.9, is three dimensional and has dots which are equally spaced 10 mm apart. Next, each camera is manually focused to obtain a clear image of each side of the plate. The LaVision software has an automated calibration program which then captures images of the calibration plate from each side, determines the location and angle of both cameras, then removes any warping in the images to correctly display 10 mm between each dot. Figure 3.10 is the pre-calibration image from camera 1, above the calibration plate, and Figure 3.11 is the pre-calibration image from camera 2, below the calibration plate. The corrected, post-calibration images of camera 1 and camera 2 are shown in Figure 3.12 and Figure 3.13 respectively.

The foam blocks seen in the calibration figures were put in place to protect the highly polished tunnel window from being scratched. As a result, there is an unknown separation between the window and the edge of the calibration plate which introduced some ambiguity as to the precise location of the wall measurement in the calibrated images. This ambiguity, of just 3 or 4 mm, resulted in large shifts of the data when plotted and is discussed in Chapter 4.

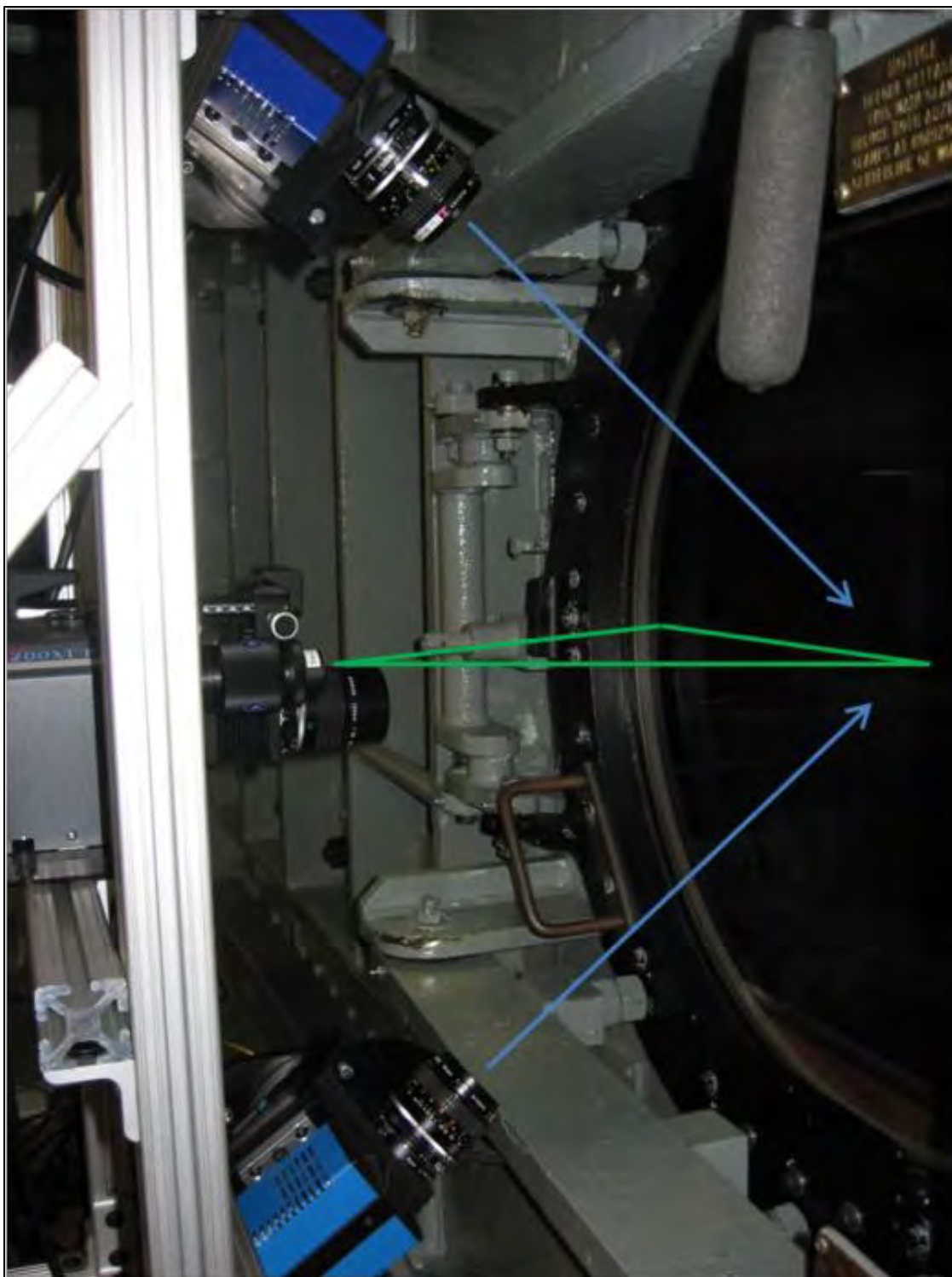


Figure 3.8: Stereoscopic PIV setup for boundary layer measurements with laser sheet (green) and optical axis of cameras (blue).



Figure 3.9: Type 11 calibration plate.

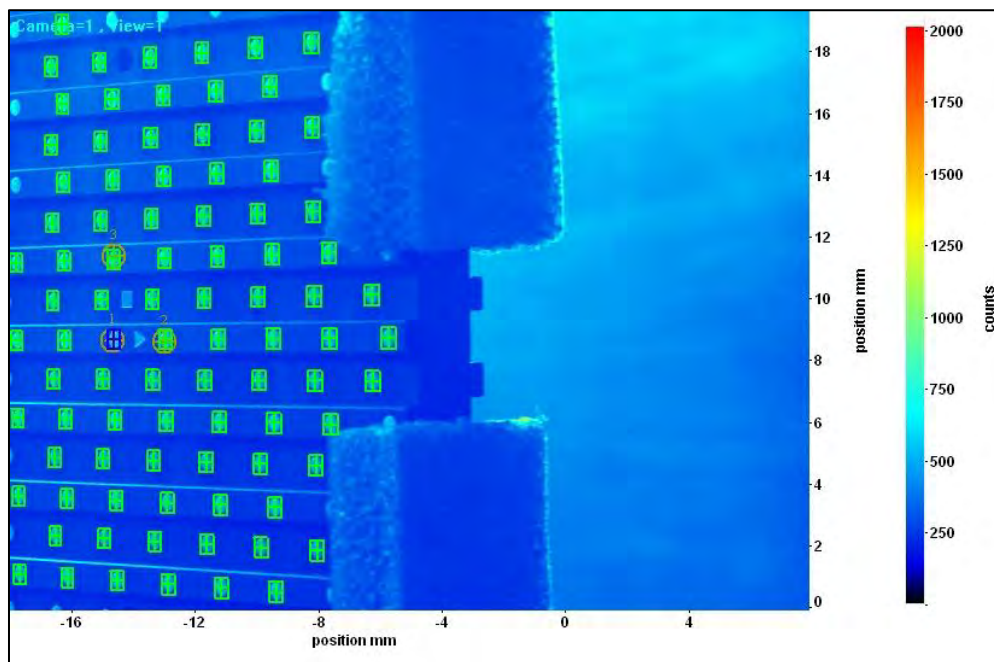


Figure 3.10: Pre-calibration image from camera 1.

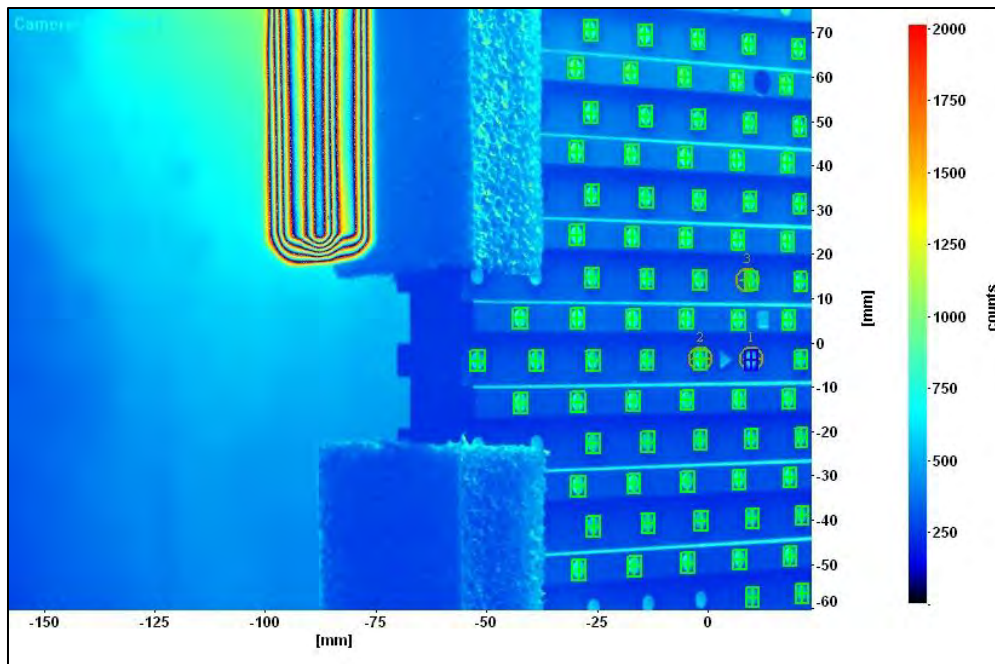


Figure 3.11: Pre-calibration image from camera 2.

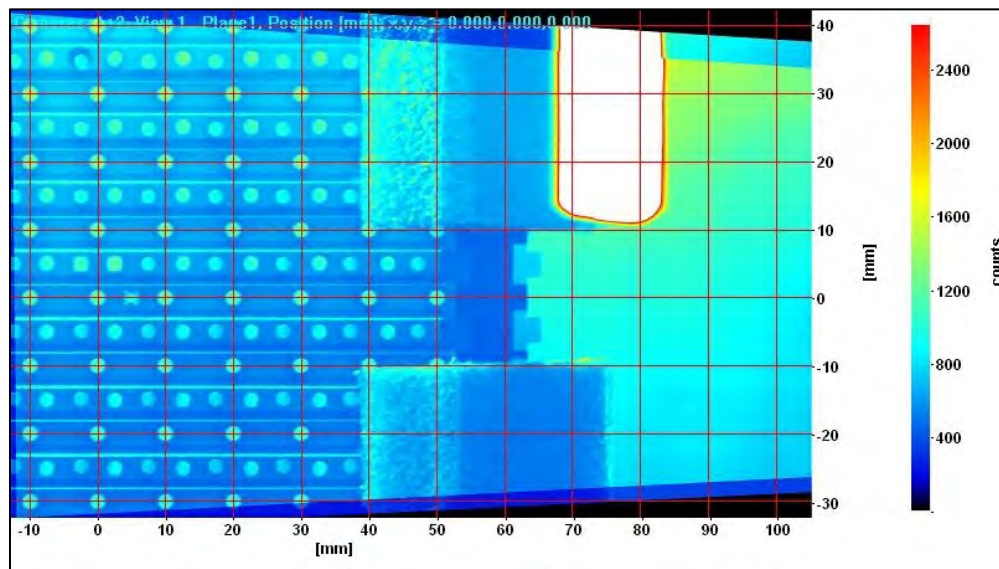


Figure 3.12: Post-calibration, corrected image from camera 1.

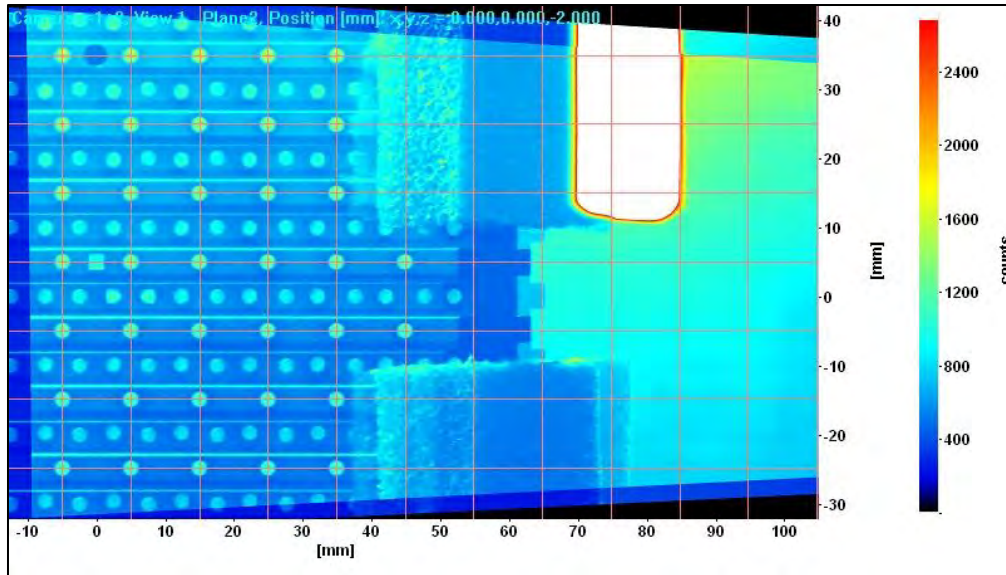


Figure 3.13: Post-calibration, corrected image from camera 2.

These corrected images provide a grid of known distance so the scale factor can then be calculated to determine the relative size of each pixel captured on the focal plane. The calibration process resulted in an image of the flow field with a field of view measuring 80 mm x 70 mm and a scale factor of 22.4264 pixels per mm. The software also calculated the focal length of the cameras to be 54.8352 mm. Laser and camera timing were adjusted to properly capture the flow velocity. This calibration was used for the tests which occurred between 8 September and 13 September.

The PIV system was needed for another experiment at a different facility so a new calibration was done on 21 September when the system was again set up at the TGF. This calibration resulted in a 120 mm x 70 mm field of view with a scale factor of 16.5479 pixels per mm. Camera focal length was calculated to be 46.1784 mm. This calibration was used during all tests of the smaller, 0.364 inch ID, shroud tubes on 21 September.

3.3.1 PIV Data Processing

Pre-processing of the image pairs started with a filter to reduce or eliminate reflections which contaminate the data. This process, called Subtracting a Sliding Background acts as a high pass filter where large intensity fluctuations in the background are filtered out while small intensity fluctuations of the particle signal will pass through. A scale length setting of four pixels produced the best results. The next process performed a standard Fast Fourier Transform cross-correlation using an initial interrogation region (IR) of 128 x 128 pixels followed by a smaller 64 x 64 pixel IR. The entire image was processed using a 50% overlap for both IR sizes.

The cross-correlation was followed by a peak validation using a value of 1.5 and a smoothing operation. The peak validation measures the relative height of the two tallest correlation peaks in an interrogation region and results in a valid vector if the height ratio of the tallest peak to the second tallest peak is 1.5 or greater. According to the LaVision Flow Master manual, a peak ratio setting between 1.2 and 1.5 is standard for PIV applications [10]. For multi-pass processing, as done in this research, the LaVison software uses a simple 3x3 smoothing filter to reduce noise by default.

Two operations were performed in the post-processing of the flow field vector map. First, a median filter was used which computes a median vector from the 8 neighboring vectors and compares the middle vector plus/minus a selected deviation of the neighbor vectors. The center vector is rejected when it is outside the specified range. Figure 3.14 provides an example of the median filter operation. In this example a median filter RMS setting of 1.4 or less will reject the center vector. The median filter

was set to 1 RMS of neighbors for this research. The second operation sets a minimum threshold for valid vectors at each location on the vector map. If this threshold is not met results will not be displayed for that location. A setting of 200 vectors was used for the experiments where 1000 images were captured. For the case where 10000 image pairs were taken, a minimum of 2000 valid vectors were required.

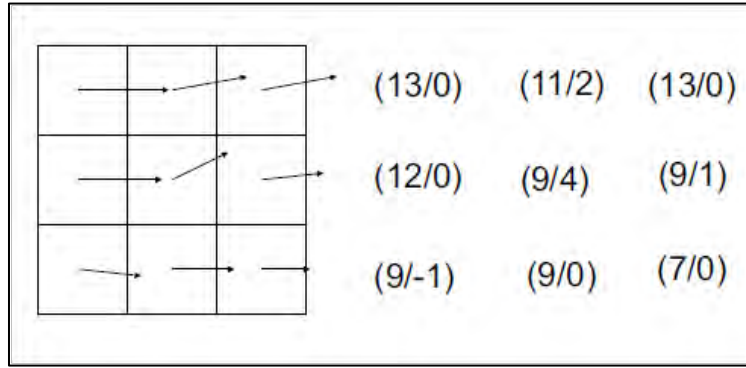


Figure 3.14: Example of median filter operation.

[10]

Two different methods were used to plot the results. The first method creates a two dimensional vector field of the flow field. The second method creates a scalar contour plot of several variables over the entire flow field. These variables include streamwise velocity, V_x , perpendicular velocity, V_y , RMS of streamwise velocity, v_x' , RMS of perpendicular velocity, v_y' , and Reynolds shear stress, $v_x'v_y'$. Reynolds shear stress is calculated by Equation (3.1).

$$v_x'v_y' = \frac{\sum_{i=1}^N [(V_{xi} - \bar{V}_x)(V_{yi} - \bar{V}_y)]}{N} \quad (3.1)$$

IV. Results and Discussion

Results for testing conducted at the TGF are presented below. First, a record of all the tests which were performed is discussed. Second, the dependency of CO₂ particle size and the particle number density in the test section on Mach number and stagnation pressure is presented. Third, based on the PIV data, boundary layer profiles are calculated for several Mach numbers and stagnation pressure combinations. Finally, results of turbulence data are presented.

4.1 Record of Experiments Performed

Experimental PIV data was collected at the TGF over a period of seven days throughout the month of September 2011. A total of 42 experiments, as seen in Table 4.1, were performed in which Mach number, stagnation pressure, shroud tube diameter, injection manifold location, and injection manifold angle to the flow direction were all varied in several combinations. Tests were run at nominal Mach numbers of 0.3, 0.5 and 0.8. Tunnel instrumentation recorded exact conditions for each experiment which are listed in Appendix A. Experiments 1 through 24 were primarily performed to make adjustments to the settings of the PIV equipment and CO₂ injection manifold. PIV data in some of these early experiments is less than optimal and is not analyzed in this document. However, results are presented for Experiments 25 through 42 where data was significantly better. In a majority of the experiments 1000 image pairs were captured for PIV analysis. In several tests only 100 image pairs were captured. These images were quickly analyzed and adjustments to the time between laser pulses (Δt) were made for each Mach number in order to optimize PIV results. In Experiment 33, ten thousand

image pairs were collected to provide a larger statistical sample for boundary layer turbulence analysis.

Table 4.1: Record of experiments performed.

Experiment Number	Date	Nominal Mach Number	Stagnation Pressure (lb/ft ²)	Δt (μs)	Number of Image Pairs	Shroud Tube Diameter (inches)	Injection Location	Injection Angle (degrees)
1	2-Sep-2011	0.3	550	10	1000	0.824	center	0
2	2-Sep-2011	0.3	1000	10	100	0.824	center	0
3	6-Sep-2011	0.3	300	10	1000	0.824	center	0
4	6-Sep-2011	0.3	400	10	1000	0.824	center	0
5	6-Sep-2011	0.3	500	10	1000	0.824	center	0
6	6-Sep-2011	0.3	600	10	1000	0.824	center	0
7	6-Sep-2011	0.3	800	10	1000	0.824	center	0
8	6-Sep-2011	0.3	1000	10	1000	0.824	center	0
9	6-Sep-2011	0.3	1300	10	100	0.824	center	0
10	6-Sep-2011	0.3	1700	10	100	0.824	center	0
11	6-Sep-2011	0.5	1000	8	100	0.824	center	40
12	7-Sep-2011	0.3	500	5	1000	0.824	center	40
13	7-Sep-2011	0.3	500	10	1000	0.824	center	40
14	7-Sep-2011	0.3	1000	5	1000	0.824	center	40
15	7-Sep-2011	0.3	1000	10	1000	0.824	center	40
16	7-Sep-2011	0.5	500	3	1000	0.824	center	40
17	7-Sep-2011	0.5	500	5	1000	0.824	center	40
18	7-Sep-2011	0.5	500	10	100	0.824	center	40
19	7-Sep-2011	0.5	750	3	1000	0.824	center	40
20	7-Sep-2011	0.5	750	5	1000	0.824	center	40
21	7-Sep-2011	0.5	750	10	1000	0.824	center	40
22	7-Sep-2011	0.5	1000	5	1000	0.824	center	40
23	7-Sep-2011	0.5	1500	3	1000	0.824	center	40
24	7-Sep-2011	0.5	1500	6	1000	0.824	center	40
25	8-Sep-2011	0.3	1042	10	1000	0.824	wall	0
26	8-Sep-2011	0.3	1531	10	1000	0.824	wall	0
27	8-Sep-2011	0.3	2018	10	1000	0.824	wall	0
28	8-Sep-2011	0.3	2395	10	1000	0.824	wall	0
29	8-Sep-2011	0.3	550	10	1000	0.824	wall	0
30	12-Sep-2011	0.8	798	4	1000	0.824	wall	0
31	12-Sep-2011	0.8	1044	4	1000	0.824	wall	0
32	12-Sep-2011	0.8	1239	4	1000	0.824	wall	0
33	13-Sep-2011	0.5	1044	8	10000	0.824	wall	0
34	21-Sep-2011	0.3	799	10	1000	0.364	center	0
35	21-Sep-2011	0.3	1530	15	100	0.364	center	0
36	21-Sep-2011	0.3	1530	10	1000	0.364	center	0
37	21-Sep-2011	0.5	800	8	1000	0.364	center	0
38	21-Sep-2011	0.5	1042	8	1000	0.364	center	0
39	21-Sep-2011	0.5	1529	8	1000	0.364	center	0
40	21-Sep-2011	0.8	552	5	100	0.364	center	0
41	21-Sep-2011	0.8	1045	5	1000	0.364	center	0
42	21-Sep-2011	0.8	1525	5	1000	0.364	center	0

4.2 Particle Size and Particle Number Density

Analysis of the raw camera images reveals several important trends regarding CO₂ particle size and the particle number density in the TGF test section. First, as the stagnation pressure in the tunnel is increased the rate of CO₂ sublimation is decreased. Figure 4.1 shows typical particle size and particle number density for Mach 0.3 at the lowest stagnation pressure of 500 pounds per square foot (psf). The particles produced at this condition range in size from two to six pixels. When the Mach number is held constant and stagnation pressure is increased to a mid-range value of 1042 psf, average particle size increases to between four and eight pixels as seen in Figure 4.2. This trend of increasing particle size continues through the 1531 and 2018 psf conditions and is shown in Figure 4.3 and Figure 4.4. At the maximum stagnation pressure of 2395 psf the CO₂ particles sublime at the slowest rate and retain a larger portion of their original size. Figure 4.5 shows typical particle sizes for the Mach 0.3, 2395 psf case. Average particle size at this condition ranges from eight to twelve pixels. Occasionally large particles over 12 pixels in diameter are produced at this condition and can be seen in Figure 4.5. This trend is consistent when velocity is held at Mach 0.5 or Mach 0.8 and stagnation pressure is varied.

It is important to point out that camera 1, above the light sheet, is used to display the images from the large, 0.824 inch ID, shroud tubes and particles will appear on the left side of the image, representing the inside of the tunnel. Camera 2, located below the light sheet, is used to display images from the small, 0.364 inch ID, shroud tubes and particles will appear on the right side of the image. The white line in each image is a reflection of the light sheet and represents the approximate location of the window.

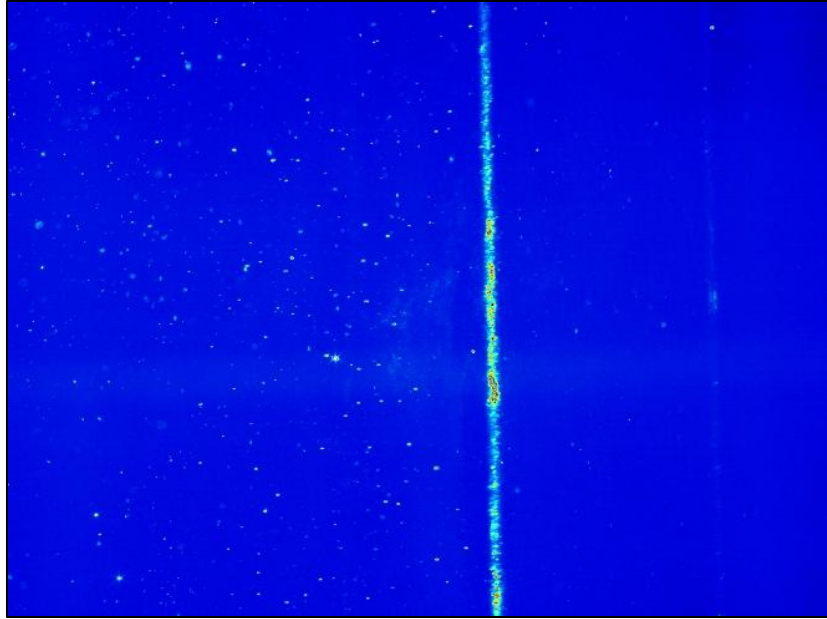


Figure 4.1: Seeding from 0.824 inch ID shroud tubes at $M = 0.3$, $P = 500$ psf.

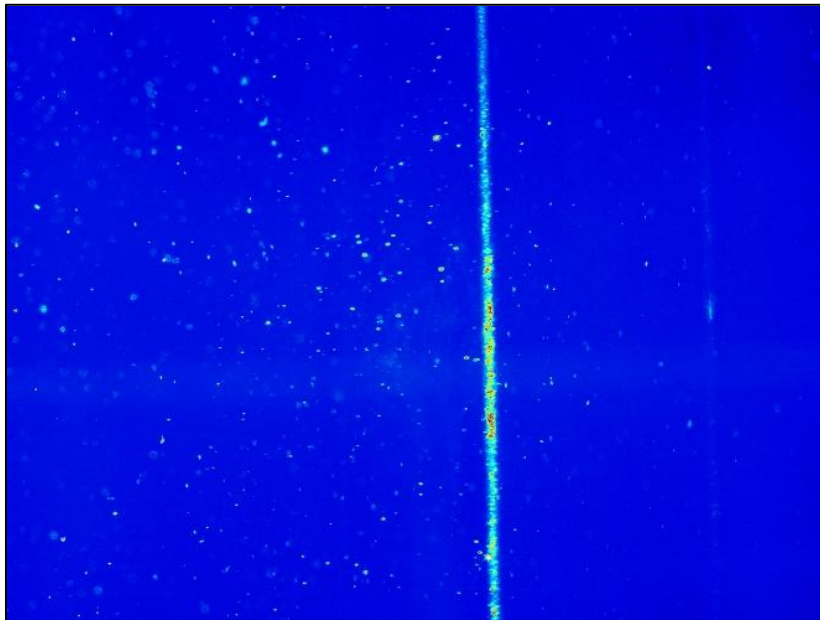


Figure 4.2: Seeding from 0.824 inch ID shroud tubes at $M = 0.3$, $P = 1042$ psf.

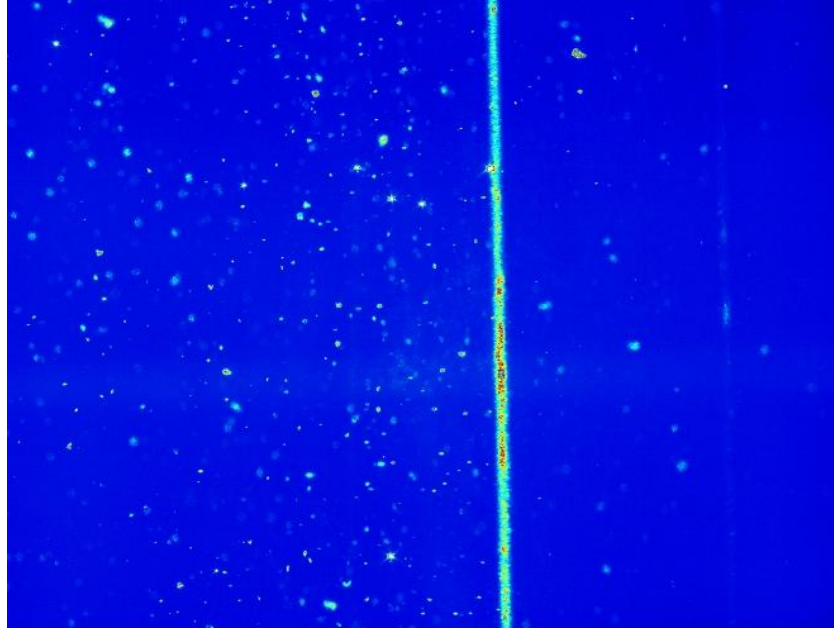


Figure 4.3: Seeding from 0.824 inch ID shroud tubes at $M = 0.3$, $P = 1531$ psf.

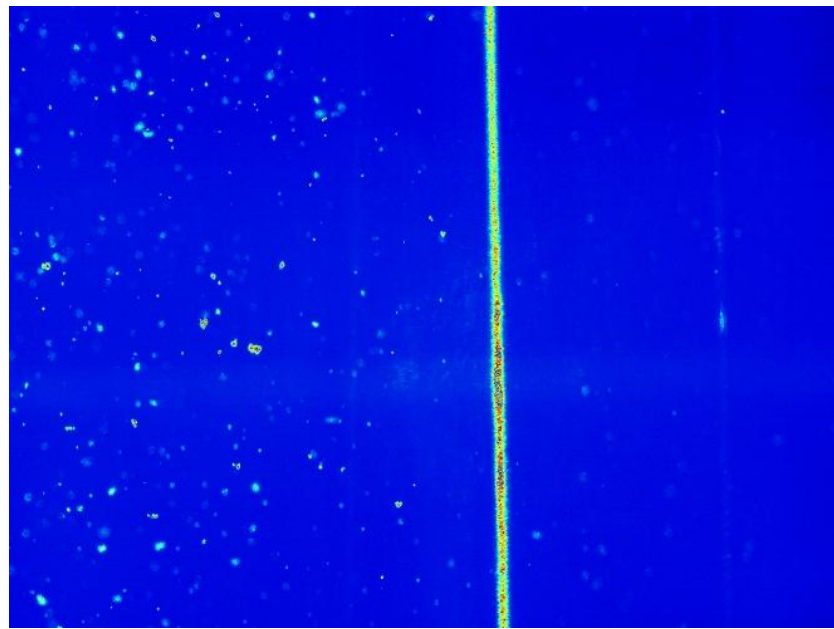


Figure 4.4: Seeding from 0.824 inch ID shroud tubes at $M = 0.3$, $P = 2018$ psf.

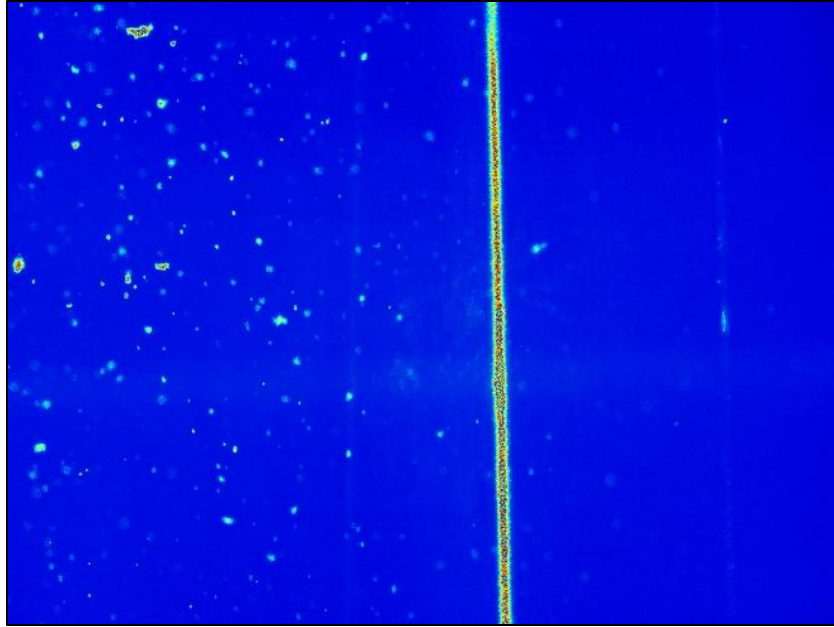


Figure 4.5: Seeding from 0.824 inch ID shroud tubes at $M = 0.3$, $P = 2395$ psf.

The second trend confirms prior research by Greene [11] and Love [7] showing that decreasing the size of the shroud tubes will decrease the size of the CO_2 particles. Figure 4.6 shows typical particle size between five and ten pixels for Mach 0.5 at 1044 psf using shroud tubes with an ID of 0.824 inches. When smaller shroud tubes with an ID of 0.364 are used, particle sizes are noticeably smaller, between two and four pixels, at equivalent tunnel conditions. Particle number density in the test section of the TGF also decreases significantly. An image of particles generated with the smaller shroud tubes at Mach 0.5 and 1042 psf is shown in Figure 4.7. The particle number density at this condition is sufficient to capture PIV data over 1000 image pairs.

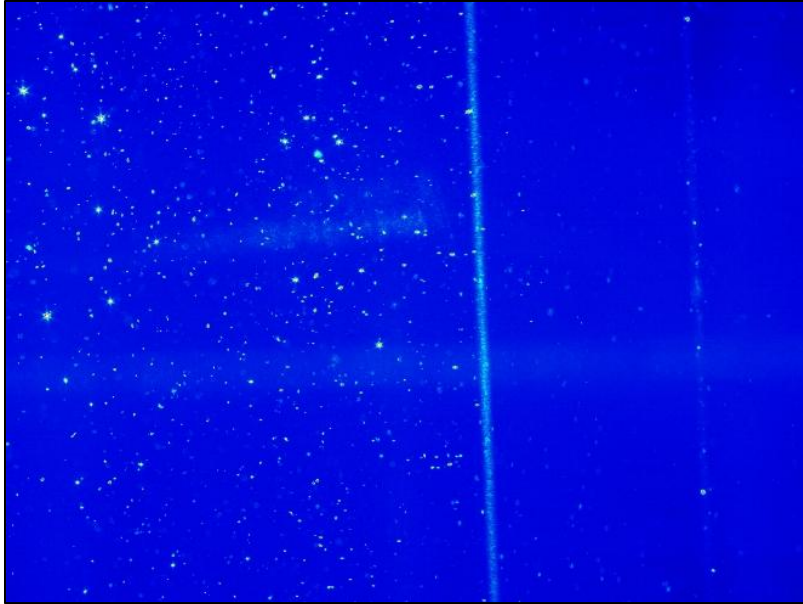


Figure 4.6: Seeding from 0.824 inch ID shroud tubes at $M = 0.5$, $P = 1044$ psf.

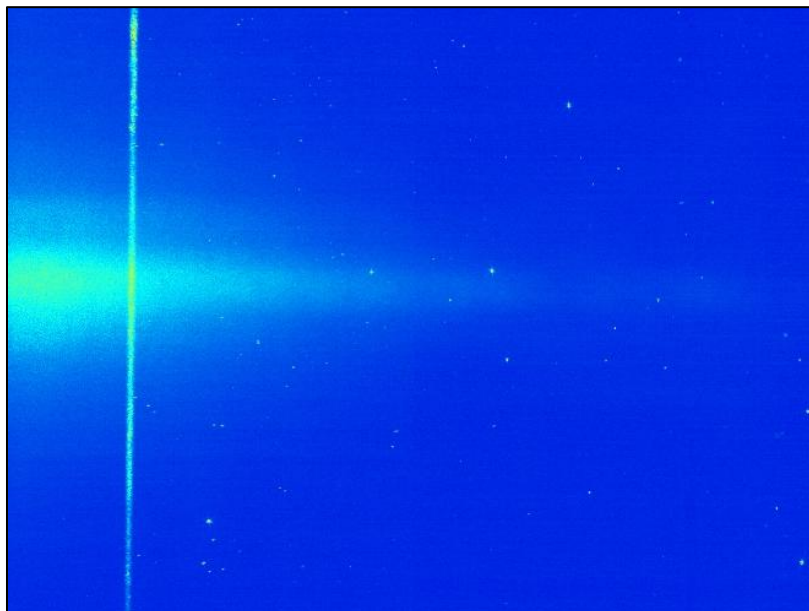


Figure 4.7: Seeding from 0.364 inch ID shroud tubes at $M = 0.5$, $P = 1042$ psf.

The final trend revealed as a result of this research is at low stagnation pressures the 0.364 inch ID shroud tubes produce small particles, a majority of which sublime prior to reaching the test section of the TGF. Figure 4.8 shows the typical particles produced at Mach 0.3 and 750 psf. Particle number density is extremely low and particles are approximately one or two pixels in diameter. Similar results were obtained at stagnation pressures below 1000 psf and flow velocities of Mach 0.5 and Mach 0.8. Above 1000 psf, the small shroud tubes are able to produce sufficient particles to capture PIV data.

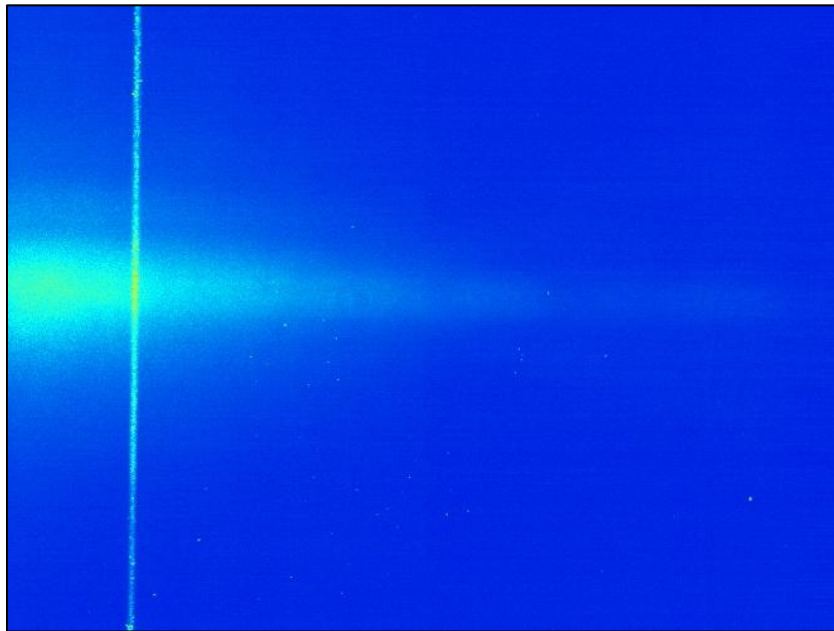


Figure 4.8: Seeding from 0.364 inch ID shroud tubes at $M = 0.3$, $P = 750$ psf.

PIV is highly dependent on particle size and particle number density to calculate flow field characteristics. Each image pair must have a sufficient amount of properly sized particles in order to produce a quality vector map of the flow. These individual

vector maps are averaged over the entire set of image pairs to produce an accurate flow field vector map. The resulting vector map of a single image pair with very low particle number density is shown below in Figure 4.9. This single vector map corresponds to an image pair (Figure 4.8) collected at Mach 0.3 and 750 psf in Experiment 34. Particle number density was extremely low in this case and did not produce a valid flow field vector map.

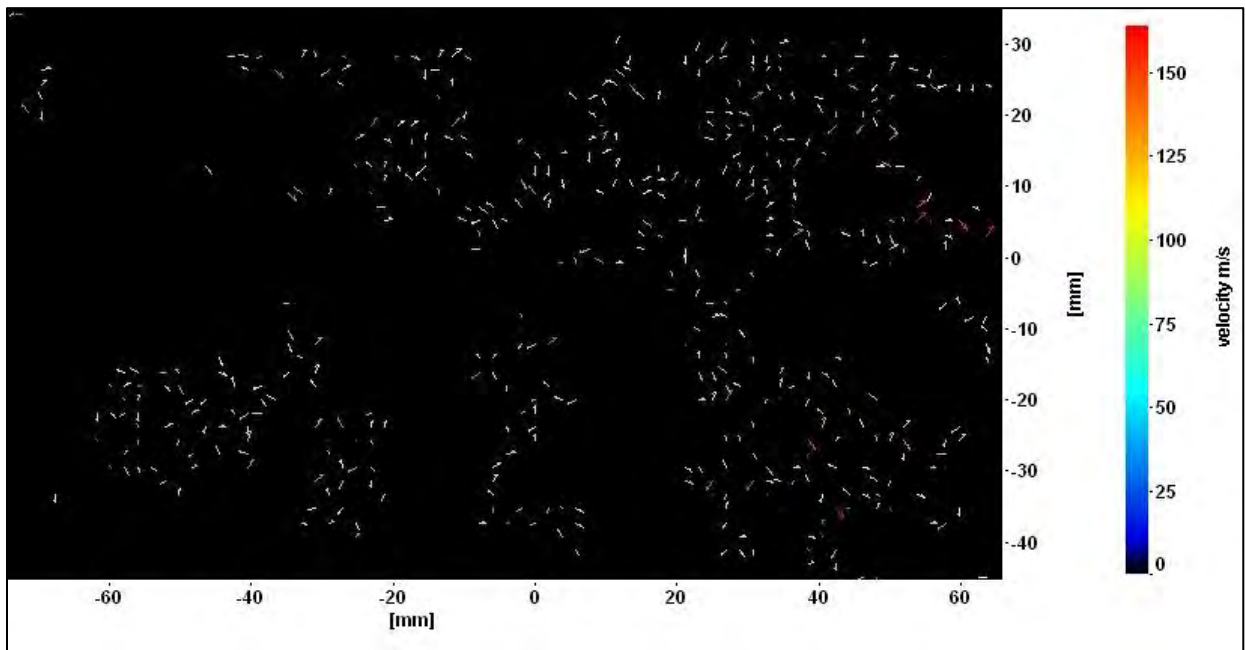


Figure 4.9: Vector map of image pair with low particle number density.

Image pairs with a high particle number density provide sufficient data to accurately calculate the overall average flow field vector map. Experiment 31 was conducted at Mach 0.8 and 1044 psf. Figure 4.10 shows the high number of particles present in a typical image pair collected at this tunnel condition. The corresponding vector map to this image is shown in Figure 4.11 and shows a significant increase in the

amount of valid vectors calculated. The condensation cloud visible in Figure 4.10 may be a result of moisture condensation where the CO₂ has locally cooled the flow field, though this is just a hypothesis.

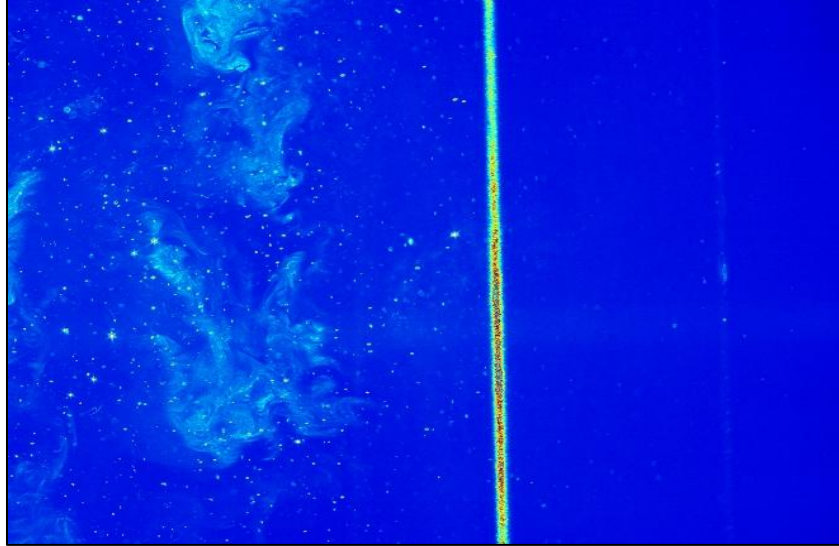


Figure 4.10: Seeding from 0.824 inch ID shroud tubes at $M = 0.8$, $P = 1044$ psf.

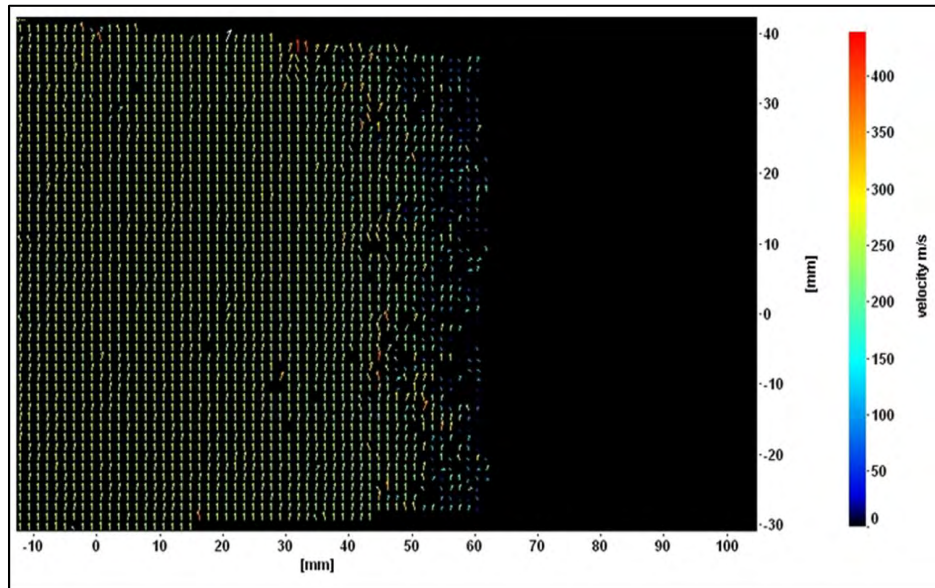


Figure 4.11: Vector map of a single image pair captured at $M = 0.8$, $P = 1044$ psf.

The final step performed by the PIV analysis software is a summing and averaging of the individual vector maps resulting in a single overall average velocity vector map of the flow field. This final vector map provides the means to further analyze the data by producing scalar plots of V_x , V_y , v_x' , v_y' and $v_x'v_y'$ for the entire image. Text files of this data are then exported to another software program for analysis. Boundary layer profiles were calculated by plotting V_x versus distance from the wall for each experiment. Calculations of turbulence in the boundary layer were also performed for several experiments using v_x' , v_y' and $v_x'v_y'$.

4.3 Boundary Layer Calculations

4.3.1 Mach 0.3

Boundary layer profiles were calculated by averaging the freestream velocities along ten separate rows of the time averaged flow field vector map. Selection of the rows must be done carefully as to avoid areas in the vector map where light reflections bias the data. The red box in Figure 4.12 shows an area of a final vector map that contains data affected by a reflection. Velocity profile data for the Mach 0.3, 550 psf condition, using 0.824 inch ID shroud tubes, was collected from horizontal rows above and below the boxed area to perform boundary layer calculations. In this image the tunnel wall is located at approximately 62 mm on the X-axis and the flow is moving vertically from the bottom to the top. Tunnel instrumentation indicated a freestream velocity of 105 m/s. PIV measurements resulted in an average freestream velocity of 103.4 m/s yielding an error of less than two percent. Figure 4.13 shows a boundary layer thickness of approximately 59 mm when measured at 99 percent of the freestream velocity. The

initial gap between the wall and boundary layer is due to the ambiguity in the wall location. In order to align with standard convention, the boundary layer profile data has been rotated 90 degrees clockwise from the vector map so the flow direction is from left to right while the distance from the wall is indicated on the Y-axis.

Boundary layer data is also typically plotted according to the “law of the wall” which states the average velocity of a turbulent flow at a certain point is proportional to the logarithm of the distance from that point to the wall. Clauser plots are one method used to graphically represent boundary layer data. Clauser plots of the data from this research are presented in Appendix B.

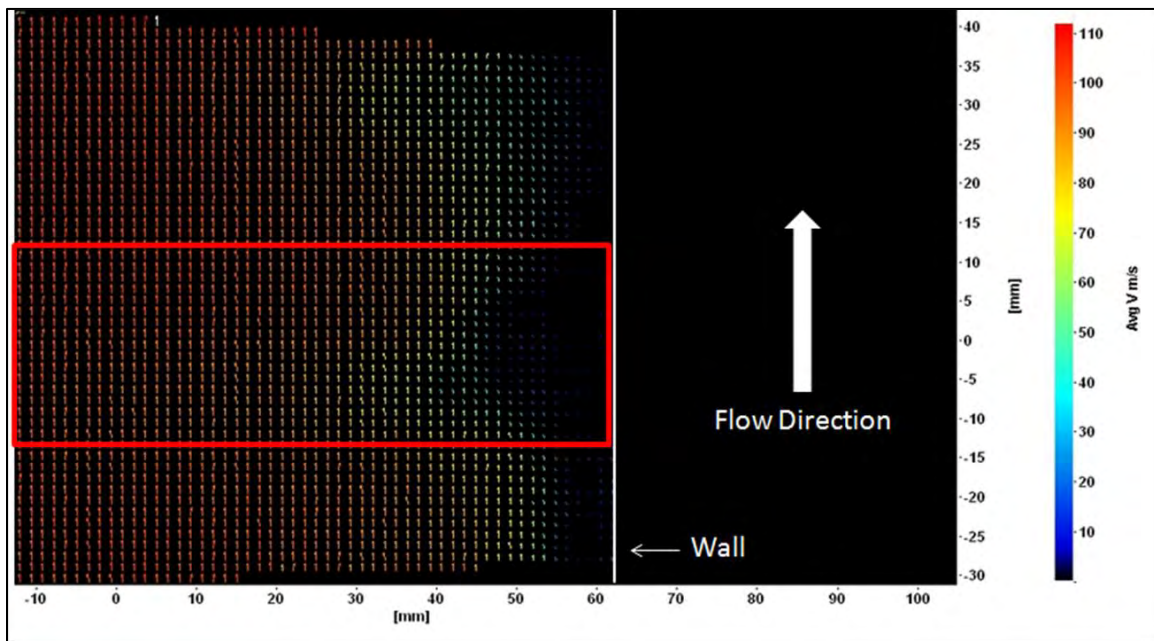


Figure 4.12: Flow field vector map for 0.824 inch ID shroud tubes at $M = 0.3$, $P = 550$ psf with red box indicating area affected by laser light reflections.

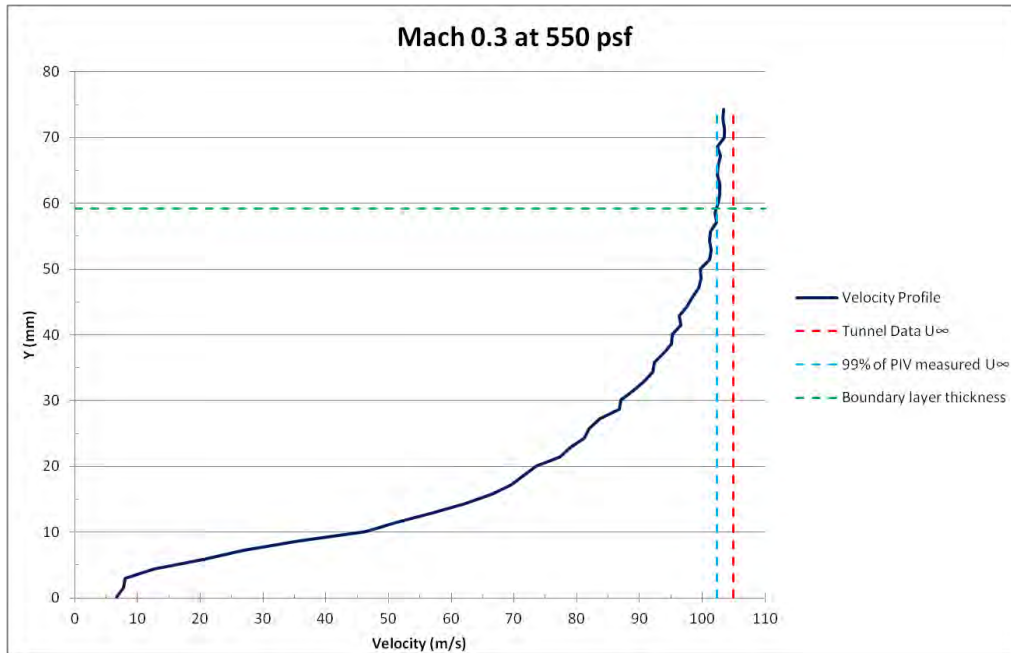


Figure 4.13: Velocity profile for 0.824 inch ID shroud tubes at $M = 0.3$, $P = 550$ psf.

In Experiment 25, tunnel conditions were set to Mach 0.3 and 1042 psf. The large shroud tubes were used in this case and provided excellent particle size and particle number density. The PIV vector map resulted in an average freestream velocity of 103.1 m/s while tunnel data indicated 104.6 m/s. Boundary layer thickness was calculated to be approximately 61 mm as shown in Figure 4.14.

For Experiment 26, stagnation pressure was increased to 1531 psf while velocity was held to Mach 0.3. The PIV calculation of freestream velocity, 100 m/s, was 3.66% lower than the velocity of 103.8 m/s measured by tunnel instrumentation. Figure 4.15 shows an estimate for boundary layer thickness of 67 mm.

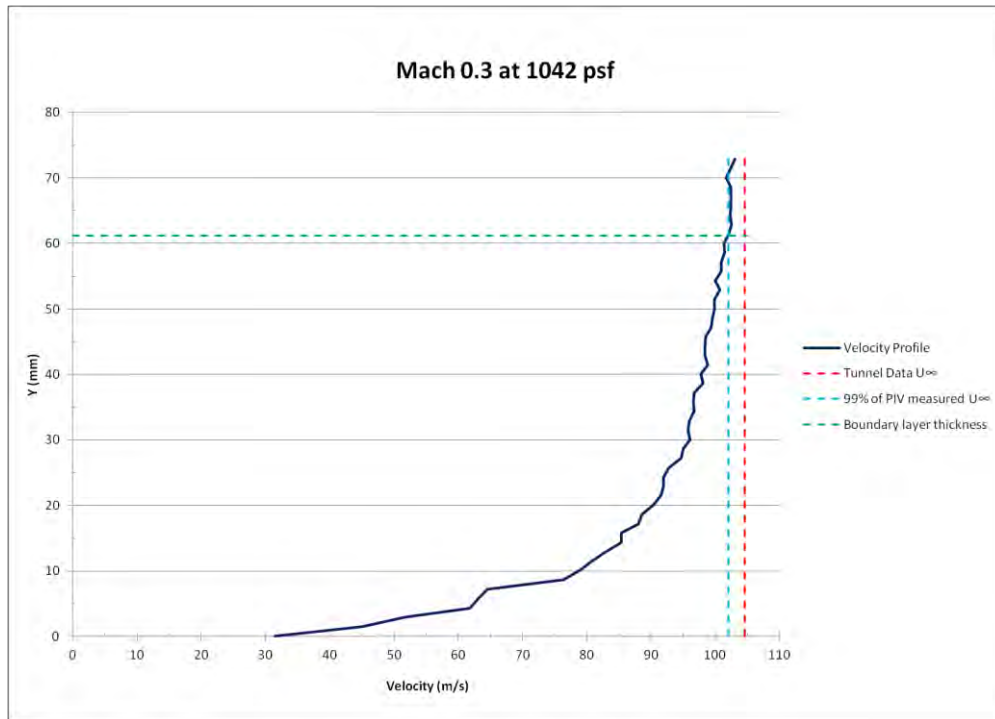


Figure 4.14: Velocity profile for 0.824 inch ID shroud tubes at $M = 0.3$, $P = 1042$ psf.

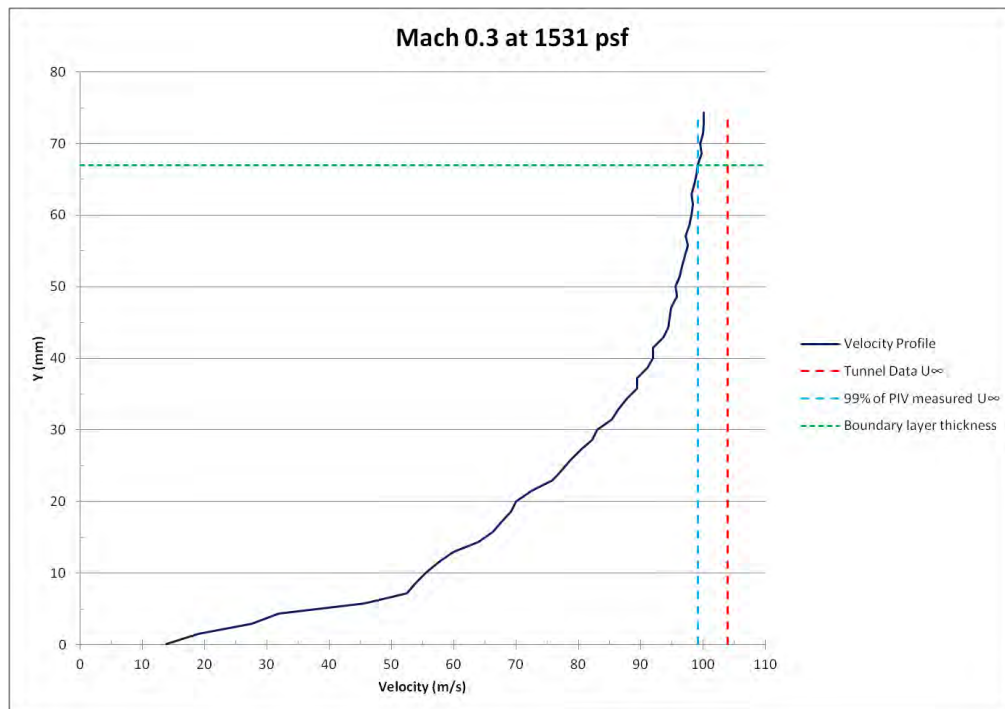


Figure 4.15: Velocity profile for 0.824 inch ID shroud tubes at $M = 0.3$, $P = 1531$ psf.

In Experiments 27 and 28, stagnation pressure was increased to 2018 psf and 2395 psf respectively. In both cases it appears particle size increased to the point where reliable freestream velocities could not be captured by the PIV system. Errors between PIV measurements and actual freestream velocities were over 15% at 2018 psf and 33% at 2395 psf. Boundary layer thickness for Experiment 27 was approximately 66 mm. An estimate for boundary layer thickness cannot be accurately calculated for the Experiment 28. Figure 4.16 and 4.17 are shown to demonstrate how improperly sized particles negatively affect PIV measurements.

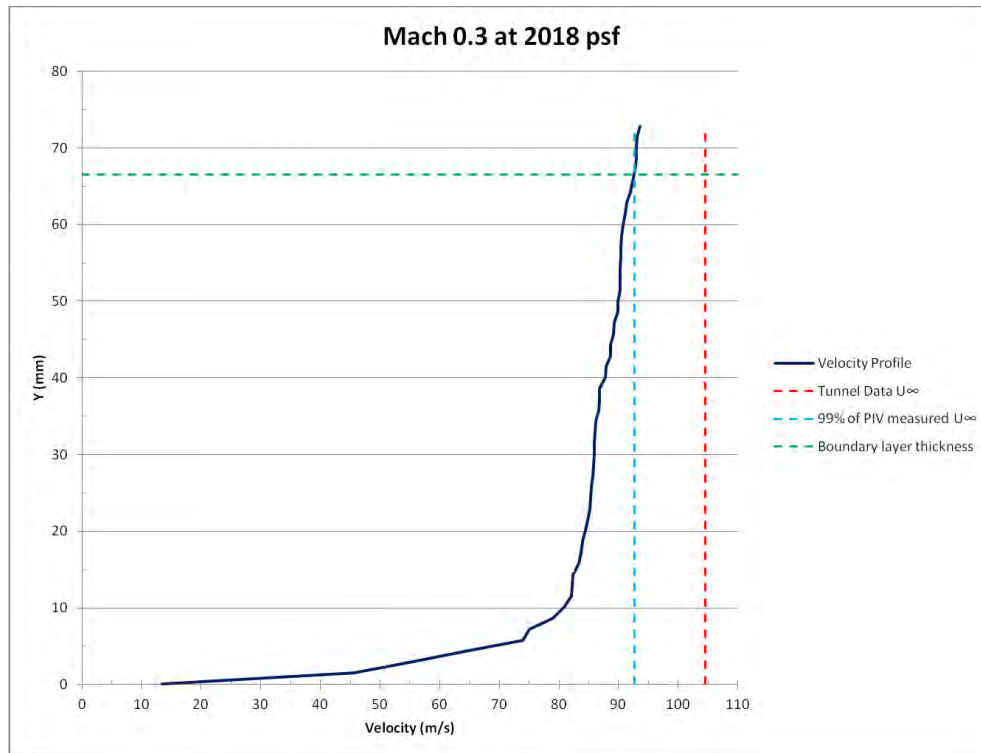


Figure 4.16: Velocity profile for 0.824 inch ID shroud tubes at $M = 0.3$, $P = 2018$ psf.

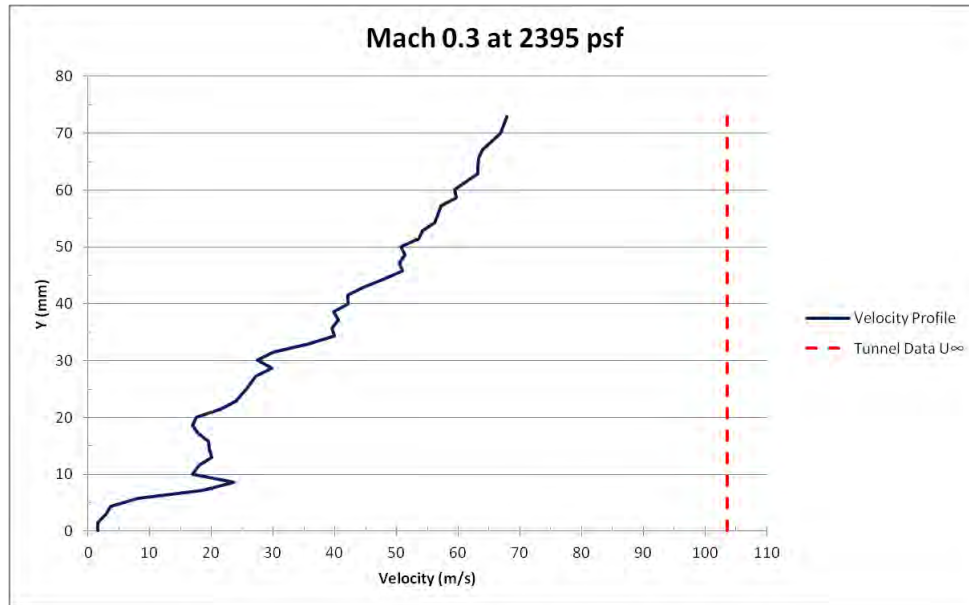


Figure 4.17: Velocity profile for 0.824 inch ID shroud tubes at $M = 0.3$, $P = 2395$ psf.

The second set of experiments performed at Mach 0.3 used the smaller shroud tubes with an ID of 0.364 inches. Experiments were conducted at 750 psf and 1000 psf but particle number density in the test section was extremely low in both cases making the collection of PIV data impractical. The stagnation pressure was then increased to approximately 1530 psf. This reduced the sublimation rate of the CO_2 resulting in a sufficient amount of particles in the test section to resume PIV data collection. Freestream velocity according to the tunnel instruments was 103.7 m/s, while PIV measurements produced an average velocity of 102.4 m/s, a difference of less than 2%. The boundary layer thickness is calculated to be approximately 64 mm as shown in Figure 4.18. A comparison of the results obtained using different sizes of shroud tubes is shown in Figure 4.19. Beyond 35 mm from the wall, the two velocity measurements are reasonably consistent. Below 35 mm, however, the two profiles are inconsistent due to differences in the particles sizes and their ability to follow the flow dynamics.

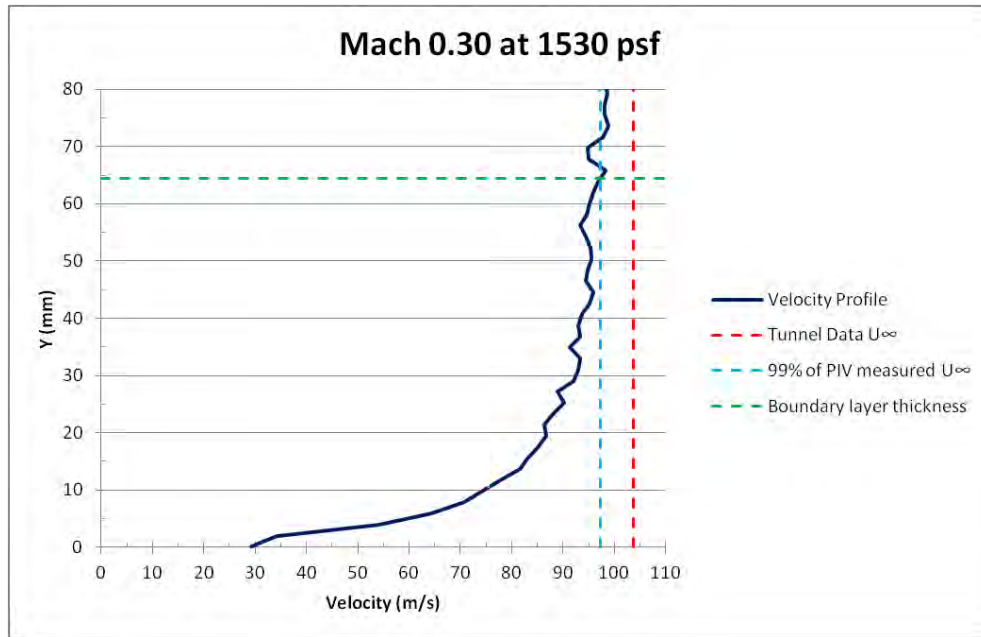


Figure 4.18: Velocity profile for 0.364 inch ID shroud tubes at $M = 0.3$, $P = 1530$ psf.

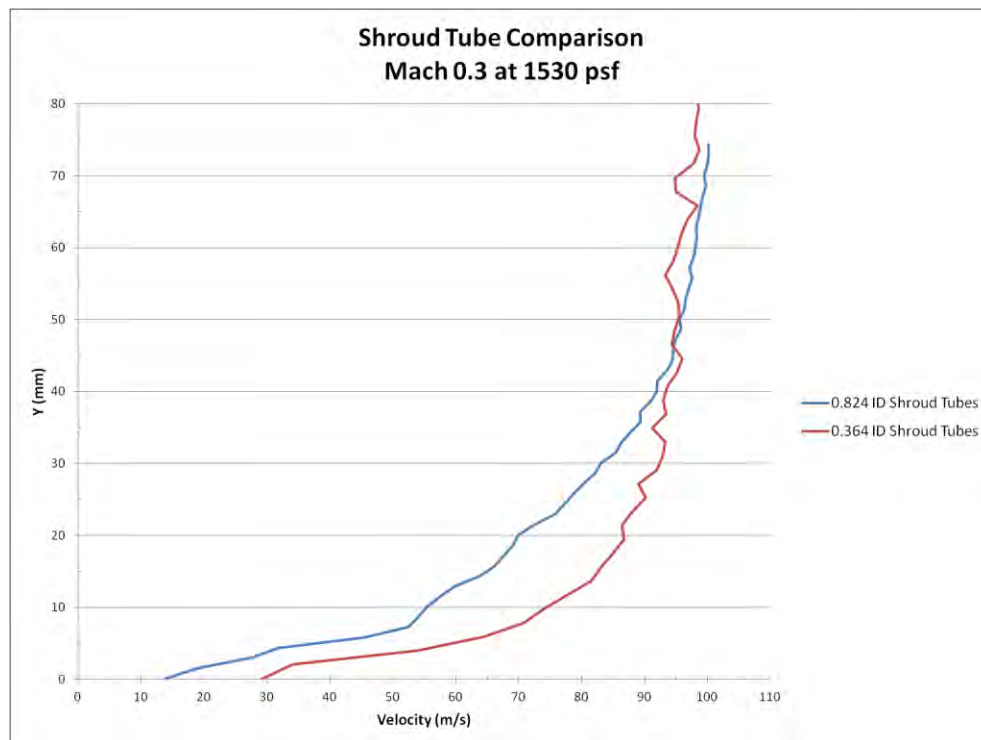


Figure 4.19: Boundary layer comparison using 0.824 inch ID and 0.364 inch ID shroud tubes at $M = 0.3$, $P = 1530$ psf.

The size of the particles produced by the large shroud tubes are significantly larger than the particles generated by the small tubes and may account for this difference.

4.3.2 *Mach 0.5*

Particle number density was sufficient for PIV data collection in all experiments conducted at Mach 0.5. In Experiment 33, a total of 10000 image pairs were collected at the Mach 0.5, 1044 psf condition using the larger shroud tubes. This data set provides a larger statistical sample for improved boundary layer thickness calculations and turbulence data analysis which is discussed in Section 4.4. Figure 4.20 shows the results for the Mach 0.5 at 1044 psf case using the large shroud tubes. As expected, the velocity profile curve for this test case is much smoother than for the other cases. Freestream velocity calculations using the PIV system were within 1 m/s of the data provided by tunnel instrumentation. The boundary layer thickness is estimated to be approximately 64 mm.

A second experiment was conducted at the same wind tunnel conditions with the small shroud tubes. Results of this test are shown in Figure 4.21 and show a boundary layer thickness of approximately 62 mm. Comparison of the two profiles in Figure 4.22 shows a similar trend in the boundary layer growth. Small changes in the wind tunnel settings or stagnation temperature may account for the different freestream velocity values.

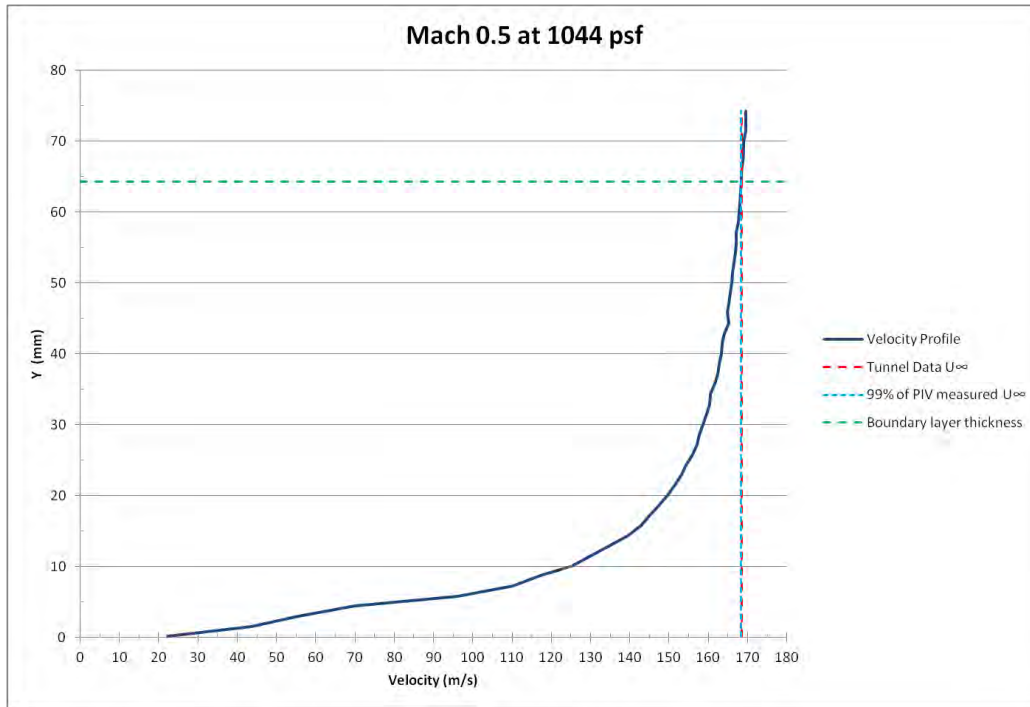


Figure 4.20: Velocity profile for 0.824 inch ID shroud tubes at $M = 0.5$, $P = 1044$ psf.

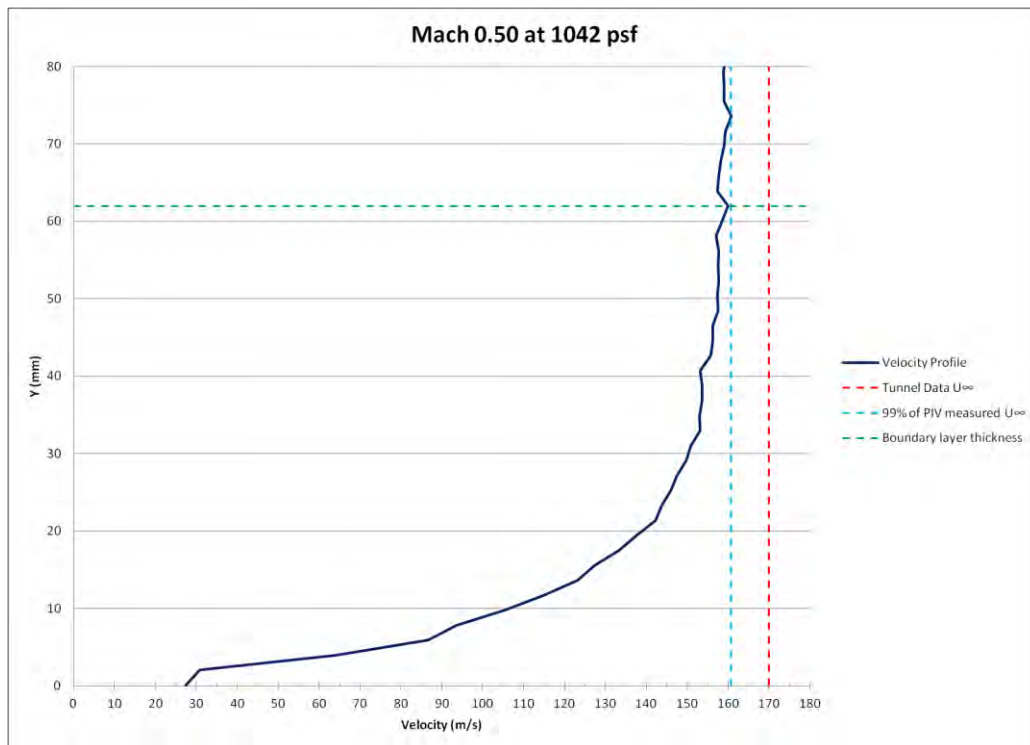


Figure 4.21: Velocity profile for 0.364 inch ID shroud tubes at $M = 0.5$, $P = 1042$ psf.

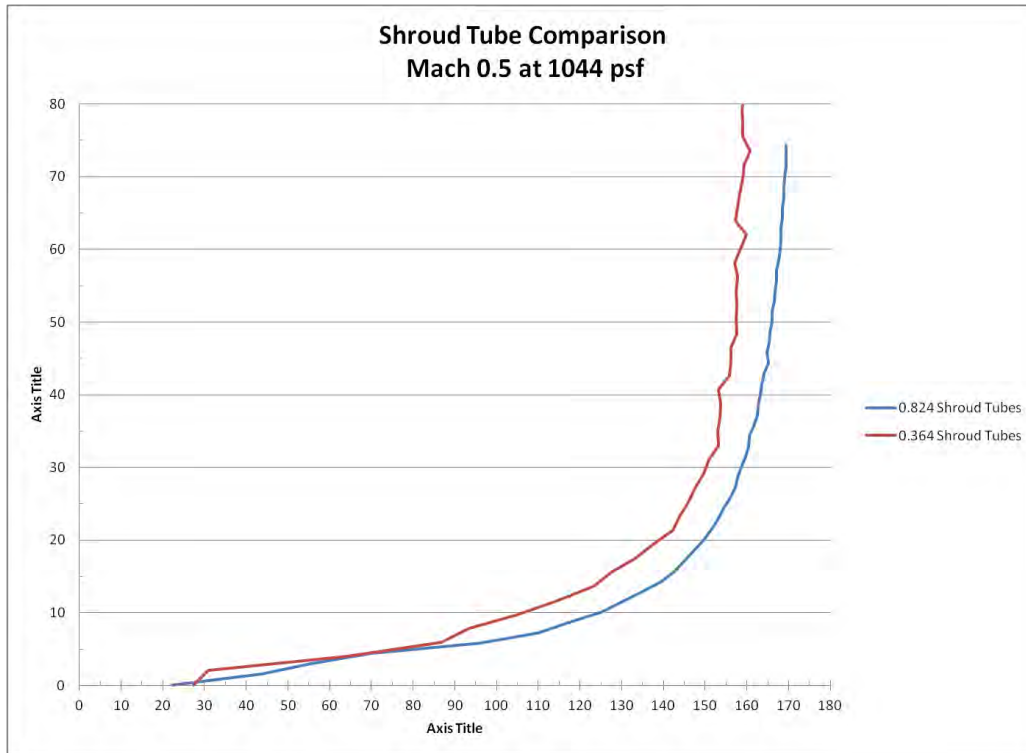


Figure 4.22: Boundary layer comparison using 0.824 inch ID and 0.364 inch ID shroud tubes at $M = 0.5$, $P = 1044$ psf.

The final Mach 0.5 experiment was conducted at 1530 psf with the small shroud tubes. Wind tunnel data reveals a freestream velocity of 169.6 m/s compared to a PIV measurement of 168.4 m/s. Based on the mean velocity measured using the wind tunnel instrumentation, the boundary layer thickness for this case worked out to approximately 94 mm as seen in Figure 4.23.

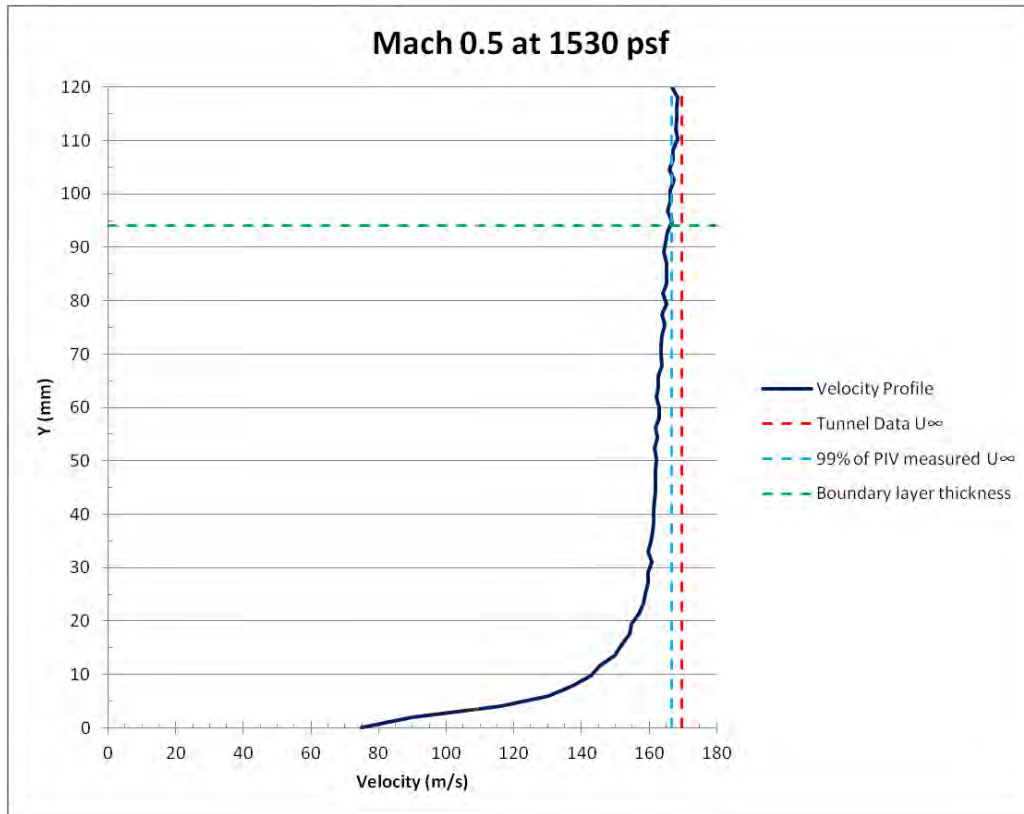


Figure 4.23: Velocity profile for 0.364 inch ID shroud tubes at $M = 0.5$, $P = 1530$ psf.

4.3.3 Mach 0.8

Particle number density was very good for all Mach 0.8 experiments. Three sets of data were collected using the large shroud tubes at different stagnation pressures, 798 psf, 1044 psf, and 1239 psf. Trial runs with the small shroud tubes at low pressures revealed a lack of CO_2 at pressures stagnation pressures of 500 and 750 psf. As the stagnation pressure was raised to 1000 psf the particle number density increased to acceptable levels for data collection.

Figure 4.24 through Figure 4.26 show velocity profiles for the large shroud tube experiments at Mach 0.8 and 798 psf, 1044 psf, and 1239 psf in order. In all three cases

boundary layer thickness is estimated to be 59 mm. Errors between freestream velocities recorded by tunnel instrumentation and calculated from PIV data are minimized at low pressures where particle size is small. At 798 psf this error is 1.7%. As stagnation pressure is increased, particle size increases resulting in an increased error between freestream velocity measurements. This error is 2.3% at 1044 psf and 4.3% at 1239 psf.

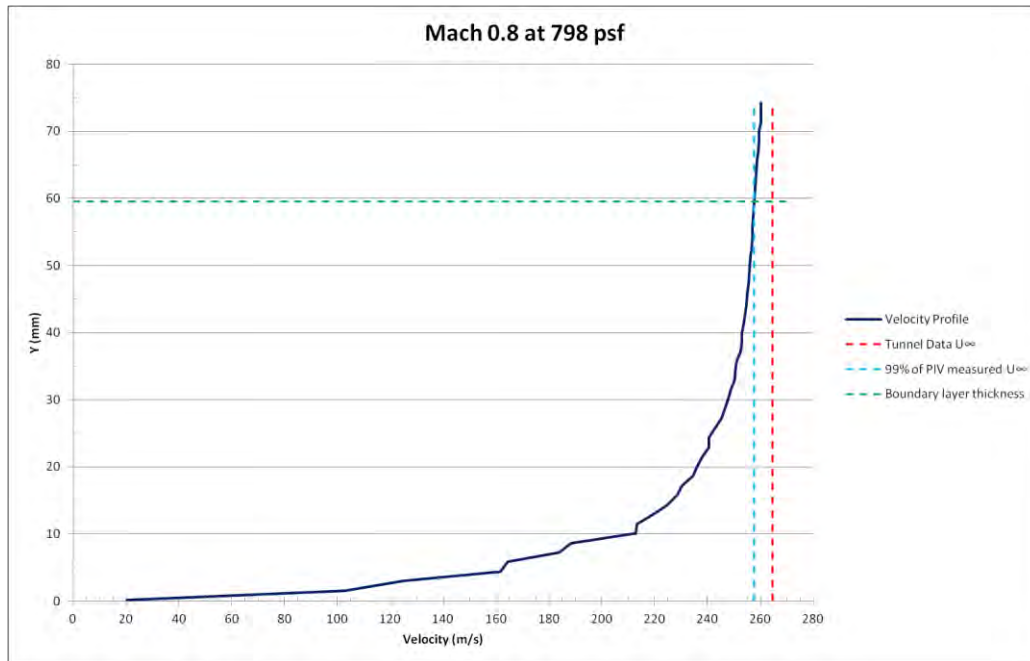


Figure 4.24: Velocity profile for 0.824 inch ID shroud tubes at $M = 0.8$, $P = 798$ psf.

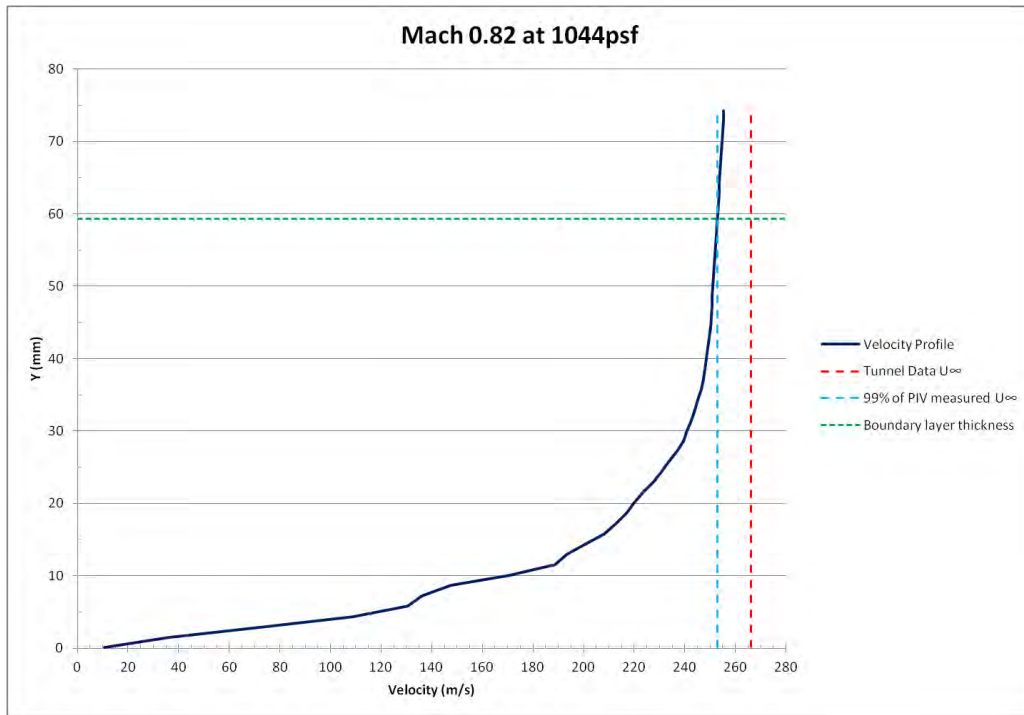


Figure 4.25: Velocity profile for 0.824 inch ID shroud tubes at $M = 0.82$, $P = 1044$ psf.

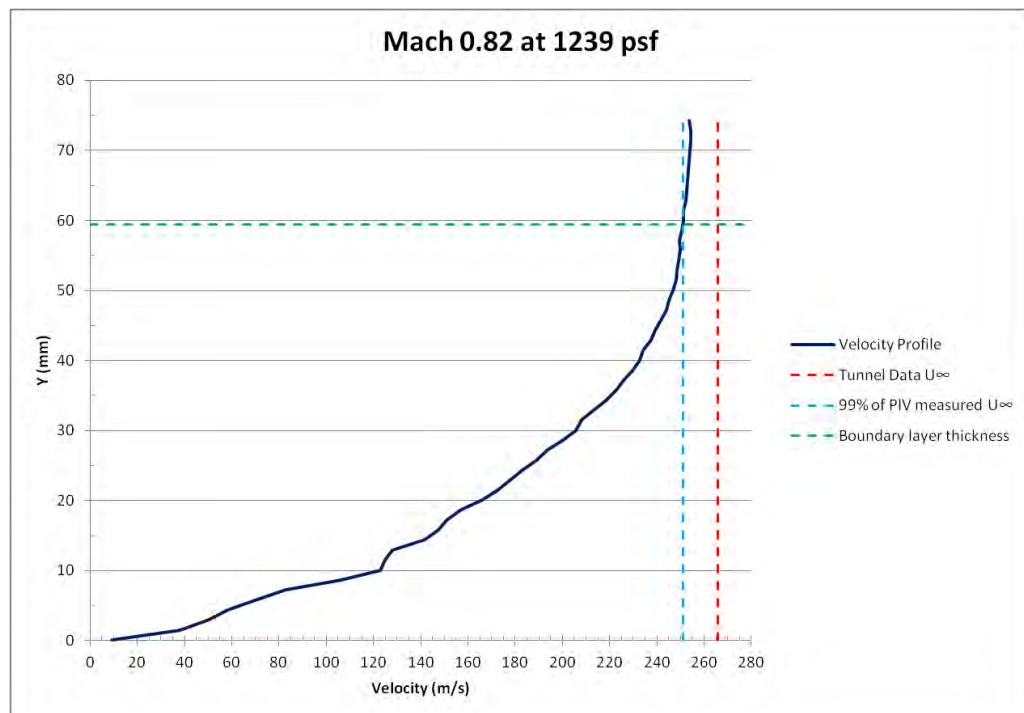


Figure 4.26: Velocity profile for 0.824 inch ID shroud tubes at $M = 0.82$, $P = 1239$ psf.

Two experiments were conducted at approximately Mach 0.8 with the small shroud tubes. Tunnel conditions for Experiment 41 were Mach 0.84, 272 m/s, and 1045 psf. The average PIV measurement of freestream velocity was 265 m/s and the boundary layer thickness was estimated to be 68 mm. The velocity profile for Experiment 41 is shown in Figure 4.27. Experiment 42 was conducted at Mach 0.79, or 263 m/s, and 1525 psf. The average freestream velocity measured by PIV was 266.9 m/s. In this test the boundary layer thickness was measured to be 71 mm as seen in Figure 4.28.

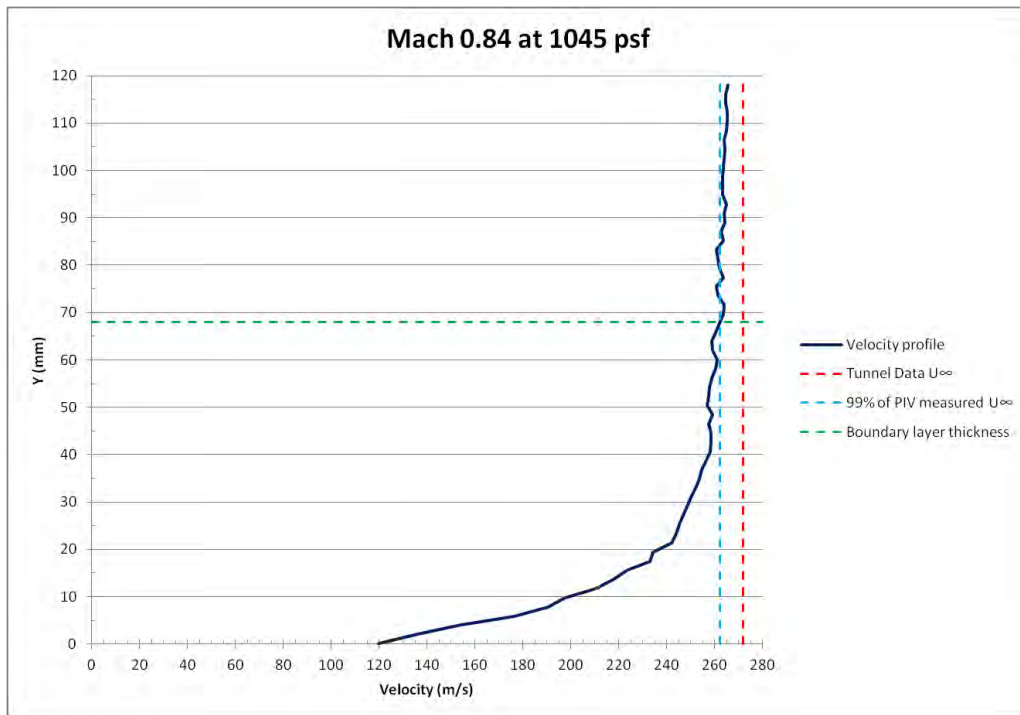


Figure 4.27: Velocity profile for 0.364 inch ID shroud tubes at $M = 0.84$, $P = 1045$ psf.

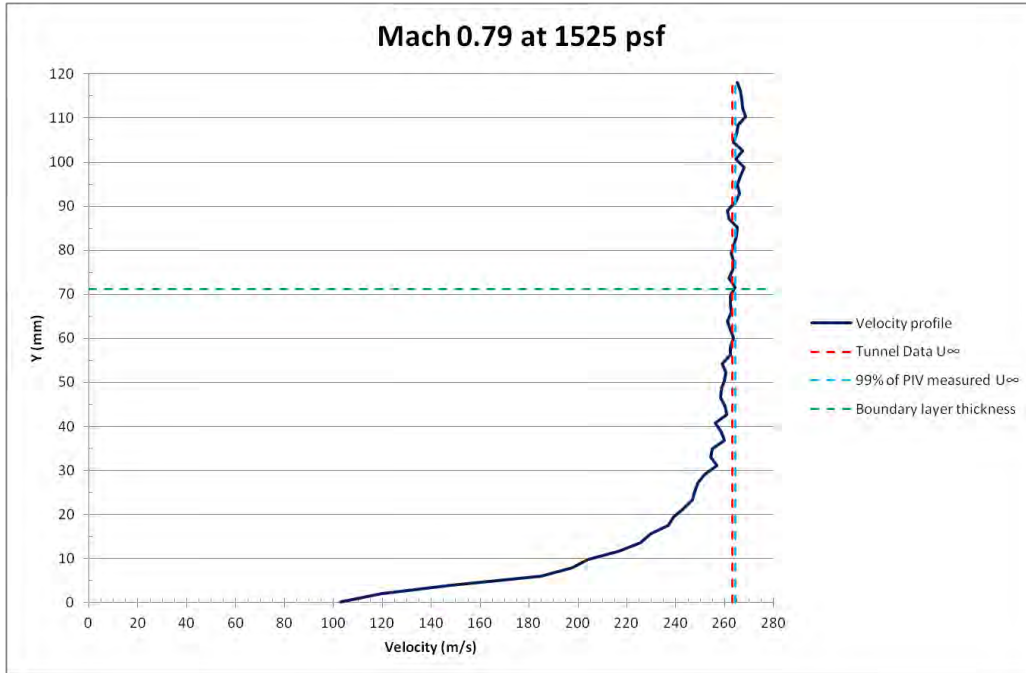


Figure 4.28: Velocity profile for 0.364 inch ID shroud tubes at $M = 0.79$, $P = 1525$ psf.

4.3.4 Expected Boundary Layers

In this section, boundary layer thickness measurements obtained through PIV are compared to expected values. The expected values for boundary layer thickness are calculated using Equation (2.7), which was developed empirically for flow over flat plates at zero incidence. Solving this equation for δ_{99} will yield a boundary layer thickness at the point where velocity equals 99% of the freestream velocity, U_{∞} . In the TGF, the straight section wall extends from a convergent nozzle, and so there is some ambiguity in the proper characteristic distance, x , to use in Equation (2.7). In order to use this comparison method, a characteristic distance is needed. The boundary layer thickness measured in Experiment 33 is based on an average of 10000 image pairs and therefore provides the most statistically accurate measurement of this value. PIV analysis

of Experiment 33 revealed a boundary layer thickness of 64 mm. This value is set equal to δ_{99} , and Equation (2.7) is solved for the characteristic distance, x , resulting in a value of 3.795 m, which seems reasonable given the complex geometry of the TGF. Equation (4.1) is then solved for the other experiments to calculate an expected boundary layer thickness.

$$\delta_{99} = \frac{(0.37)(3.795 \text{ m})}{Re^{(\frac{1}{5})}} \quad (4.1)$$

where

$$Re = \text{Reynolds number based on tunnel condition}$$

Results of these calculations and comparison to the measured boundary layer thickness are shown in Table 4.2. In most cases the difference, $\Delta\delta_{99}$, between the calculated and measured value is less than 10 mm.

A second way of analyzing the boundary layer thickness is to calculate a value for δ at the location where velocity in the boundary layer reaches 90% of the freestream. One motivation for using the 90% threshold is that it is difficult to determine the 99% location with a high degree of confidence. By comparison, the 90% location is reasonably clear and allows for a simple comparison of boundary layer thickness for different tunnel operating conditions. As discussed in Chapter 2, Klebanoff's research revealed that the δ_{90} value for turbulent boundary layers is approximately half of the δ_{99} measurement. Calculated and measured values for the 90% boundary layer thickness are also compared in Table 4.2. While measured values generally fall below those calculated, they do follow a noticeable trend as seen in Figure 4.29 below.

A comparison between selected boundary layer profiles and the $1/7^{\text{th}}$ power law, Equation (2.8), is presented in Appendix C. Momentum thicknesses for the power law curves were calculated using Equation (2.10).

Table 4.2: Comparison of calculated and measured boundary layer thickness.

Experiment Number	Mach Number	Static Pressure (lb/ft ²)	Shroud Tube Diameter (in)	Calculated δ_{99} (mm)	Measured δ_{99} (mm)	$\Delta \delta_{99}$ (mm)	Calculated δ_{90} (mm)	Measured δ_{90} (mm)	$\Delta \delta_{90}$ (mm)
25	0.3	1042	0.824	69.9	61.2	-8.7	34.95	25.625	-9.325
26	0.3	1531	0.824	65	67	2	32.5	37.86	5.36
27	0.3	2018	0.824	61.6	66.5	4.9	30.8	19.463	-11.337
29	0.3	550	0.824	79.4	59.2	-20.2	39.7	36.492	-3.208
30	0.8	798	0.824	63.6	59.5	-4.1	31.8	18.57	-13.23
31	0.8	1044	0.824	60.3	59.3	-1	30.15	23.92	-6.23
32	0.8	1239	0.824	58.5	59.4	0.9	29.25	38.04	8.79
33 *	0.5	1044	0.824	64	64	0	32	22.834	-9.166
36	0.3	1530	0.364	65	64.5	-0.5	32.5	23.609	-8.891
38	0.5	1042	0.364	64.5	62	-2.5	32.25	25.5	-6.75
39	0.5	1529	0.364	59.7	94	34.3	29.85	15.44	-14.41
41	0.8	1045	0.364	60.5	68	7.5	30.25	20.512	-9.738
42	0.8	1525	0.364	56.3	71.2	14.9	28.15	19.938	-8.212

* This case was used to estimate the characteristic length X.

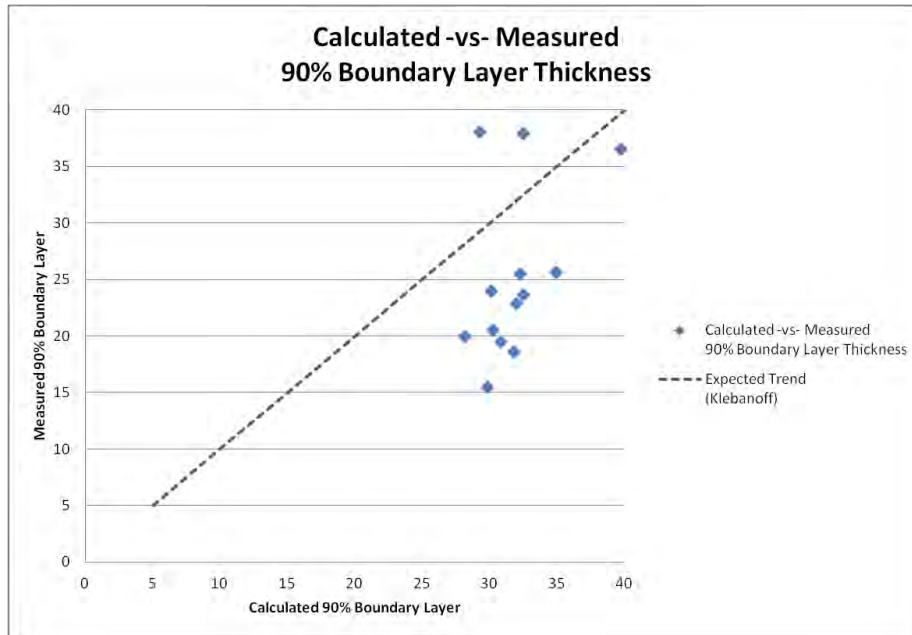


Figure 4.29: Calculated versus measured 90% boundary layer thickness.

4.4 Planar Velocity Maps and Turbulence Data

Ten thousand image pairs were captured in Experiment 33 to provide a large statistical sample to conduct PIV analysis of the turbulence in the boundary layer. The flow field vector map for this experiment is shown in Figure 4.30. Each vector in the final map is calculated by summing and averaging valid vectors calculated from individual image pairs. To determine the statistical accuracy of the final flow field vector map it is important to know how many individual valid vectors were used. Figure 4.31 shows a scalar plot of the number of valid vectors used to calculate the vector map at each location. At most locations, over 5000 vectors were used to calculate the flow field vector map. Closer to the wall, the number of valid vectors decreases to between 2000 and 4000 per location.

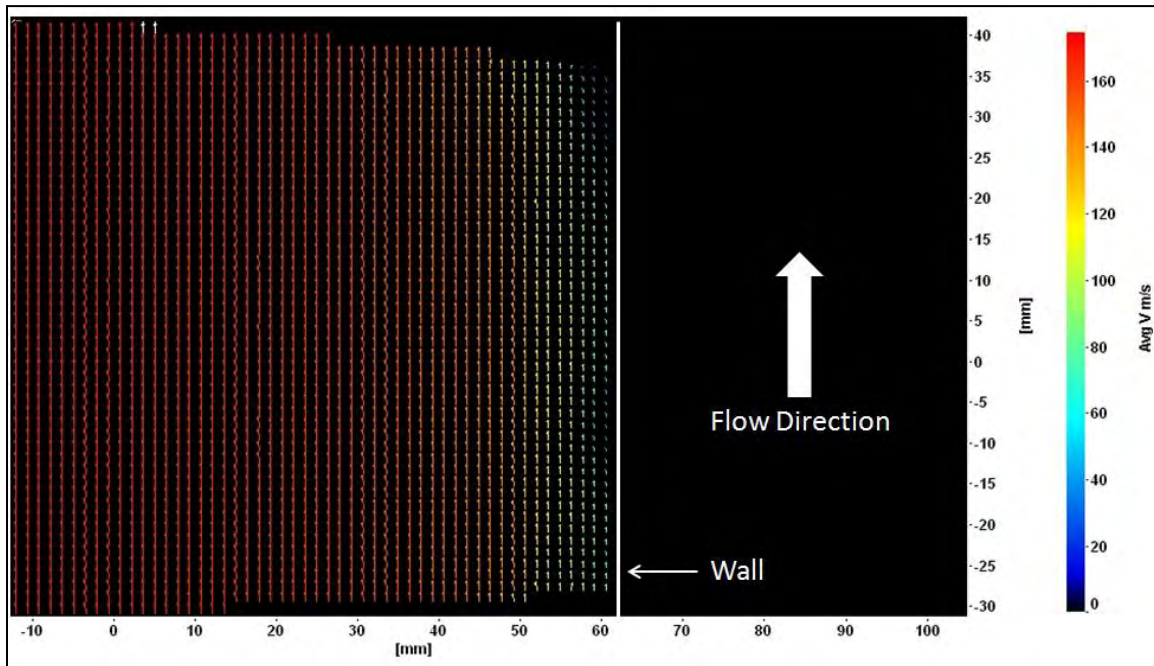


Figure 4.30: Flow field vector map for Experiment 33, $M = 0.5$, $P = 1044$ psf.

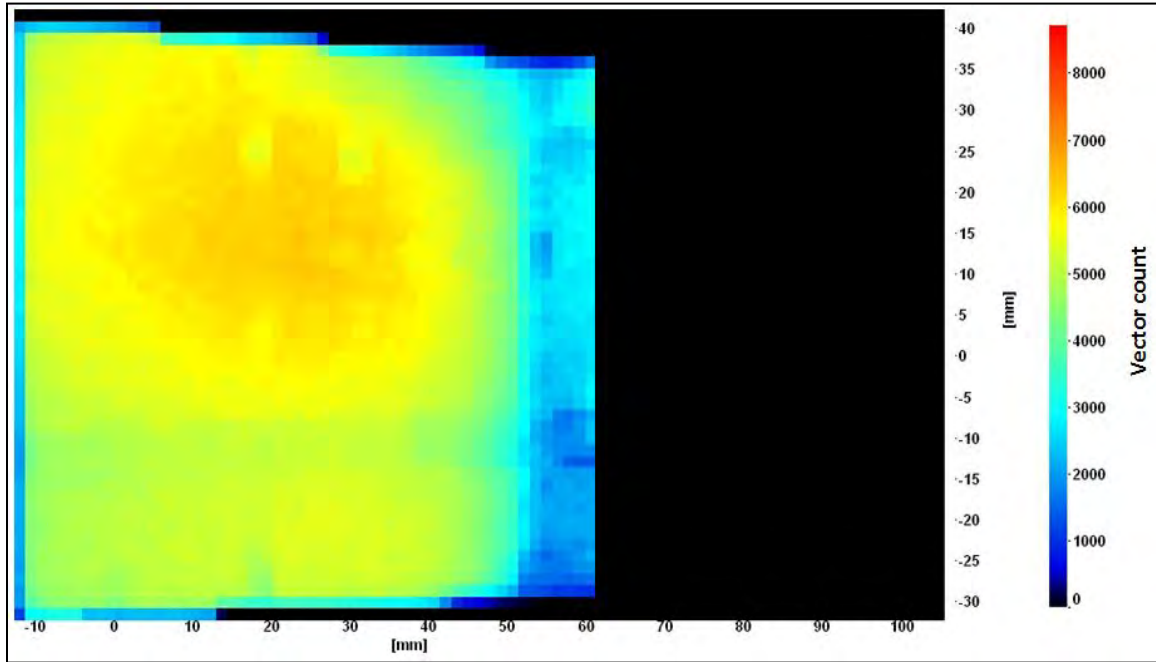


Figure 4.31: Valid vector count for Experiment 33, $M = 0.5$, $P = 1044$ psf.

The LaVision software is also capable of producing scalar plots of the streamwise velocity (V_x), perpendicular velocity (V_y), RMS fluctuations of streamwise (V_x') and perpendicular (V_y') velocity, and the Reynolds stress ($V_x'V_y'$). The data from these plots is needed to study the turbulence characteristics of the boundary layer. The scalar plots of these variables are shown in Figures 4.32, 4.33, 4.34, 4.35, and 4.36. Streamwise velocity shows the expected trend of being lowest at the wall and growing quickly to match the freestream velocity. The perpendicular velocity component remains low throughout the entire test region. Initially, all data was processed using the approach documented in Section 3.3.1 of this document.

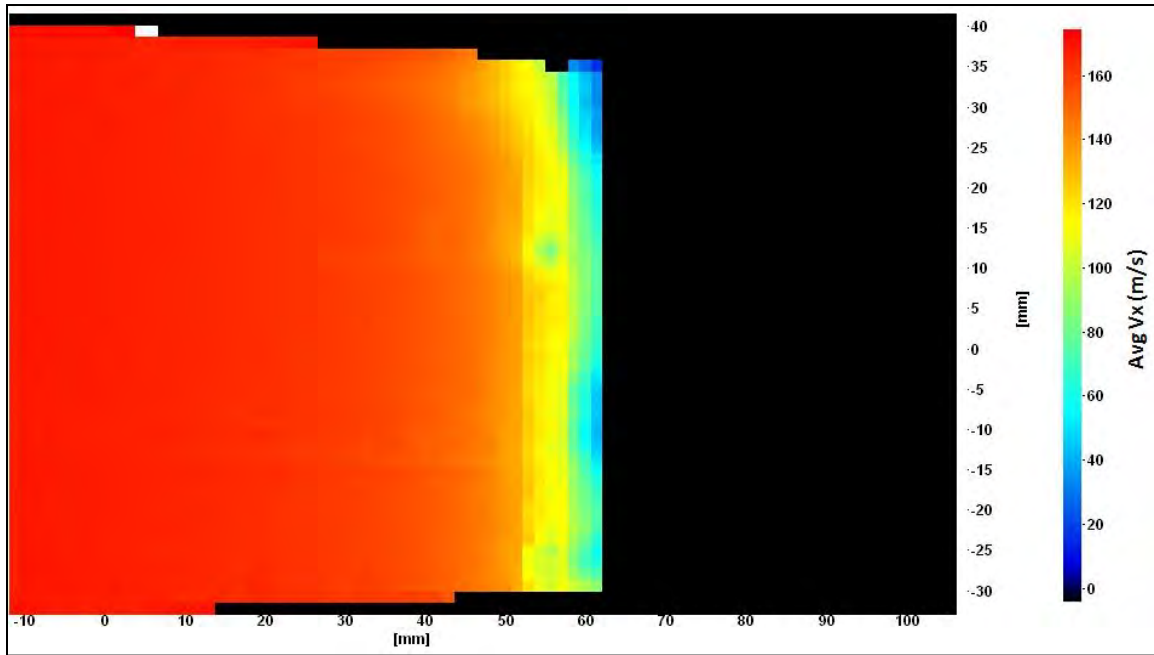


Figure 4.32: Streamwise velocity (V_x) for Experiment 33, $M = 0.5$, $P = 1044$ psf.

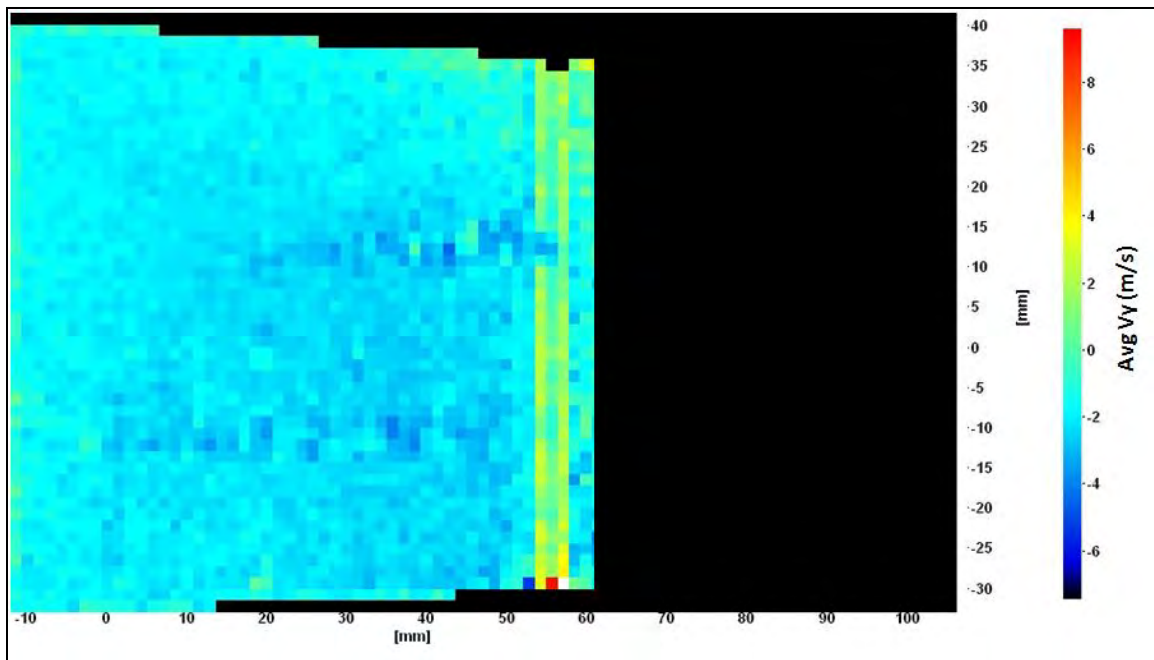


Figure 4.33: Perpendicular velocity (V_y) for Experiment 33, $M = 0.5$, $P = 1044$ psf.

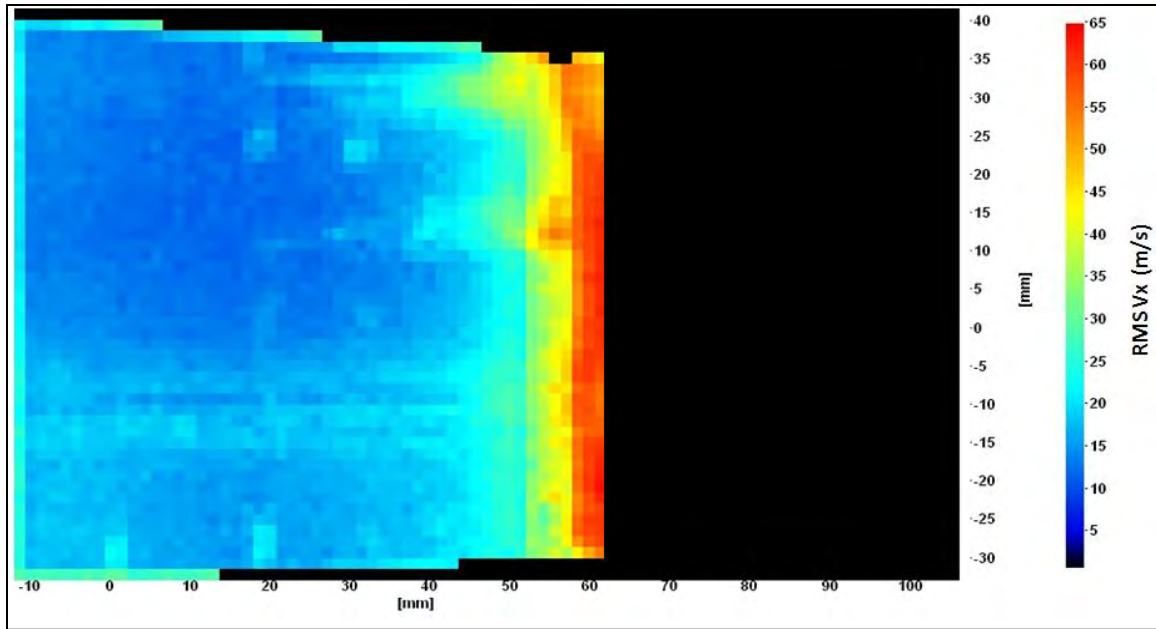


Figure 4.34: RMS streamwise velocity (V_x'), Experiment 33, $M = 0.5$, $P = 1044$ psf.

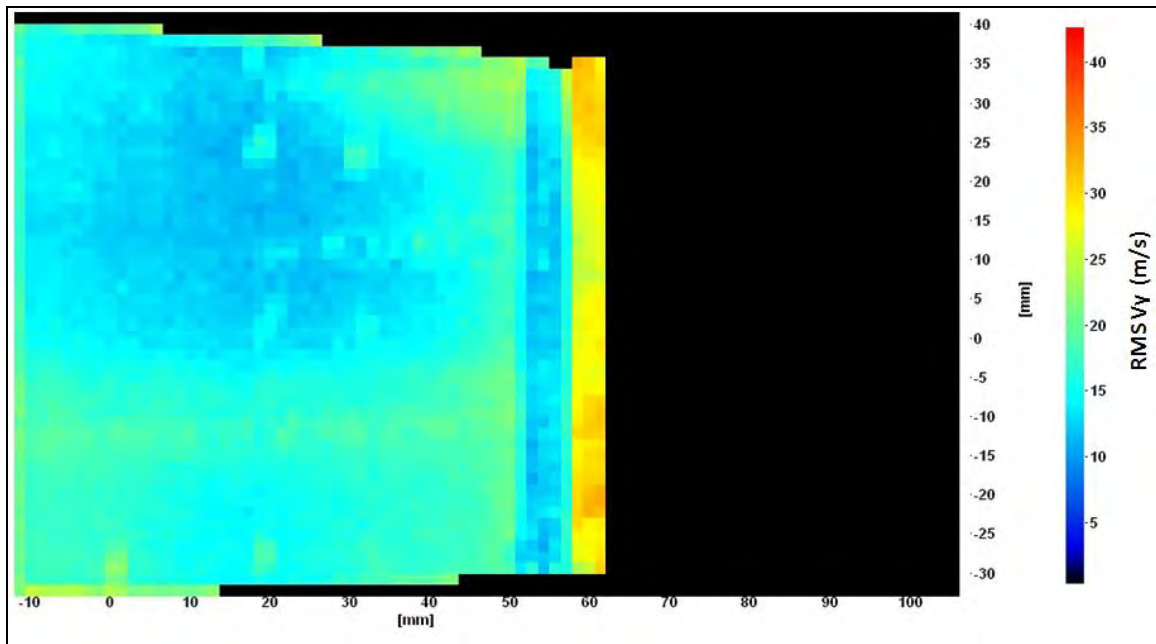


Figure 4.35: RMS perpendicular velocity (V_y'), Experiment 33, $M = 0.5$, $P = 1044$ psf.

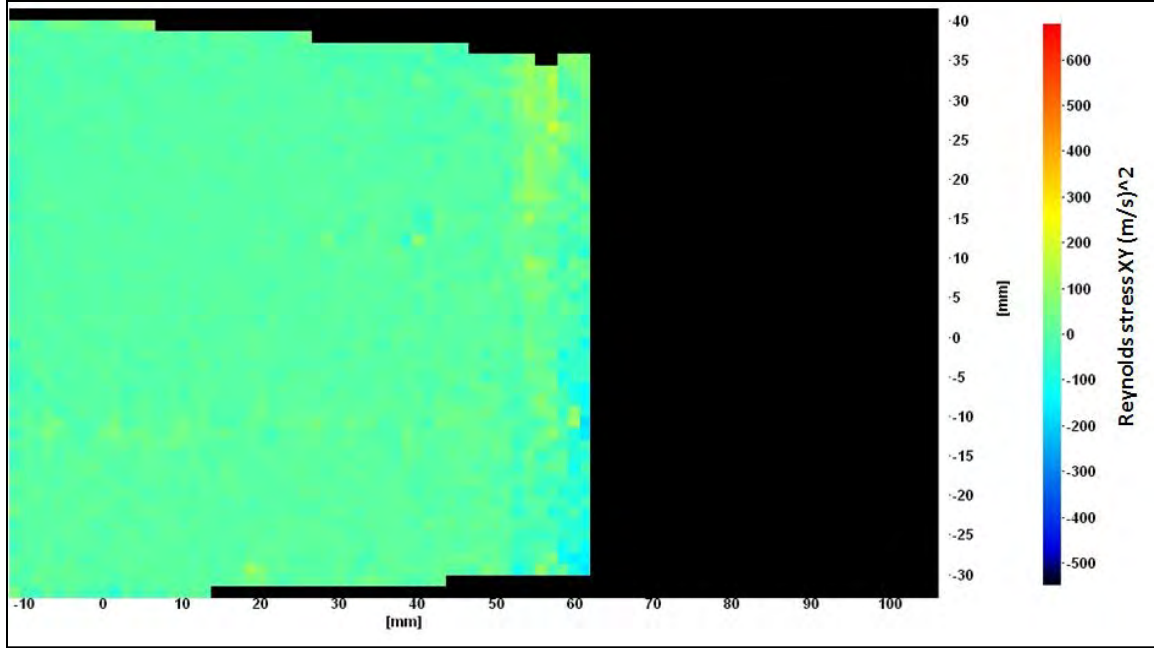


Figure 4.36: Absolute value of Reynolds stress ($V_x'V_y'$), Experiment 33, $M = 0.5$,
 $P = 1044$ psf.

The streamwise and perpendicular turbulence values are calculated by normalizing the RMS fluctuations, V_x' and V_y' , by the freestream velocity U_∞ . The Reynolds shear stress, $V_x'V_y'$, is normalized by the square of the freestream velocity to produce a non-dimensional quantity. Turbulence values with respect to distance from the wall, for Experiment 33, are plotted in Figure 4.37. The turbulence data follows a couple expected trends. First, turbulence is the greatest near the wall where the no-slip condition creates a velocity gradient that interacts with the flow velocity. Second, the streamwise turbulence is greater than that for the perpendicular direction. However, the magnitude of the turbulence data is much greater than expected and does not represent actual conditions in the TGF.

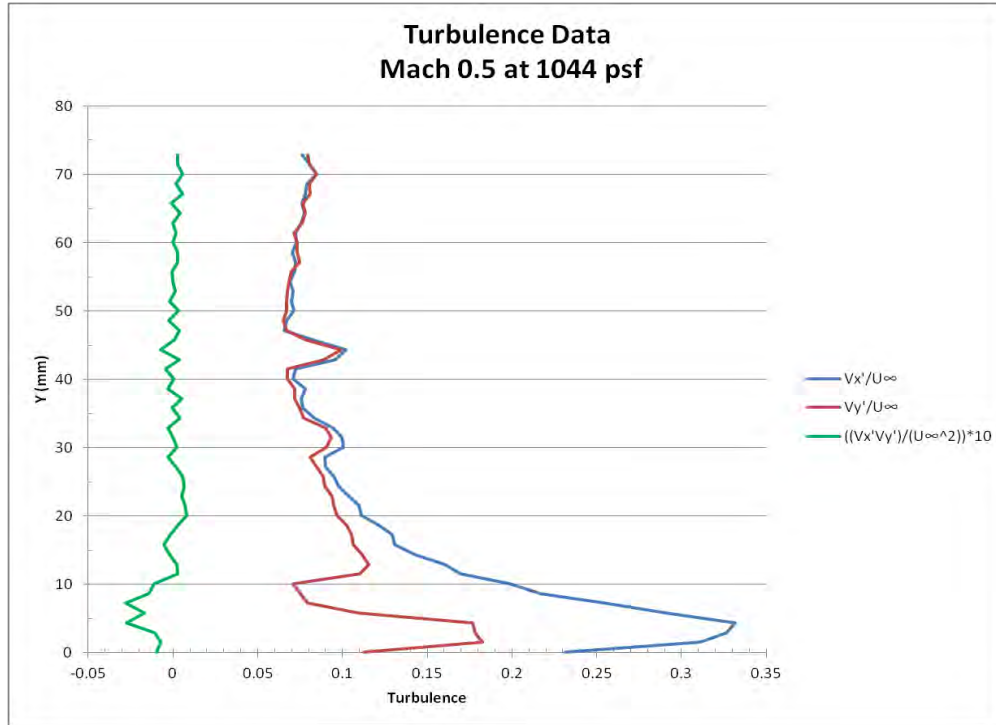


Figure 4.37: Turbulence data for Experiment 33, M = 0.5, P = 1044 psf.

Turbulence data was also analyzed for Experiment 25, Mach 0.3 at 1042 psf, and Experiment 31, Mach 0.8 at 1044 psf, for comparison. This data is presented in Figure 4.38 and Figure 4.39. In all cases streamwise turbulence peaks between 33 and 35%, while perpendicular turbulence peaks at approximately 18 or 19%. The shear stress turbulence peaks negatively between 0 mm and 10 mm then fluctuates near zero as distance from the wall increases. Analysis of the data reveals that the turbulence in the freestream is greatest for the Mach 0.3 case at about 12%. At Mach 0.5, freestream turbulence is approximately 7.5%. The minimum value for turbulence in the freestream occurs in the Mach 0.8 case between 3 and 4%. While the trends of this turbulence data are correct, the magnitudes of the data are incorrect and required further investigation to determine actual values.

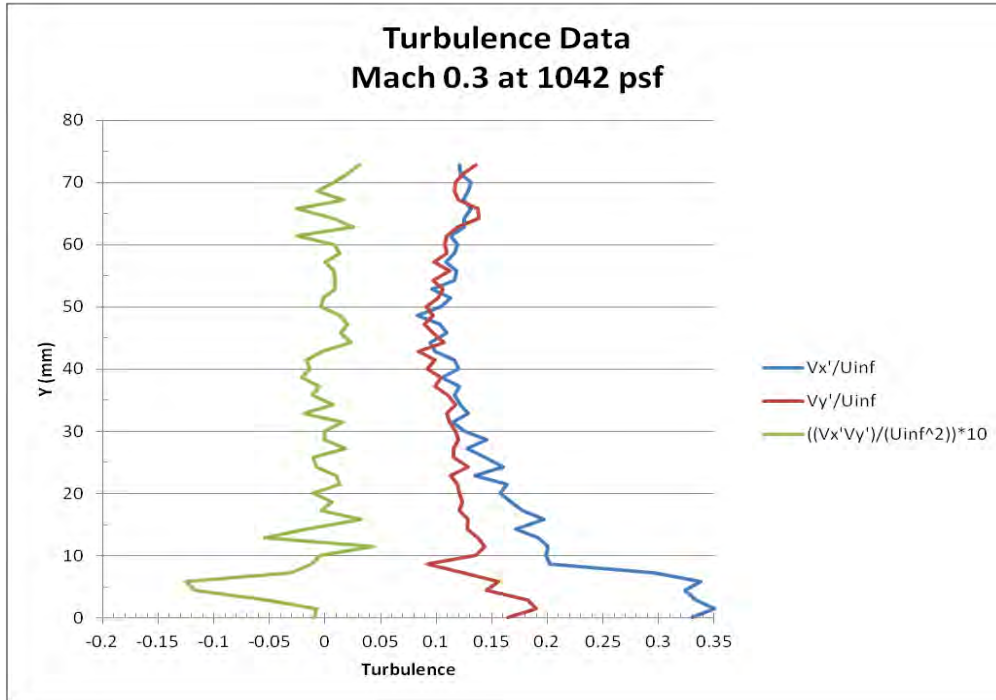


Figure 4.38: Turbulence data for Experiment 25, $M = 0.3$, $P = 1042$ psf.

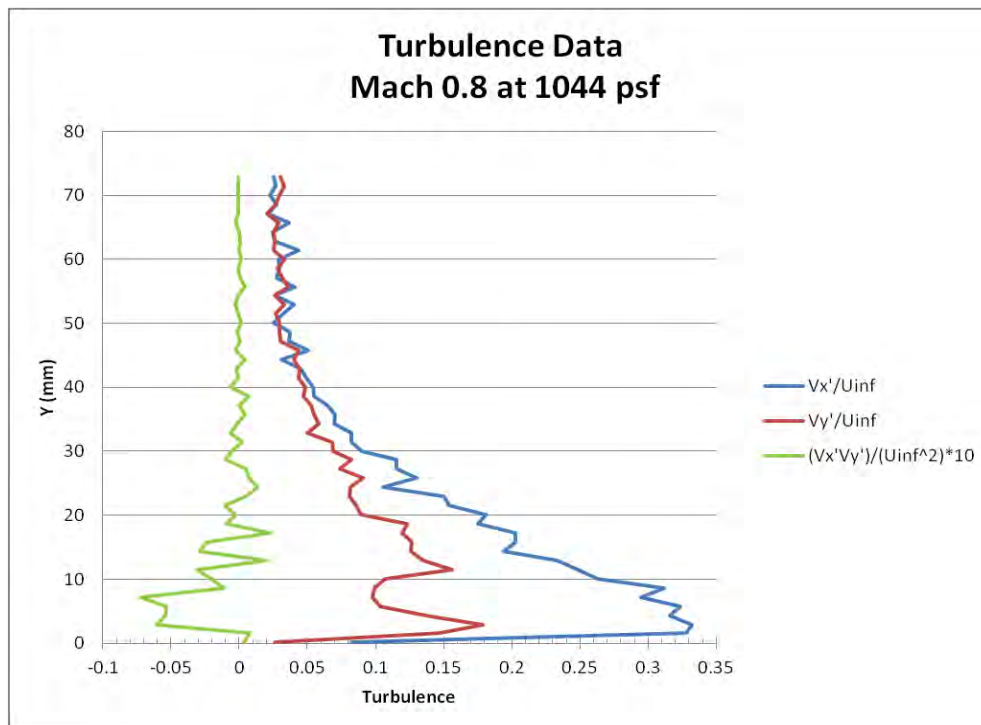


Figure 4.39: Turbulence data for Experiment 31, $M = 0.8$, $P = 1044$ psf.

4.4.1 Refined PIV Processing for Turbulence Measurements

The large values of the turbulence, especially in the freestream appeared unrealistic and prompted further investigation. Prior research done by Humble, Scarano and Oudheusden [19] suggested that using a PIV processing technique with rectangular IRs elongated in the streamwise direction to capture turbulence data. This may in part be explained by the fact that more particles will remain within the interrogation region while spatial resolution in the direction normal to the flow remains uncompromised. The LaVision software does not use rectangular IRs, but does allow for the use of elliptical areas. For the first pass an elliptical IR with a 1:2 diameter ratio was used with 50% overlap. The second pass utilized an elliptical IR with a 1:4 diameter ratio with 50% overlap. All other settings remained the same. Turbulence data for the Mach 0.5, 1044 psf case was calculated with this technique and is shown in Figure 4.40 below. Results show that turbulence in the freestream is at approximately 2% which is more in line with the expected value. While the maximum streamwise turbulence of 34% in the boundary remains high, it is skewed by the two points nearest the wall. Given the ambiguity in the exact wall location, one might argue that maximum turbulence levels are better represented as just over 15%. The perpendicular turbulence was measured to be less than 5% near the wall while shear stress turbulence remained low throughout the boundary layer. This turbulence data compares quite closely with the results of Klebanoff, given in Chapter 2, which is very encouraging. Further processing of data using elliptical interrogation regions, in particular the 10,000 image pair data set, is planned for the near future.

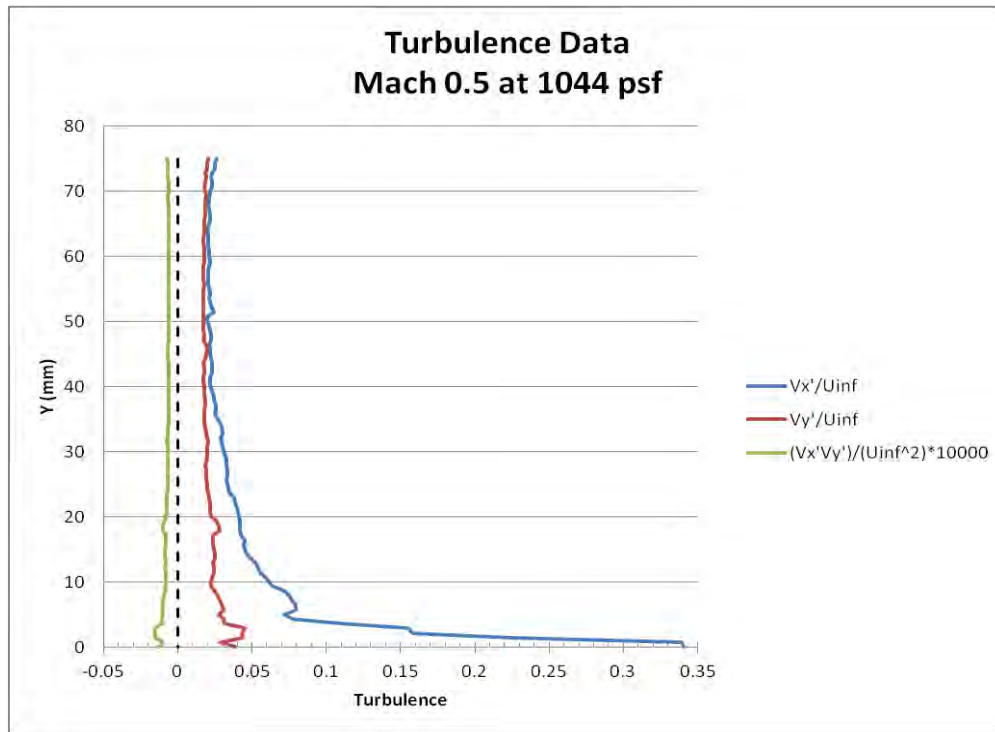


Figure 4.40: Improved turbulence data for Experiment 33, $M = 0.5$, $P = 1044$ psf.

4.5 Sources of Error

There are several potential sources of error which may explain the disagreements between PIV data and the expected results of freestream velocity, boundary layer thickness, and turbulence. The largest source of error is ambiguity of the exact wall location in the calibrated images due to the foam blocks used on the calibration plate. While these blocks were necessary to protect the highly polished tunnel window from being scratched, their use resulted in an unknown separation between the window and the edge of the calibration plate. This ambiguity, of just 3 or 4 mm, greatly affects the results of boundary layer thickness and turbulence data.

The production of CO₂ particles is sensitive to the stagnation pressure in the tunnel and introduces errors in two ways. First, the large particles formed at high stagnation pressures have greater mass and are not able to accurately follow accelerations in the flow field. This will create biases in the PIV measurements of freestream velocity and turbulence. Second, at lower stagnation pressures the particle number density decreases which reduces the statistical sample for analysis.

Laser light reflections off of the glass and metallic surfaces in the TGF limit PIV analysis of some regions of the raw images. In most cases, the LaVision software was not able to completely eliminate these reflections which introduce biases into the measurements.

Finally, the filter settings used to post-process the image pair vectors maps may not have eliminated some spurious vectors. These incorrect vectors are included in the final calculation of the flow field vector map and skew the PIV results. More stringent filter settings can be implemented at the risk of eliminating all data at certain points in the vector map where particle number density is very low.

V. Conclusions and Recommendations

5.1 *Overview of Research Effort*

PIV is a highly effective flow field analysis technique, but its usefulness is dependent on the proper selection of the particles used to seed the flow. Particle characteristics such as density and size are crucial to ensure the particles accurately respond to the flow dynamics. Additionally, particles must be large enough to reflect a sufficient amount of laser light to the cameras. Proper selection of seeding particles is especially important for use in closed-circuit wind tunnels where they can create safety hazards, cause corrosion, or leave behind residues which require extensive maintenance and down time. Facilities like the TGF, operated by AFRL/RB, have avoided using PIV in the past because of the impact of the seed material on tunnel components. Therefore, a method of cleanly seeding closed-circuit wind tunnels for PIV measurements is needed.

To this end, research has been performed on the use of solid CO₂ particles for flow seeding and collecting PIV data. Dry ice particles are produced by directing high pressure liquid CO₂ through an expansion orifice into a shroud tube which creates solidified particles that are injected into the wind tunnel stagnation chamber. Prior work had shown that the technique provided accurate freestream tunnel measurements in the TGF. However, prior to the current effort, the technique had not been applied to more complex flow fields where spatial resolution is a concern. This research primarily focused on using CO₂ particles for clean seeding to collect stereoscopic PIV data of the test section boundary layer in the TGF. Two different sets of shroud tubes were used to modify the size of CO₂ particles produced and the particle number density throughout the subsonic operating envelope of the TGF. Freestream velocity was set at Mach 0.3, Mach

0.5, or Mach 0.8 while absolute stagnation pressure ranged from 500 psf to 2400 psf. PIV data was analyzed to produce measurements of boundary layer thickness and compare results to theoretically expected values. Typically, 1000 image pairs were collected for PIV analysis of each tunnel condition. However, in one experiment, 10000 image pairs were collected to study the turbulence characteristics in the TGF test section.

5.2 *Conclusions*

The results of the study showed that boundary layer profiles can be accurately measured in the TGF using CO₂ seeding in combination with the LaVision PIV system, though some care must be exercised in generating properly sized particles and using correctly sized interrogation regions. Particle size and particle number density in the test section of the TGF is influenced by shroud tube diameter, stagnation pressure, and freestream velocity. The larger shroud tubes have an ID of 0.824 inches and consistently lead to larger CO₂ particles, compared to the small shroud tubes with an ID of 0.364 inches, at equivalent wind tunnel conditions. This research shows stagnation pressure has a large effect on particle sublimation rate in the TGF. At stagnation pressures under 1000 psf, small particles generated by the 0.364 inch ID shroud tubes sublime prior to reaching the TGF test section making PIV measurement difficult if not impractical. The larger shroud tubes produce particles large enough to provide sufficient laser light reflection and flow field coverage at all tested Mach numbers under a stagnation pressure of 1000 psf. However, at higher stagnation pressures, over 2000 psf, the 0.824 inch shroud tubes produce relatively large particles. These large particles have slower response times and do not respond as quickly to the dynamics of the flow field being

studied. Finally, freestream velocity affects particle size and particle number density in the test section. CO₂ particles begin to sublime after leaving the shroud tubes. Particles traveling at higher velocities will reach the test section faster and therefore retain a larger portion of their original size than particles dispersed in a flow field with lower airspeed. For example, the smaller shroud tubes produced better particle coverage at Mach 0.8 conditions than at Mach 0.3 conditions for a given pressure.

Boundary layer profiles were analyzed in detail for thirteen cases. In general, the measured boundary layer thickness closely matched expectations, based on flow over a flat plate, if a length scale of 3.8 meters is utilized. Given the dimensions of the TGF nozzle and test section, this value is reasonable.

Finally, PIV data of 10000 image pairs was collected in order to analyze the turbulence near the wall of the TGF test section at Mach 0.5. RMS fluctuations of the streamwise and perpendicular velocities were normalized by the freestream velocity while Reynolds shear stress was normalized by the square of the freestream velocity and plotted against distance from the wall. Data followed expected trends showing the highest turbulence in the streamwise direction and a decrease in total turbulence as distance from the wall increases. Turbulence data from Mach 0.3 and Mach 0.8 showed similar results and revealed that freestream turbulence decreases as velocity increases. The initial processing method resulted greater than expected magnitudes for the turbulence values. A refined PIV method, using elongated elliptical interrogation regions, significantly improved the turbulence data results.

5.3 *Impact of Research*

For the first time a CO₂ distribution manifold was used to inject clean seeding particles in the TGF stagnation chamber in order to analyze the test section boundary layer through stereoscopic PIV. Closed-circuit wind tunnel facilities like the TGF can benefit from this method because of the low cost and availability of liquid CO₂, the ability to tune particle size to tunnel conditions, and because the particles do not cause safety hazards or maintenance problems. Properly sized particles can be used in combination with PIV systems to accurately analyze freestream and boundary layer velocity profiles and determine turbulence characteristics in production scale wind tunnels. Finally, the CO₂ injector design may be adjusted to produce correctly sized particles in other closed-circuit tunnels. The distance between the injection point and the test section, the speed of the air flow, and the stagnation pressure are important variables that affect the sublimation rate and residence time of the CO₂ particles.

5.4 *Future Work*

This and previous research have demonstrated the capabilities and limitations of CO₂ particle flow seeding for PIV measurement. The technique has been successfully implemented in small scale tunnels and the TGF. Future work at the TGF may be devoted to improving optical access for the laser light sheet in the test section. Currently the light sheet cannot be projected in a vertical plane over a model in the test section. This improvement would allow future researches to capture clean seeding PIV data of flow fields around aerodynamic models significantly expanding the capabilities of the TGF for AFRL.

CO₂ has been used as seed material for supersonic flow in small scale tunnels at AFIT. However, this technique has not yet been executed in the TGF at supersonic speeds. Future work may be done to design injectors that produce properly sized particles at sufficient particle number densities to perform PIV measurements in this flow regime at the TGF.

Finally, future work could include the full scale introduction and use of dry ice seeding in large scale facilities such as the 16-foot transonic (16T) wind tunnel located at Arnold Engineering Development Center, Arnold Air Force Base.

Appendix A. Wind Tunnel Instrumentation Data

Table A.1: 2 September 2011, TGF Instrumentation Data.

Clock Time YYYY-MM-DD HH:mm:ss.ff	POPSF PSFA	PSPSF PSFA	T0 °R	MACH_STD	Q_STD PSF	Velocity_STD ft/sec	Re/ft	TS_STD °R	Rho lbm/ft ³
2011-09-02 02:05:31Z	554.24	518.07	534.39	0.312	35.31	350.04	139283	524.18	0.01852901
2011-09-02 02:06:35Z	551.11	514.45	534.46	0.315	35.77	353.5	139743	524.04	0.01840477
2011-09-02 02:10:16Z	553.09	514.14	534.51	0.325	37.94	364	144087	523.47	0.01841362

Table A.2: 6 September 2011, TGF Instrumentation Data.

Clock Time YYYY-MM-DD HH:mm:ss.ff	POPSF PSFA	PSPSF PSFA	T0 °R	MACH_STD	Q_STD PSF	Velocity_STD ft/sec	Re/ft	TS_STD °R	Rho lbm/ft ³
2011-09-06 00:30:13Z	1044.38	881.49	533.77	0.498	153.15	550.49	393345	508.52	0.03249808
2011-09-06 00:30:25Z	1042.94	880.31	534.13	0.498	152.91	550.62	392438	508.86	0.03243239
2011-09-06 00:31:33Z	1044.05	876.9	534.39	0.506	156.87	558.54	397156	508.42	0.03233498
2011-09-06 00:31:52Z	1043.9	875.43	534.47	0.508	158.02	560.96	398434	508.26	0.03229102
2011-09-06 00:36:32Z	651.76	611.85	533.11	0.302	39.01	338.39	159352	523.56	0.02190892
2011-09-06 00:36:42Z	649.36	609.74	533.43	0.301	38.73	337.86	158373	523.9	0.02181947
2011-09-06 00:40:25Z	650.66	607.5	529.32	0.315	42.11	351.29	166805	519.03	0.02194304
2011-09-06 00:40:34Z	652.23	608.64	529.1	0.316	42.52	352.54	167889	518.73	0.02199713
2011-09-06 00:45:34Z	554.39	519.68	531.07	0.305	33.91	341.58	137643	521.38	0.01868677
2011-09-06 00:45:44Z	550.45	515.96	530.51	0.305	33.7	341.56	136924	520.79	0.01857388
2011-09-06 00:46:31Z	553.12	517.53	528.87	0.31	34.76	345.75	139903	518.94	0.01869659
2011-09-06 00:46:42Z	552.65	516.91	528.55	0.311	34.9	346.52	140231	518.56	0.01868784
2011-09-06 00:48:35Z	552.26	514.77	530.03	0.318	36.55	355.67	142881	519.5	0.0185772
2011-09-06 00:48:46Z	552.37	514.99	530.32	0.318	36.45	355.22	142615	519.79	0.01857453
2011-09-06 00:50:38Z	303.08	284.62	532.37	0.301	18.05	337.29	74059	522.87	0.01020497
2011-09-06 00:50:47Z	307.35	288.75	532.26	0.3	18.18	336.06	74867	522.84	0.01035373
2011-09-06 00:52:04Z	305.77	286.57	530.92	0.306	18.76	342.09	76063	521.19	0.01030815
2011-09-06 00:52:17Z	309.17	289.35	530.33	0.309	19.35	345.51	77782	520.39	0.0104243
2011-09-06 00:53:14Z	306.19	285.65	528.18	0.317	20.03	352.91	79128	517.8	0.0103423
2011-09-06 00:53:22Z	305.72	285.13	528.01	0.317	20.09	353.64	79207	517.58	0.01032779
2011-09-06 00:58:25Z	453.9	425.94	530.05	0.303	27.32	338.43	112098	520.53	0.01534099
2011-09-06 00:58:32Z	452.78	424.93	530	0.303	27.22	338.2	111772	520.49	0.01530576
2011-09-06 00:59:13Z	456.37	427.27	529.52	0.308	28.41	344.28	114737	519.65	0.01541485
2011-09-06 00:59:28Z	453.12	423.99	529.26	0.31	28.44	345.65	114446	519.3	0.01530678
2011-09-06 01:05:39Z	1043.49	972.17	531.01	0.32	69.53	357.29	270238	520.39	0.03502327
2011-09-06 01:05:47Z	1043.24	971.7	530.92	0.32	69.73	357.86	270642	520.28	0.03501434
2011-09-06 01:07:07Z	1043.86	970.96	530.72	0.323	71.03	361.16	273318	519.86	0.03501523
2011-09-06 01:07:17Z	1042.43	969.54	530.66	0.323	71.01	361.37	273135	519.8	0.03496866
2011-09-06 01:10:04Z	1043.42	975.33	534.23	0.312	66.46	349.96	262294	524.03	0.03489363
2011-09-06 01:10:13Z	1045.86	977.63	534.16	0.312	66.59	349.87	262909	523.95	0.03498079
2011-09-06 01:12:36Z	1723.65	1617.73	532.77	0.302	103.53	338.9	422448	523.23	0.05796462
2011-09-06 01:12:45Z	1722.32	1616.89	532.65	0.302	103.06	338.18	421475	523.13	0.05794553
2011-09-06 01:13:48Z	1729.36	1622.91	532.66	0.303	104.04	339.15	424291	523.1	0.05816442
2011-09-06 01:14:11Z	1727.75	1621.27	533.83	0.303	104.08	339.74	423020	524.2	0.05798371
2011-09-06 01:18:31Z	2402.46	2258.01	538.86	0.299	141.26	337.04	574354	529.39	0.07996496
2011-09-06 01:18:41Z	2406.26	2261.97	538.64	0.299	141.12	336.52	574845	529.2	0.08013398
2011-09-06 01:19:38Z	2405.93	2261.39	538.14	0.299	141.36	336.68	575932	528.7	0.08018884
2011-09-06 01:19:49Z	2404.43	2259.98	538.27	0.299	141.27	336.72	575394	528.83	0.08011958
2011-09-06 01:22:55Z	1340	1259.22	539.13	0.299	78.99	337.58	320558	529.62	0.04457405
2011-09-06 01:23:05Z	1338.93	1258.44	539.47	0.299	78.71	337.2	319595	530	0.04451466
2011-09-06 01:23:47Z	1336.81	1256.88	539.29	0.298	78.17	336.21	318407	529.86	0.044471
2011-09-06 01:24:06Z	1320.93	1241.82	539.66	0.298	77.37	336.61	314587	530.22	0.04390826
2011-09-06 01:26:10Z	847.93	796.34	534.62	0.301	50.44	337.75	205931	525.11	0.0284314
2011-09-06 01:26:19Z	847.32	795.95	534.43	0.3	50.23	337.09	205533	524.96	0.02842551
2011-09-06 01:27:03Z	846.31	795.04	533.64	0.3	50.13	336.71	205591	524.2	0.02843407
2011-09-06 01:27:16Z	849.29	798.06	533.6	0.299	50.09	335.94	205897	524.2	0.02854199

Table A.3: 7 September 2011, TGF Instrumentation Data.

Clock Time YYYY-MM-DD HH:mm:ss.ff	POPSF PSFA	PSPSF PSFA	T0 °R	MACH_STD	Q_STD PSF	Velocity_STD ft/sec	Re/ft	TS_STD °R	Rho lbm/ft³
2011-09-07 00:25:07Z	1041.31	878.95	530.43	0.498	152.65	548.68	395279	505.37	0.03260667
2011-09-07 00:25:17Z	1043.13	880.57	530.44	0.498	152.85	548.53	395892	505.37	0.03266618
2011-09-07 00:28:25Z	1045.07	880	531.91	0.502	155.07	553.23	397588	506.4	0.03257891
2011-09-07 00:28:39Z	1042.72	876.96	532	0.504	155.64	555.19	397684	506.35	0.03246957
2011-09-07 00:33:03Z	555.09	465.03	529.83	0.509	84.44	560.11	214745	503.71	0.01730823
2011-09-07 00:33:12Z	549.27	460.17	530.09	0.509	83.54	560.19	212346	503.96	0.01711891
2011-09-07 00:34:06Z	552.53	462.31	532.83	0.511	84.56	563.61	212827	506.35	0.01711695
2011-09-07 00:34:16Z	554.05	463.34	533.17	0.512	84.99	564.58	213464	506.62	0.01714608
2011-09-07 00:39:22Z	797.42	660.79	529.91	0.525	127.59	576.72	315850	502.22	0.02466675
2011-09-07 00:39:30Z	796.92	660.72	529.97	0.524	127.21	575.96	315267	502.34	0.02465845
2011-09-07 00:41:05Z	791.94	652.29	531.86	0.534	130.12	586.74	316168	503.14	0.02430498
2011-09-07 00:41:14Z	798.72	657.78	532.24	0.534	131.31	587.15	318659	503.49	0.02449255
2011-09-07 00:49:29Z	1529.19	1277.09	538.11	0.514	236.09	569.28	584041	511.1	0.04684493
2011-09-07 00:49:40Z	1526.68	1275.67	538.31	0.513	235.13	568.6	582100	511.39	0.04676616
2011-09-07 00:52:37Z	1526.14	1273.46	536.44	0.515	236.57	569.72	586296	509.4	0.04686758
2011-09-07 00:52:47Z	1531.17	1277.62	536.3	0.515	237.38	569.69	588468	509.26	0.04703376
2011-09-07 01:01:03Z	552.54	517.93	533.32	0.305	33.82	342.42	136498	523.56	0.0185459
2011-09-07 01:01:11Z	554.7	519.93	533.39	0.305	33.96	342.52	137049	523.6	0.01861626
2011-09-07 01:04:26Z	554.4	517.06	532.78	0.317	36.42	355.21	141974	522.28	0.01856022
2011-09-07 01:04:35Z	551.67	514.48	532.68	0.317	36.27	355.33	141381	522.14	0.01847262
2011-09-07 01:07:47Z	1040.89	974.23	531.01	0.309	65.09	345.55	261323	521.05	0.03505342
2011-09-07 01:07:57Z	1041.75	975.23	531.04	0.308	64.96	345.05	261162	521.11	0.03508546
2011-09-07 01:08:41Z	1044.1	976.58	531.37	0.311	65.92	347.42	263137	521.31	0.03511989
2011-09-07 01:08:49Z	1042.55	974.78	531.56	0.311	66.15	348.39	263254	521.46	0.03504556
2011-09-07 01:15:15Z	2012.52	1888.95	535.78	0.302	120.79	339.71	489550	526.17	0.06730348
2011-09-07 01:15:24Z	2015.11	1891.66	535.67	0.302	120.67	339.28	489783	526.08	0.06741284

Table A.4: 8 September 2011, TGF Instrumentation Data.

Clock Time YYYY-MM-DD HH:mm:ss.ff	POPSF PSFA	PSPSF PSFA	T0 °R	MACH_STD	Q_STD PSF	Velocity_STD ft/sec	Re/ft	TS_STD °R	Rho lbm/ft³
2011-09-08 01:39:14Z	552.46	517.27	530.89	0.308	34.37	344.56	138387	520.98	0.01861417
2011-09-08 01:39:27Z	548.03	513.16	530.94	0.308	34.06	344.43	137194	521.06	0.0184632
2011-09-08 01:40:35Z	550.1	514	530.36	0.313	35.23	349.71	139948	520.18	0.01852476
2011-09-08 01:58:20Z	552.91	516.17	529.57	0.315	35.84	351.66	141769	519.25	0.01863632
2011-09-08 02:04:23Z	1041.13	974.86	529.97	0.308	64.73	344.16	261291	520.09	0.03514034
2011-09-08 02:08:24Z	1044.34	978.74	534.25	0.306	64.09	343.21	257780	524.43	0.03498853
2011-09-08 02:08:34Z	1042.73	976.77	533.98	0.307	64.42	344.33	258376	524.12	0.03493908
2011-09-08 02:31:52Z	1526.77	1431.89	535.7	0.304	92.72	341.8	373611	525.99	0.05103628
2011-09-08 02:32:00Z	1528.46	1433.68	535.59	0.304	92.62	341.36	373720	525.89	0.05111032
2011-09-08 02:32:42Z	1532.62	1436.7	534.94	0.305	93.72	342.78	376999	525.15	0.05128937
2011-09-08 02:32:55Z	1536.76	1439.92	534.92	0.306	94.59	343.96	379270	525.06	0.05141342
2011-09-08 02:48:34Z	2017.83	1891.13	539.19	0.306	123.78	344.72	492103	529.32	0.06698011
2011-09-08 02:48:42Z	2018.64	1891.61	539.26	0.306	124.1	345.12	492797	529.32	0.06699757
2011-09-08 02:54:12Z	2018.41	1893.12	540.68	0.304	122.44	343.18	487869	530.88	0.06685417
2011-09-08 02:54:26Z	2015.57	1890.34	540.81	0.304	122.38	343.38	487277	530.98	0.06674367
2011-09-08 03:13:31Z	2397.41	2252.15	545.09	0.3	142.03	340.31	566942	535.42	0.07885926
2011-09-08 03:14:15Z	2395.91	2251.14	544.43	0.3	141.56	339.64	566657	534.84	0.07890921
2011-09-08 03:14:50Z	2378.51	2234.34	543.89	0.3	140.97	340.02	564123	534.26	0.07840443
2011-09-08 03:21:48Z	2409.71	2263.6	546.08	0.3	142.87	340.77	568682	536.43	0.07910993

Table A.5: 12 September 2011, TGF Instrumentation Data.

Clock Time YYYY-MM-DD HH:mm:ss.ff	POPSF PSFA	PSPSF PSFA	T0 °R	MACH_STD	Q_STD PSF	Velocity_STD ft/sec	Re/ft	TS_STD °R	Rho lbm/ft³
2011-09-11 23:08:02Z	554.23	363.4	532.28	0.801	163.01	852.01	286983	471.8	0.01444034
2011-09-11 23:08:11Z	552.33	362.66	532.29	0.799	162.11	850.72	285725	472.02	0.0144041
2011-09-11 23:11:48Z	552.55	354.69	529.81	0.822	167.62	869.86	291509	466.79	0.01424537
2011-09-11 23:21:09Z	550.75	357.08	530.15	0.812	164.71	860.88	288632	468.42	0.0142915
2011-09-11 23:25:56Z	798.07	514.7	532.53	0.817	240.5	867.74	417132	469.81	0.02053933
2011-09-11 23:26:05Z	798.08	514.97	532.38	0.817	240.33	867.16	417155	469.75	0.02055226
2011-09-11 23:30:50Z	799.88	516.93	533.29	0.815	240.35	866.44	416827	470.74	0.0205875
2011-09-11 23:31:03Z	797.86	512.58	533.68	0.821	241.77	872.28	416784	470.31	0.02043269
2011-09-11 23:46:33Z	1044.06	670.48	534.86	0.821	316.55	873.62	543956	471.29	0.026671
2011-09-11 23:46:51Z	1045.32	670.99	534.86	0.822	317.12	874.03	544736	471.24	0.02669433
2011-09-11 23:47:14Z	1045.55	673.36	534.77	0.818	315.72	870.89	543948	471.6	0.02676808
2011-09-11 23:51:10Z	1045.54	672.58	535.57	0.82	316.23	872.61	543258	472.15	0.02670602
2011-09-11 23:51:19Z	1042.66	668.5	535.6	0.823	316.83	875.71	542739	471.74	0.02656744
2011-09-12 00:05:26Z	1231.5	796.74	538.87	0.814	369.45	869.96	632690	475.84	0.03139097
2011-09-12 00:05:35Z	1234.88	797.56	539.01	0.816	371.38	871.67	634856	475.73	0.03143058
2011-09-12 00:10:02Z	1243.37	804.28	539.9	0.814	373.11	870.95	637283	476.72	0.03162942
2011-09-12 00:10:10Z	1240.07	801.05	539.9	0.815	372.85	872.23	636109	476.53	0.03151482

Table A.6: 13 September 2011, TGF Instrumentation Data.

Clock Time YYYY-MM-DD HH:mm:ss.ff	POPSF PSFA	PSPSF PSFA	T0 °R	MACH_STD	Q_STD PSF	Velocity_STD ft/sec	Re/ft	TS_STD °R	Rho lbm/ft³
2011-09-13 00:06:50Z	1043.42	881.05	529.75	0.498	152.69	547.77	396404	504.76	0.0327233
2011-09-13 00:06:59Z	1044.62	881.87	529.8	0.498	153.04	548.14	397016	504.79	0.03275235
2011-09-13 00:11:16Z	1044.39	876.34	534.15	0.507	157.66	559.92	398394	508.06	0.03233764
2011-09-13 00:12:08Z	1045.73	870.94	533.46	0.518	163.53	571.02	406292	506.29	0.03225016

Table A.7: 21 September 2011, TGF Instrumentation Data.

Clock Time YYYY-MM-DD HH:mm:ss.ff	POPSF PSFA	PSPSF PSFA	T0 °R	MACH_STD	Q_STD PSF	Velocity_STD ft/sec	Re/ft	TS_STD °R	Rho lbm/ft³
2011-09-20 23:32:02Z	1042.47	977.48	533.81	0.305	63.5	341.71	256643	524.06	0.03496823
2011-09-20 23:33:35Z	1045.09	978.66	534.83	0.308	64.88	345.49	259069	524.89	0.03495508
2011-09-20 23:46:08Z	799.5	750.86	532.91	0.301	47.56	337.21	194962	523.43	0.02689359
2011-09-20 23:47:02Z	797.89	748.43	532.71	0.304	48.33	340.37	196396	523.07	0.02682498
2011-09-20 23:51:57Z	1529.86	1435.91	534.86	0.302	91.83	339.45	372993	525.26	0.05125076
2011-09-20 23:52:56Z	1532.92	1438.03	535.01	0.304	92.74	340.89	375052	525.32	0.05132043
2011-09-21 00:10:54Z	1044.5	976.07	537.74	0.313	66.78	351.81	260867	527.43	0.03469516
2011-09-21 00:11:40Z	1043.24	974.35	537.77	0.314	67.21	353.24	261508	527.38	0.03463679
2011-09-21 00:14:50Z	1043.46	878.34	538.12	0.502	155.1	557.02	391418	512.28	0.03214395
2011-09-21 00:16:35Z	1039.93	874.42	537.71	0.504	155.39	558.51	391450	511.74	0.03203455
2011-09-21 00:25:28Z	800.52	674.08	536.99	0.502	118.78	555.87	300847	511.26	0.0247184
2011-09-21 00:27:08Z	797.91	671.63	536.87	0.502	118.61	556.41	300229	511.08	0.02463707
2011-09-21 00:34:21Z	1524.85	1285.02	539.22	0.501	225.35	555.76	568970	513.49	0.04691668
2011-09-21 00:35:29Z	1533.58	1290.26	540.08	0.503	228.5	558.8	573282	514.06	0.04705554
2011-09-21 00:48:19Z	551.36	361.9	539.69	0.799	161.91	856.94	280233	478.53	0.01417825
2011-09-21 00:49:31Z	552.82	359.78	539.66	0.808	164.42	864.99	282485	477.32	0.01413101
2011-09-21 00:54:43Z	1519.78	1014.26	543.71	0.783	434.8	843.95	756788	484.39	0.03925546
2011-09-21 00:55:10Z	1524.4	1002.6	543.82	0.797	446.26	858.25	766211	482.46	0.03895927
2011-09-21 00:56:07Z	1530.37	1001.43	544.09	0.803	451.49	863.33	771231	481.98	0.03895279
2011-09-21 01:00:38Z	1044.63	665.89	542.69	0.829	319.98	886.86	536321	477.19	0.02616126
2011-09-21 01:01:17Z	1045.62	658.78	542.93	0.84	325.34	897.76	539936	475.8	0.02595751

Appendix B. Clauser Plots

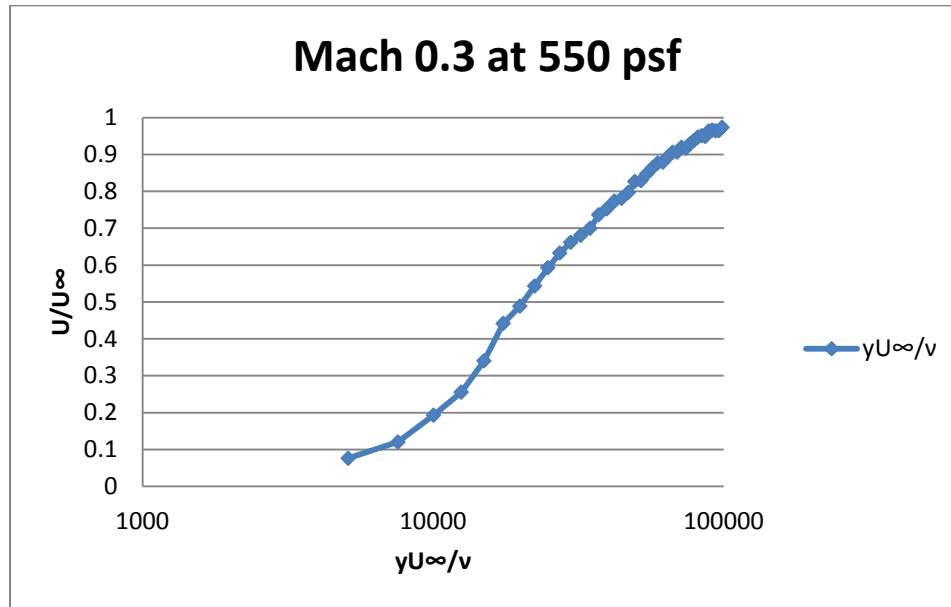


Figure B.1: Clauser plot for 0.824 inch ID shroud tubes at $M = 0.3$, $P = 550$ psf.

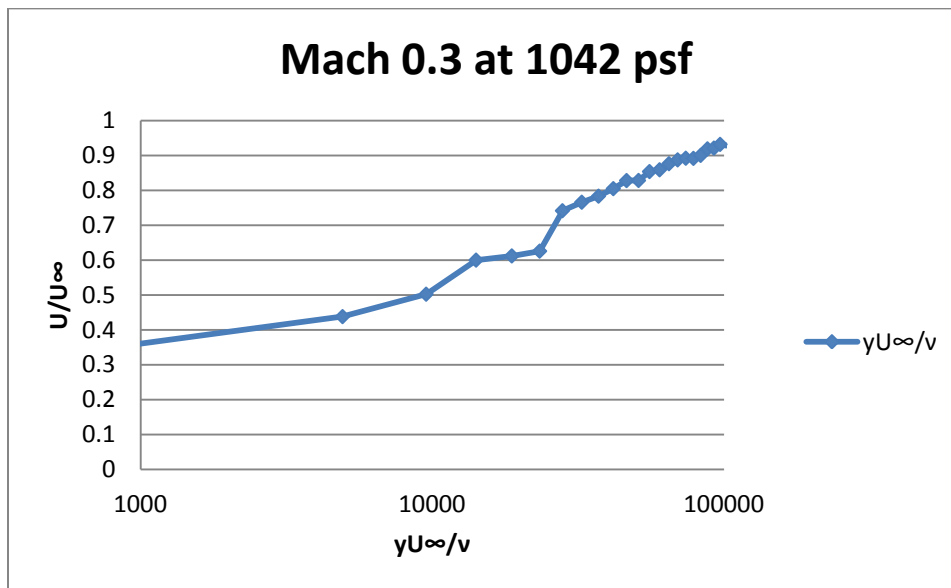


Figure B.2: Clauser plot for 0.824 inch ID shroud tubes at $M = 0.3$, $P = 1042$ psf.

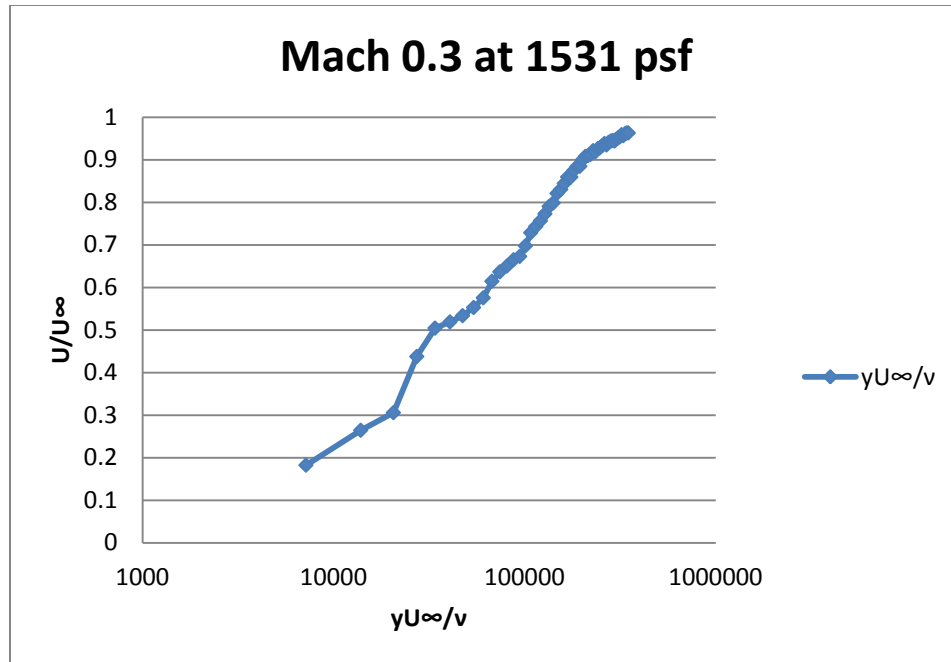


Figure B.3: Clauser plot for 0.824 inch ID shroud tubes at $M = 0.3$, $P = 1531$ psf.

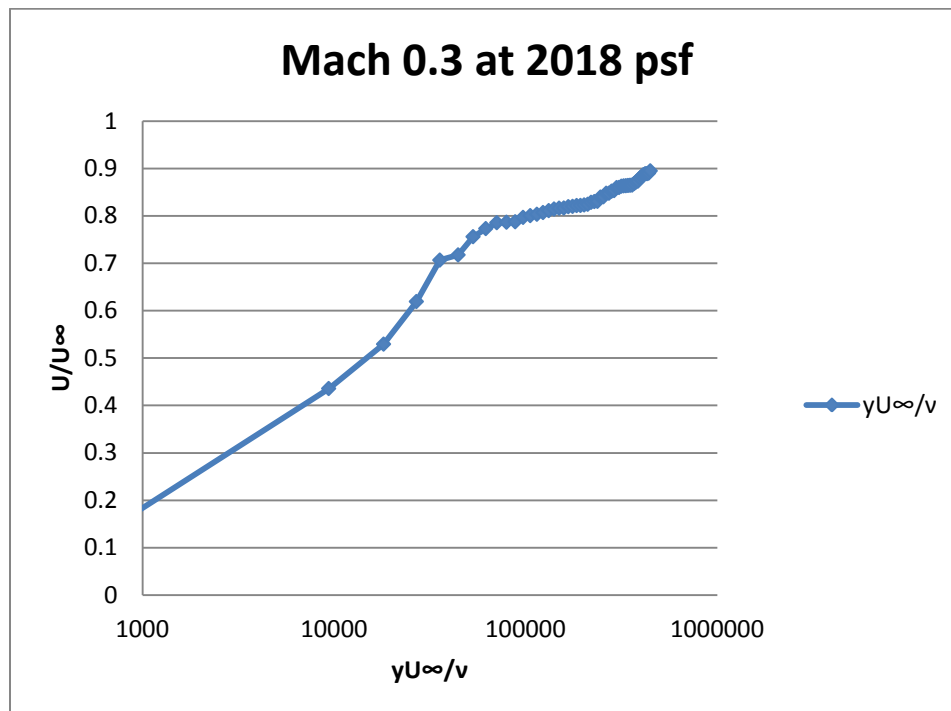


Figure B.4: Clauser plot for 0.824 inch ID shroud tubes at $M = 0.3$, $P = 2018$ psf.

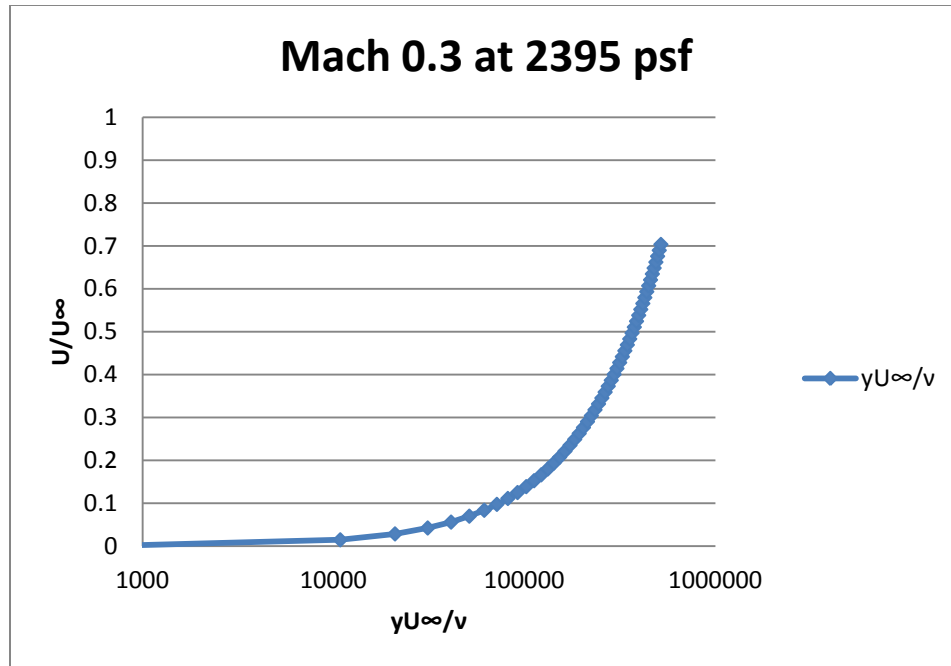


Figure B.5: Clauser plot for 0.824 inch ID shroud tubes at $M = 0.3$, $P = 2395$ psf.

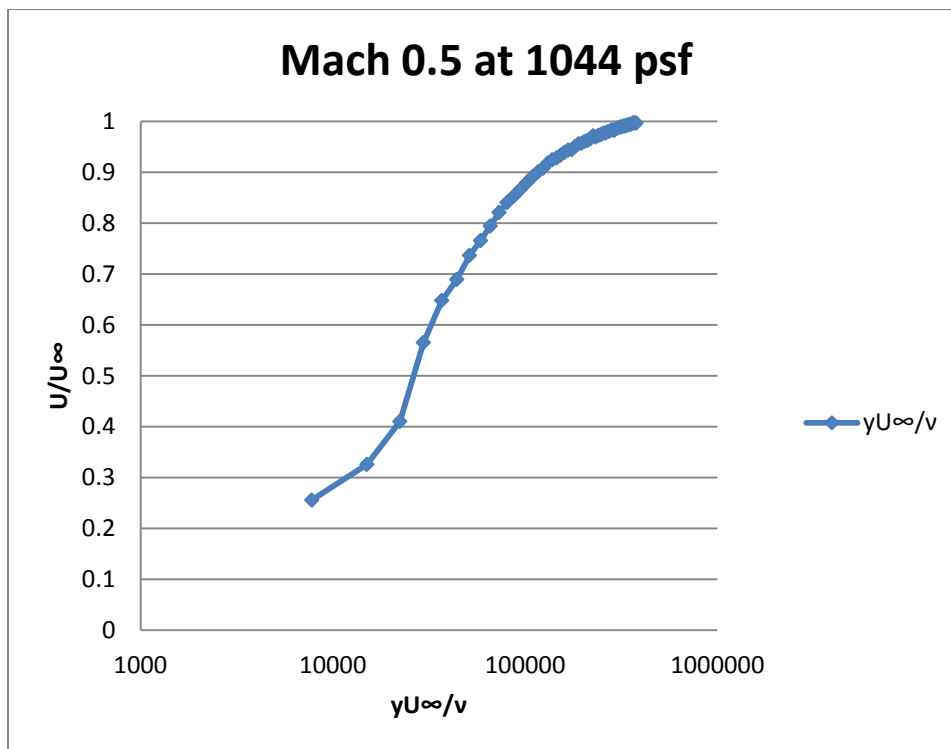


Figure B.6: Clauser plot for 0.824 inch ID shroud tubes at $M = 0.5$, $P = 1044$ psf.

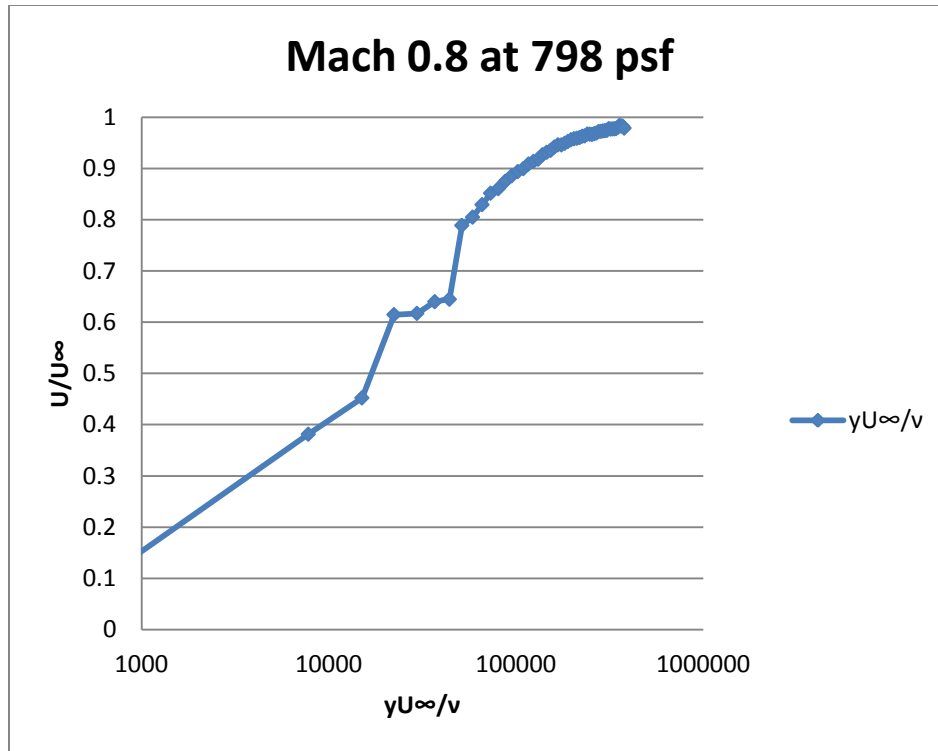


Figure B.7: Clauser plot for 0.824 inch ID shroud tubes at $M = 0.8$, $P = 798$ psf.

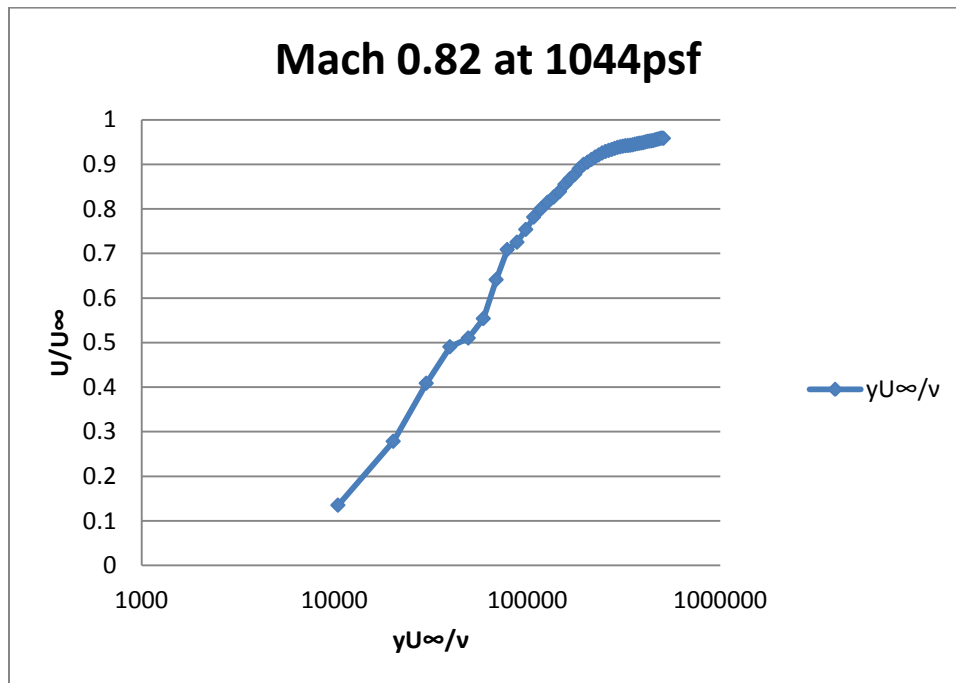


Figure B.8: Clauser plot for 0.824 inch ID shroud tubes at $M = 0.82$, $P = 1044$ psf.

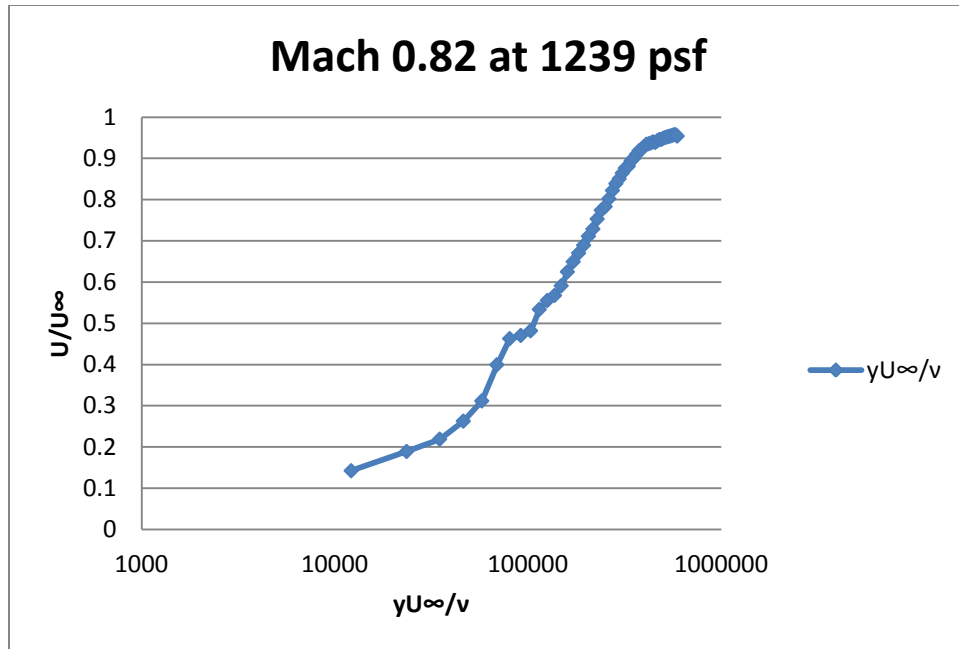


Figure B.9: Clauser plot for 0.824 inch ID shroud tubes at $M = 0.82$, $P = 1239$ psf.

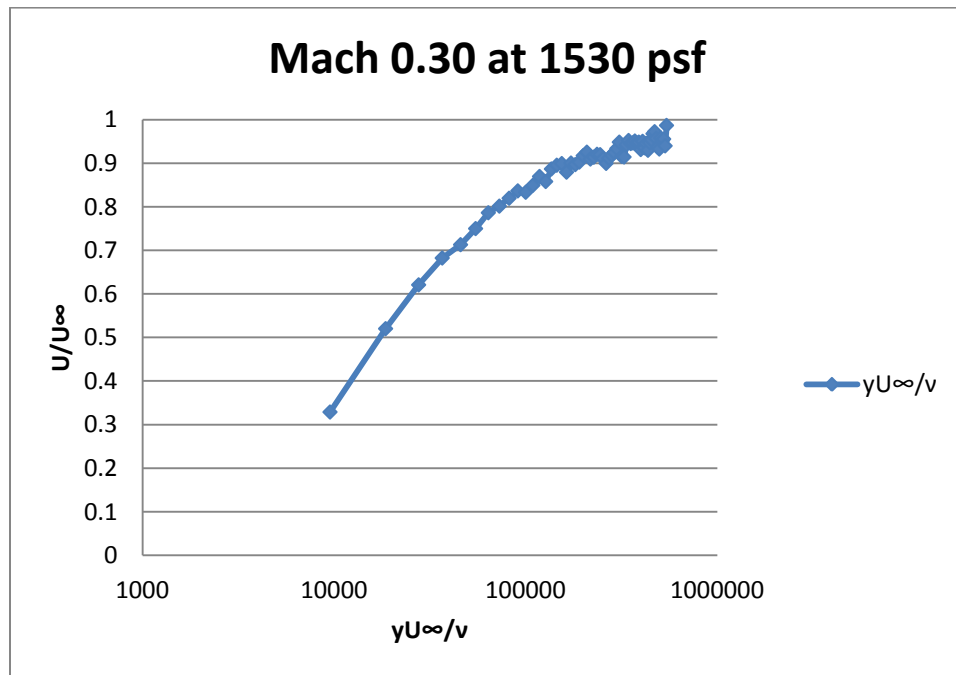


Figure B.10: Clauser plot for 0.364 inch ID shroud tubes at $M = 0.3$, $P = 1530$ psf.

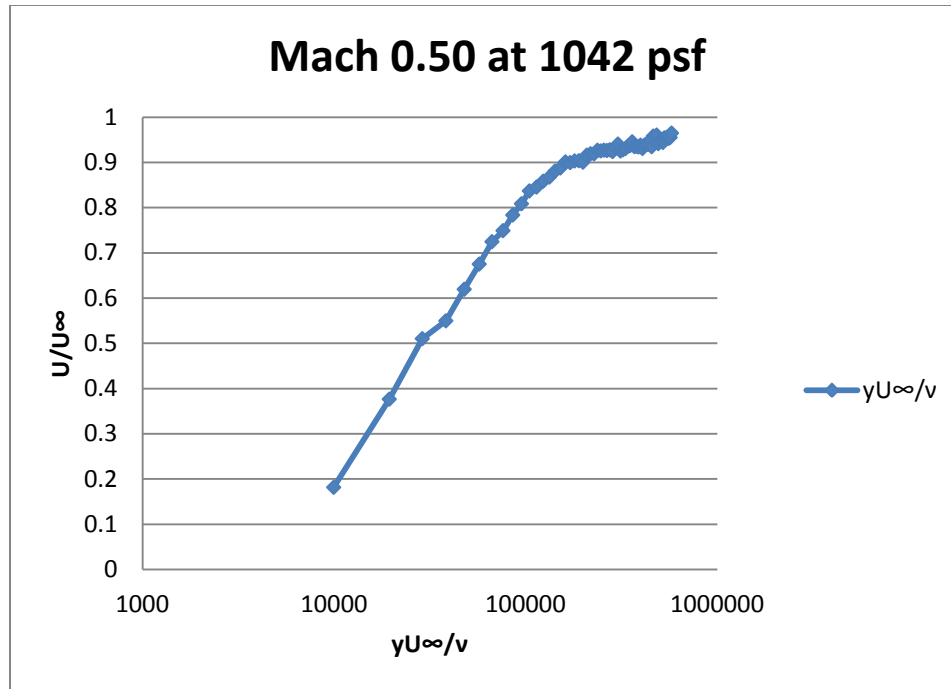


Figure B.11: Clauser plot for 0.364 inch ID shroud tubes at $M = 0.5$, $P = 1042$ psf.

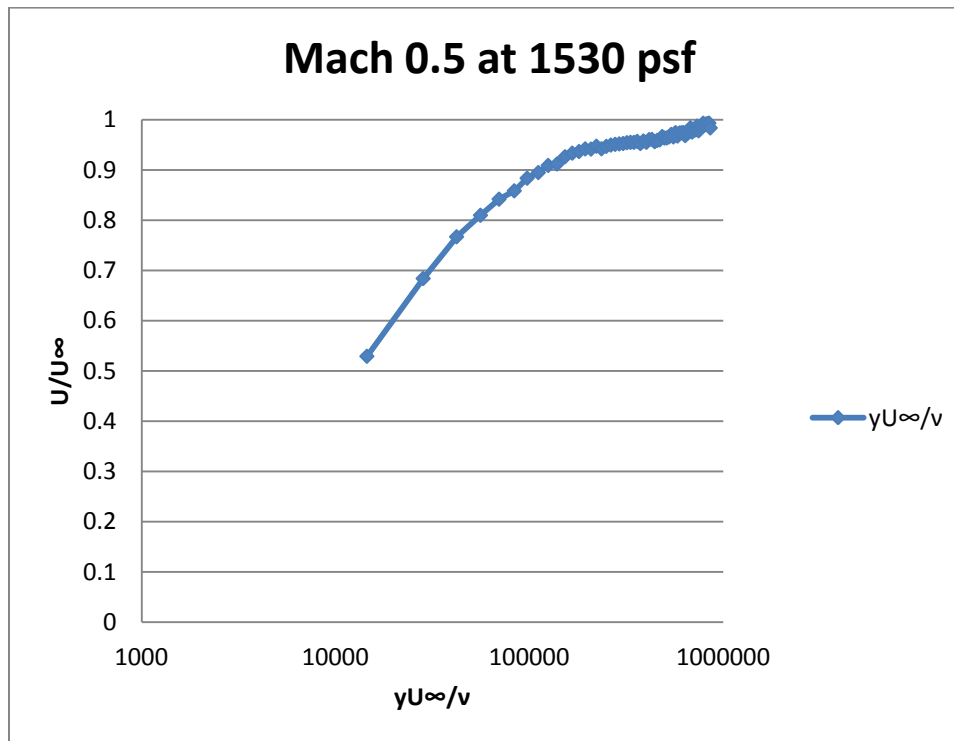


Figure B.12: Clauser plot for 0.364 inch ID shroud tubes at $M = 0.5$, $P = 1530$ psf.

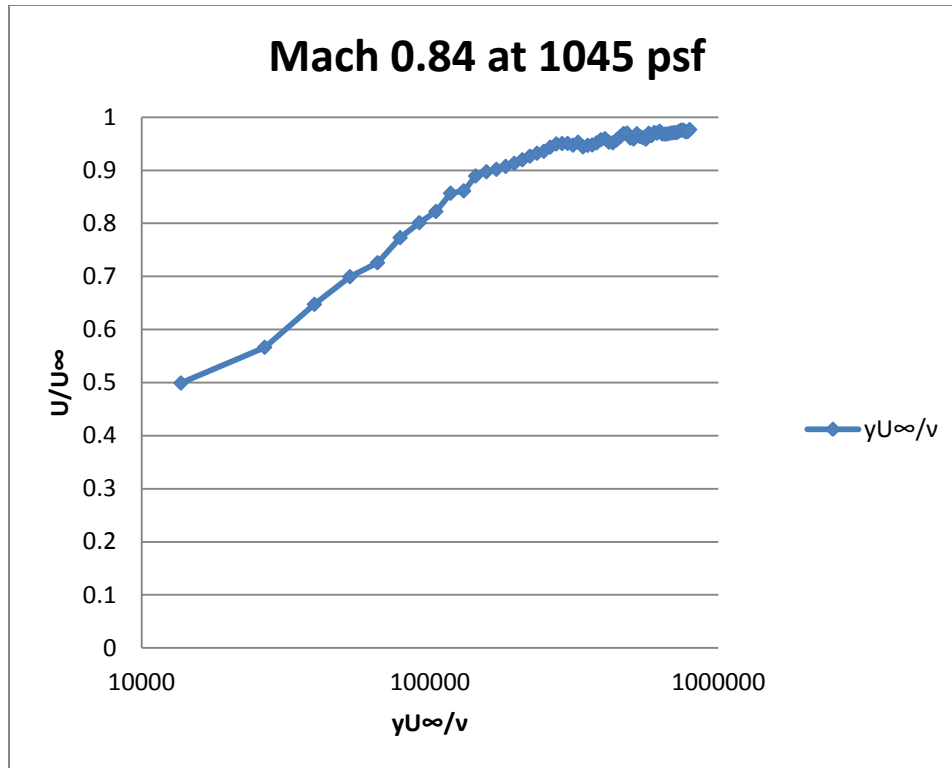


Figure B.13: Clauser plot for 0.364 inch ID shroud tubes at $M = 0.84$, $P = 1045$ psf.

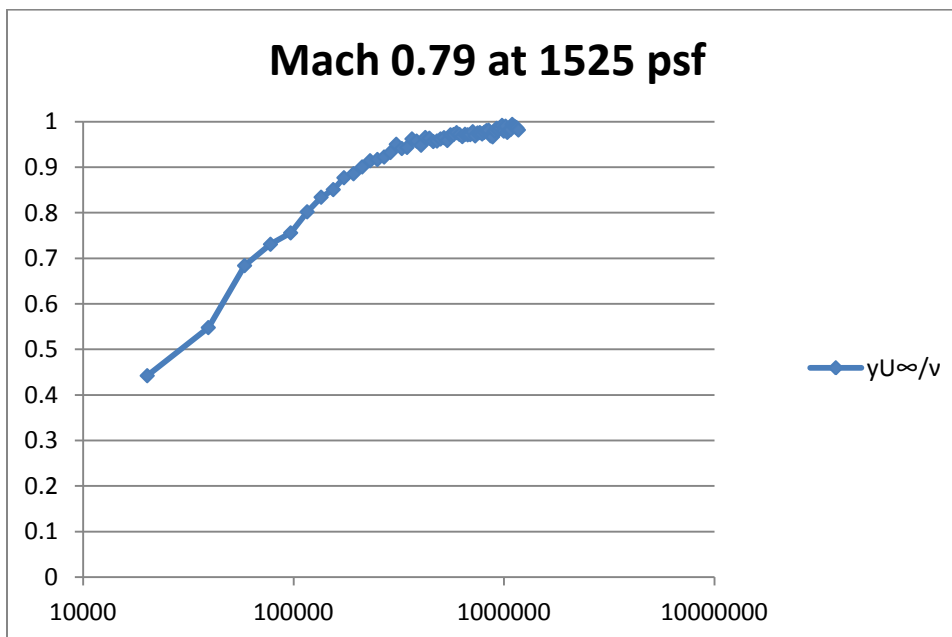


Figure B.14: Clauser plot for 0.364 inch ID shroud tubes at $M = 0.79$, $P = 1525$ psf.

Appendix C. Boundary Layer Profiles Compared to 1/7th Power Law

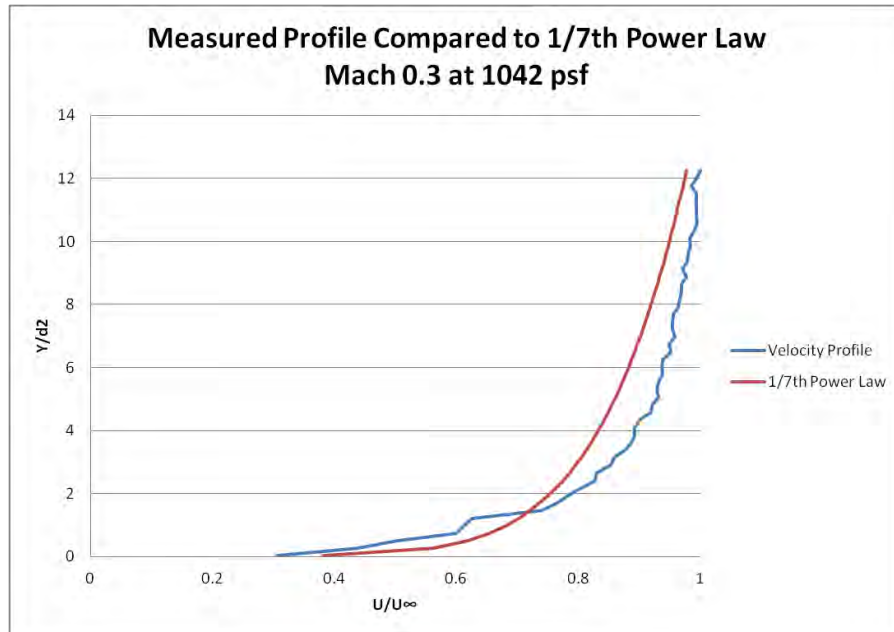


Figure C.1: Velocity profile compared to 1/7th Power Law at $M = 0.3$, $P = 1042$ psf.

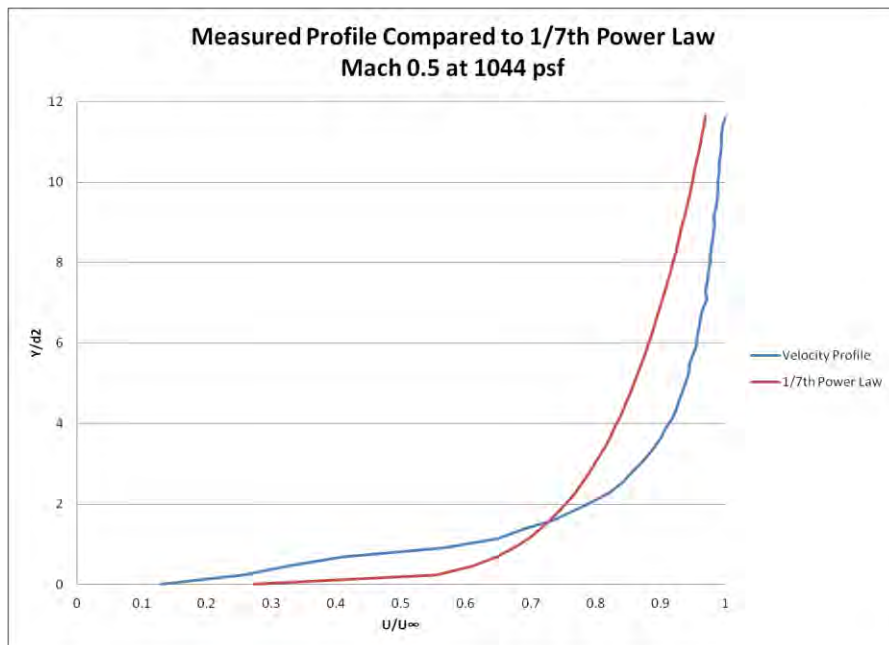


Figure C.2: Velocity profile compared to 1/7th Power Law at $M = 0.5$, $P = 1044$ psf.

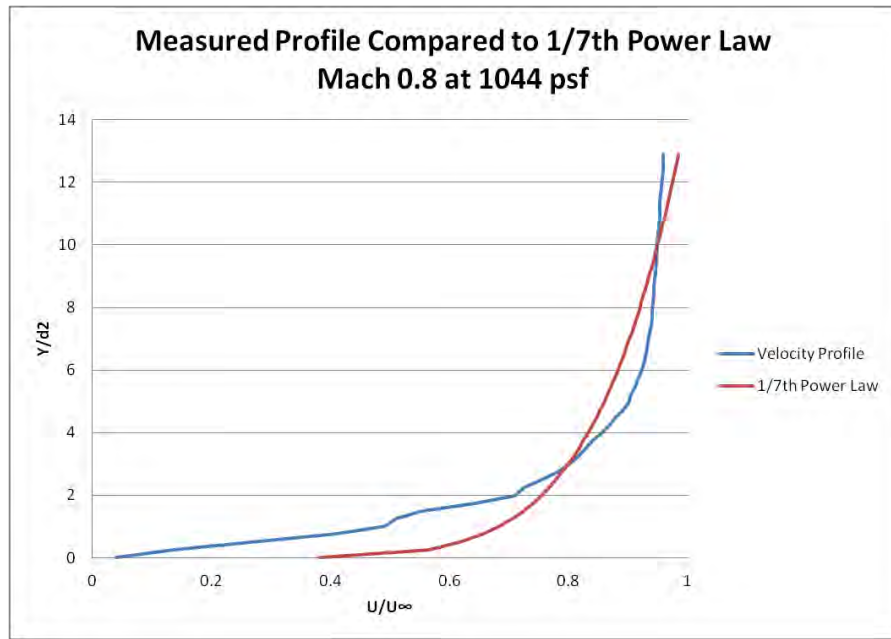


Figure C.3: Velocity profile compared to 1/7th Power Law at $M = 0.8$, $P = 1044$ psf.

Bibliography

1. Jakab, Peter L., *Visions of a Flying Machine: The Wright Brothers and the Process of Invention*, Smithsonian Institution Press, Washington D.C., 1990.
2. Tropea, C., Yarin, A., and Foss, J., *Springer Handbook of Experimental Fluid Mechanics*, Springer, Verlag, Berlin, Heidelberg, 2007.
3. Adrian, Ronald J., and Westerweel, Jerry, *Particle Image Velocimetry*, Cambridge University Press, New York, NY, 2011.
4. Reeder, M. F., Crafton, J. W., Estevadeordal, J., Delapp, J., McNiel, C., Peltier, D., and Reynolds, T., "Clean seeding for flow visualization and velocimetry measurements," *Experimental Fluids*, 2010, Vol. 48, pp. 889-900.
5. Wehrmeyer, J., Menako, C., Sirbaugh, J., and Sinclair, D., "Planar Doppler velocimetry applied in the AEDC 16T large-scale transonic wind tunnel," 48th AIAA Aerospace Sciences Meeting, Orlando, FL, 4-7 January 2010.
6. Love, B., Reeder, M., Schmit, R., Presdorf, T., "Applying Clean Seeding for Velocimetry in the AFRL Trisonic Gasdynamics Facility," AIAA Paper 2010-1033.
7. Love, B. T., *Particle Size Control for PIV Seeding Using Dry Ice*, MS thesis, AFIT/GAE/ENY/10-M15, Department of Aeronautics and Astronautics, Air Force Institute of Technology (AU), Wright-Patterson AFB OH, March 2010.
8. Raffel, M., Willert, C., Wereley, S., and Kompenhans, J., *Particle Image Velocimetry, A Practical Guide*, Springer, New York, NY, 2nd ed., 2007.
9. Melling, A., "Tracer particles and seeding for particle image velocimetry," *Measurements Science and Technology*, Vol. 8, No. 12, 1997, pp. 1406-1416.
10. LaVision, Göttingen, Germany, *FlowMaster Product-Manual*, 2007
11. Greene, B. G., *Characterization and Control of Carbon Dioxide Seed Particles in Particle Image Velocimetry*, MS thesis, AFIT/GAE/ENY/08-M12, Department of Aeronautics and Astronautics, Air Force Institute of Technology (AU), Wright-Patterson AFB OH, June 2008.
12. DeLapp, C.J., Reeder, M. F., Crafton, J., and Goss, L. P., "Clean Seeding Material for Particle Image Velocimetry Measurements," 25th AIAA Aerodynamic Measurement Technology and Ground Testing Conference, San Francisco, CA, 5-8 June 2006.

13. McNiel, C. M., Peltier, D. W., Reeder, M. F., and Crafton, J., "Clean Seeding for Particle Image Velocimetry," 22nd International Congress on Instrumentation in Aerospace Simulation Facilities, Pacific Grove, CA, 10-14 June 2007.
14. Anderson, John, D., *Fundamentals of Aerodynamics*, McGraw-Hill, New York, NY, Fifth Edition, 2011.
15. Schlichting, H., *Boundary Layer Theory*, McGraw-Hill, New York, NY, 1979.
16. Klebanoff, P. S., *Characteristics of Turbulence in a Boundary Layer with Zero Pressure Gradient*, NACA Report 1247, 1955.
17. Air Force Research Laboratory, *TGF User Manual*.
18. McMaster-Carr Supply Company, Online Catalog, <http://www.mcmaster.com>
19. Humble, R. A., Scarano, F., van Oudheussden, B. W., "Particle image velocimetry measurements of a shock wave/turbulent boundary layer interaction," *Experimental Fluids*, 2007, Vol. 43, pp. 173-183.

REPORT DOCUMENTATION PAGE				Form Approved OMB No. 074-0188	
<p>The public reporting burden for this collection of information is estimated to average 1 hour per response, including the time for reviewing instructions, searching existing data sources, gathering and maintaining the data needed, and completing and reviewing the collection of information. Send comments regarding this burden estimate or any other aspect of the collection of information, including suggestions for reducing this burden to Department of Defense, Washington Headquarters Services, Directorate for Information Operations and Reports (0704-0188), 1215 Jefferson Davis Highway, Suite 1204, Arlington, VA 22202-4302. Respondents should be aware that notwithstanding any other provision of law, no person shall be subject to an penalty for failing to comply with a collection of information if it does not display a currently valid OMB control number.</p> <p>PLEASE DO NOT RETURN YOUR FORM TO THE ABOVE ADDRESS.</p>					
1. REPORT DATE (DD-MM-YYYY) 22 -03-2012		2. REPORT TYPE Master's Thesis		3. DATES COVERED (From - To) August 2010 - March 2012	
TITLE AND SUBTITLE Boundary Layer Measurements in the Trisonic Gas-dynamics Facility Using Particle Image Velocimetry with CO ₂ Seeding				5a. CONTRACT NUMBER	
				5b. GRANT NUMBER	
				5c. PROGRAM ELEMENT NUMBER	
6. AUTHOR(S) Wolfe, Daniel B., Major, USAF				5d. PROJECT NUMBER	
				5e. TASK NUMBER	
				5f. WORK UNIT NUMBER	
7. PERFORMING ORGANIZATION NAMES(S) AND ADDRESS(S) Air Force Institute of Technology Graduate School of Engineering and Management (AFIT/ENY) 2950 Hobson Way, Building 640 WPAFB OH 45433-8865				8. PERFORMING ORGANIZATION REPORT NUMBER AFIT/GAE/ENY/12-M43	
9. SPONSORING/MONITORING AGENCY NAME(S) AND ADDRESS(ES) Mr. Tom Presdorf Tom.presdorf@wpafb.af.mil Air Force Research Laboratory, Air Vehicles Directorate Bldg 45 2130 Eighth St WPAFB, OH 45433-7542 937-255-6317				10. SPONSOR/MONITOR'S ACRONYM(S) AFRL/RBAI	
				11. SPONSOR/MONITOR'S REPORT NUMBER(S)	
12. DISTRIBUTION/AVAILABILITY STATEMENT APPROVED FOR PUBLIC RELEASE; DISTRIBUTION UNLIMITED.					
13. SUPPLEMENTARY NOTES This material is declared a work of the U.S. Government and is not subject to copyright protection in the United States.					
14. ABSTRACT Particle image velocimetry (PIV) is utilized with solid carbon dioxide (CO ₂) seeding material to conduct boundary layer measurements in the test section of the Air Force Research Laboratory's Trisonic Gas-dynamics Facility (TGF), which has a 24 inch by 24 inch cross-section. Freestream velocity was set at Mach 0.3, Mach 0.5, or Mach 0.8 while stagnation pressure ranged from 500 to 2400 pounds per square foot (psf). High pressure liquid CO ₂ was directed through expansion nozzles into shroud tubes which led to solidified particles in the wind tunnel stagnation chamber. Two different sets of shroud tubes were used to modify the size of dry ice particles produced and the particle number density. Shroud tubes with an inside diameter (ID) of 0.824 inches provided good particle count and coverage for stagnation pressures between 500 and 1500 psf, while 0.364 inch ID shroud tubes demonstrated good particle count and coverage for stagnation pressures over 1000 psf. Overall, the PIV results produced freestream velocity measurements and boundary layer profiles which compared well with expected values. After initial processing, turbulence data closely followed trends expected within boundary layer, but levels were somewhat higher than anticipated. When the PIV data was processed using elliptical interrogation regions, elongated in the streamwise direction, resulting turbulence levels were much closer to expectations.					
15. SUBJECT TERMS Particle Image Velocimetry, Carbon Dioxide, Clean Seeding, Boundary Layer, Trisonic Gas-dynamics Facility, Wind Tunnel					
16. SECURITY CLASSIFICATION OF: UNCLASSIFIED			17. LIMITATION OF ABSTRACT UU	18. NUMBER OF PAGES 109	19a. NAME OF RESPONSIBLE PERSON Dr. Mark Reeder
a. REPO RT U	b. ABSTRA CT U	c. THIS PAGE U			19b. TELEPHONE NUMBER (Include area code) (937) 255-3636, ext 4530 (mark.reeder@afit.edu)

Standard Form 298 (Rev. 8-98)
Prescribed by ANSI Std. Z39-18

